Identification de photons UHE dans le cadre de l'astronomie multi-messagers avec l'universalité à l'Observatoire Pierre Auger

Zoé Torrès

THÈSE

Pour obtenir le grade de

DOCTEUR DE L'UNIVERSITÉ GRENOBLE ALPES

École doctorale : PHYS - Physique
Spécialité : Physique Subatomique et Astroparticules
Unité de recherche : Laboratoire de Physique Subatomique et Cosmologie

Identification de photons UHE dans le cadre de l'astronomie multi-messagers avec l'universalité à l'Observatoire Pierre Auger

Identification of UHE photons for multi-messengers astronomy with universality at the Pierre Auger Observatory

Présentée par :

Zoé TORRÈS

Direction de thèse :

Corinne BERAT DIRECTRICE DE RECHERCHE, CNRS DELEGATION ALPES	Directrice de thèse
Carla BLEVE CNRS	Co-encadrante de thèse

Rapporteurs :

OLIVIER DELIGNY
DIRECTEUR DE RECHERCHE, CNRS DELEGATION ILE-DE-FRANCE SUD
YVONNE BECHERINI
PROFESSEURE DES UNIVERSITES, UNIVERSITE PARIS CITE

Thèse soutenue publiquement le **27 octobre 2023**, devant le jury composé de :

LAURENT DEROME, PROFESSEUR DES UNIVERSITES, UNIVERSITE GRENOBLE ALPES	Président
OLIVIER DELIGNY, DIRECTEUR DE RECHERCHE, CNRS DELEGATION ILE-DE-FRANCE SUD	Rapporteur
YVONNE BECHERINI, PROFESSEURE DES UNIVERSITES, UNIVERSITE PARIS CITE	Rapporteure
ANNE STUTZ, CHARGEE DE RECHERCHE, CNRS DELEGATION ALPES	Examinatrice
DAMIEN DORNIC, CHARGE DE RECHERCHE HDR, CNRS DELEGATION PROVENCE ET CORSE	Examinateur

Titre: Identification des photons UHE pour l'astronomie multi-messagers avec l'universalité à l'Observatoire Pierre Auger

Mots clés: Photon, Universalité, Ultra haute energie, Astronomie multi-messagers, Observatoire Pierre Auger

Résumé: Les neutrinos, les rayons cosmiques chargés, et les photons de très haute énergie ainsi que les ondes gravitationnelles fournissent des informations complémentaires pour étudier les objets les plus énergétiques de l'Univers, permettant ainsi le developpement de l'astronomie multi-messagers. L'Observatoire Pierre Auger est l'expérience phare qui étudie les rayons cosmiques à ultra-haute énergie et recherche les neutrinos et photons les plus énergétiques. L'objectif du travail de thèse présenté dans ce manuscrit est de développer une recherche performante de photons d'ultra-haute énergie dans les données Auger, en concevant une analyse discriminante de qualité basée sur une méthode de reconstruction des gerbes atmosphériques en exploitant le principe d'universalité. Les observables utlisées pour la reconstruction proviennent uniquement des détecteurs de surface de l'Observatoire (SD). Ce principe d'universalité implique que les propriétés moyennes d'une gerbe atmosphérique peuvent être décrites avec un nombre réduit de paramètres macroscopiques décrivant ces gerbes. Un modèle prédisant les sigaux dans les détecteurs du SD, et basé sur ce principe, a été développé dans la collaboration. Ainsi, en utilisant ce modèle, le maximum de développement des gerbes, une observable qui n'est pas directement accessible avec le SD, est reconstruit grace à la methode développée dans ces travaux de thèse. Cette observable permet de séparer les gerbes initiées par des photons de celles issues de hadrons. Le maximum de développement de la gerbe ainsi reconstruit, il est combiné à deux autres variables caractérisant la gerbe pour être introduit dans une analyse discrimante. Dans un premier temps, les différentes étapes de l'analyse sont développées et optimisées sur des simulations de gerbes initiées par des photons et des protons. Finalement, ses performances sont étudiées sur un échantillon de gerbes détectées à l'Observatoire Pierre Auger et les résultats sont comparés à la recherche de photons UHE actuelle faite au sein de l'Observatoire.

Title: Identification of UHE photons for multi-messengers astronomy with universality at the Pierre Auger Observatory

Keywords: Photon, Universality, Ultra high energy, Multi-messengers astronomy, Pierre Auger Observatory

Abstract: Neutrinos, cosmic rays, photons of ultra high energy as well as gravitational waves provide complementary information to study the most energetic objects in the universe, allowing therefore the development of multi-messengers astronomy. The Pierre Auger Observatory is the current experiment studying cosmic rays at the highest energies and searching for the most energetic neutrinos and photons. The aim of the thesis work presented in this manuscript is to develop an efficient search of ultra high energy photons in the Auger data, by building a discriminating analysis based on a reconstruction method using the universality of extensive air showers. The observables used are obtained only from the surface detectors (SD) of the Observatory. The universality principle states that the average properties of air showers can be described by a small set of macroscopic parameters describing the air showers. A model predicting the signals in the detectors of the SD was developed by the collaboration. Thus, using this model, the maximum depth of the shower development, an observable not directly accessible with the SD, is reconstructed using the method developed in this thesis work. This observable allows to discriminate between photon-induced air showers and showers initiated by hadrons. The shower maximum beging reconstructed, it is combined with two other variables describing the air showers, and they are implemented in a discriminating analysis. To begin with, the different steps of the analysis are developed and optimised on simulations of photon-induced and proton-induced showers. Then, its efficiency is studied on a sample of data detected by the Observatory and the results are compared to the current SD search for UHE photons.

Table of contents

Chapter 1

Introduction

High energy astroparticles are valuable messengers from the universe. The cosmos has been observed through photons since the beginning of modern astronomy, at first in the optical range, which was then enlarged to infrared and ultra-violet. The detection of ultra high energy (UHE) photons plays a crucial role in the understanding of extreme astrophysical phenomena. Nowadays, the most energetic photons ever detected reached energies in the PeV range and the search for photon emissions at higher energies, in which their absorption is less likely, is an ongoing quest.

The search for UHE neutral particles (in the EeV range) is of great importance in the era of multi-messenger astronomy: as they are not deflected by galactic and extra-galactic magnetic fields on their way to Earth, they can provide valuable information on the nature of ultra high energy cosmic rays (UHECR) sources. Indeed, although the knowledge on UHECRs has developed greatly in the last decades, thanks to the contribution of UHECR observatories such as the one operated by the Pierre Auger Collaboration, the question of where and how cosmic rays are accelerated to such energies remains one of the main questions. The UHE neutral particles are thought to be produced alongside UHECRs in the source environment, or during their propagation. They could also open a window to new physics beyond the Standard Model as several scenarios predict the production of these neutral astroparticles in the decay of still unknown heavy particles.

In this context, UHECR observatories and in particular the Pierre Auger Observatory in Argentina, are searching for these neutral messengers among their data largely dominated by charged cosmic rays. They study the extensive air showers generated by the interactions of UHECRs in the atmosphere. The Pierre Auger Observatory is today's largest UHECR observatory. It uses an hybrid mode of detection consisting in a network of surface detectors and several fluorescence telescopes to reconstruct the initial properties of the cosmic ray. UHE photons can be identified as the extensive air showers they produce have different characteristics from those of showers induced by charged UHECRs, which allows the design of analyses aiming to discriminate photons from hadrons. In the search of UHE photons produced by astrophysical sources or by envisaged new physics processes, diffuse fluxes of high energy photons could constitute a "background" hiding localised photon emission. They have to be accounted for as well as the attenuation length of photon resulting from their interaction with different photon fields permeating

the universe which limits the detection horizon. In the absence of detections above the PeV range, upper limits have been set on UHE photon fluxes by cosmic ray observatories and have disfavoured several models of UHECR production in non acceleration processes.

The work presented in this thesis manuscript falls within the context of the search for UHE photons and is mainly dedicated to their identification using data provided by the surface detector of the Pierre Auger Observatory. The analysis relies on the concept of the universality of extensive air showers occurring at UHE. The very important amount of secondary particles in UHE showers results in a smoothing of the shower properties which can then be described by a few macroscopic shower parameters. By designing a reconstruction for photon-induced showers based on this principle, we estimate the depth corresponding to the maximum of the shower development, a robust observable to discriminate photons from hadrons primaries. This observable is accessible directly using hybrid data but this data set suffers of low statistics making it impossible to probe efficiently the highest energies. The reconstructed depth of the shower maximum is then combined in a multivariate analysis with two other elaborated discriminant variables with the objective of improving the performance of the photon search with the surface detector.

This manuscript is divided in six chapters. The first one is dedicated to multi-messenger astronomy at UHE, above 10^{17} eV, with an emphasis on cosmic rays. The importance of the searches for neutrals messengers to identify the sources of UHECR is underlined, and the state-of-art in the UHE neutral searches is presented. The second chapter presents the estimation of the diffuse UHE photon and neutrino fluxes originating from the interactions of UHECRs with the interstellar gas in Milky Way. The third chapter is devoted to the search for UHE photons taking place at the Pierre Auger Observatory. The physics of air showers is detailed as well as the detection method used at the Observatory, especially with the surface detector. The specificities of photon-induced showers with respect to hadron-induced ones exploited in the UHE photons search are described and the different analyses performed by the Pierre Auger Collaboration are presented. In the fourth chapter, the concept of the universality of extensive air showers used in this work to design a novel reconstruction of photon-induced showers is introduced, alongside the models predicting the signals in the surface detectors of the Observatory. The fifth chapter explains the elaborated procedure to implement the universality-based reconstruction which provides appropriate variables to identify photon-induced showers recorded by the surface detector. Finally, the designed reconstruction is applied on photon and proton simulations and thanks to the information extracted from this reconstruction, three photon-hadron separation observables are combined in a multivariate analysis, as described in the last chapter. The obtained results after applying the designed analysis on a small Auger data sample are presented and commented.

Chapter 2

Multi-messenger astronomy at ultra-high energies

Contents

Nowadays, the astrophysical sources and the physics mechanisms producing ultra high energy cosmic rays (UHECR) are still unclear. In this context, the search for photons and neutrinos in the flux of cosmic rays at the highest energies is of great interest. These neutral messengers, which are not deflected by galactic and extra-galactic magnetic fields, could be produced alongside UHECRs or during their propagation. This chapter introduces cosmic rays, focusing on those above 10 TeV, and the importance of high-energy neutral astroparticles in UHECR physics. Then, the mechanisms that could be at the origin of the production of UHE photons and neutrinos are presented.

2.1 Multi-messenger astronomy and UHECRs

Cosmic rays have been discovered at the beginning of the 20th century. After a brief recall of the discoveries related to cosmic rays, the features of the energy spectrum of cosmic rays above 10 TeV originating from the intertwining multiple astrophysical phenomena is presented. Then, the searches for UHE neutral particles in the objective of identifying sources is addressed.

2.1.1 Brief history of cosmic rays

Cosmic rays are high energy particles travelling through space at the speed of light and reaching Earth from all directions. Their discovery dates back to 1912, when the Austrian physicist Hess went onboard balloons with a series of electroscopes at altitudes above 5000 m [1]. There, he observed that the rate of formation of ions in air was three times the one measured at sea level. From these observations, he concluded that Earth was bombarded by radiations coming from outer space, and gave them the name "cosmic radiations".

The discovery of cosmic rays, for which Hess got the Nobel prize in 1936, is related to the studies on radioactivity that started at the beginning of the 20th century. Before Becquerel discovered natural radioactivity in 1896, the discharged of electroscopes overtime had been observed for several years but the reason behind this phenomenon was unknown. The ionisation of air at the origin on the discharge possibly produced by radioactivity was studied by the scientific community at the time with measurements carried at different places on Earth (high altitudes, below ground, underwater...). Only after, the study of Hess coupled with the work of Pacini [2], who carried an experiment similar to Hess but deep under the see level, highlighted that radiations from outer space were striking Earth and were participating in producing the air ionisation.

Cosmic radiations were renamed "cosmic rays" at the beginning of the 1920s by Millikan as he thought these radiations were only composed of gamma rays [3]. However, in 1932 Clay and his collaborators demonstrated in [4] that the CR intensity varied with geographic latitude which is explained by the magnetic deflection of charged particles. It will be shown later that the composition of cosmic rays is dominated by positively charged particles and in particular protons.

Extensive air showers created by cosmic rays after their interaction in the atmosphere were discovered by Pierre Auger in 1938 [5] when studying the rate of coincidences between Geiger-Müller counters at the top of the atmosphere (Sec. 4.1). His work showed the presence of primary cosmic rays with an energy of about 10^{15} eV. Less than 20 years later, Heitler developed a model describing these extensive air showers [6] which is detailed in Sec. 4.1. The first air shower experiments based on ground arrays started in the mid-1940s. In 1963, a cosmic ray with a primary energy of 10^{20} eV was detected by the largest array built at the time, with 20 ground scintillator counters, by the Massachusetts Institute of Technology in New Mexico [7]. This motivated the need for larger arrays to study UHECRs.

In 1966, following the discovery of the cosmic microwave background (CMB) by Penzias and Wilson [8], three physicists, namely Greisen, Kuzmin and Zatsepin, theorised that cosmic rays at ultra high energies would interact with the CMB photons [9] [10]. These interactions during the propagation of cosmic rays results in an energy loss and create a distance horizon for the detection of ultra high energy cosmic rays (UHECRs) from distant sources. This phenomena, known as the GZK cut-off, is explained in Sec. 2.2.3.

In 1967, the Haverah Park detector, a 12 km^2 array composed of 200 water Cherenkov detectors was deployed in North Yorkshire and recorded air showers for 20 years [11]. The energy spectrum reported by the High Resolution Fly's Eye (HiRes) collaboration detecting air showers with fluorescence telescopes in Utah, indicated a suppression in the energy spectrum of UHECRs as expected from the GZK effect [12]. However, the spectrum published by the Akeno Giant Air Shower Array (AGASA) showed no evidence of such suppression [13]. To improve the measurement at such energies, a higher statistics is needed and the idea of larger arrays of more than 1000 km^2 arose to increase the sample of detected air showers at UHE. Accordingly, the project that led to the design and construction of the Pierre Auger Observatory, the largest cosmic ray observatory, began in 1995 (see Sec. 4.2).

Since then, the knowledge acquired on UHECRs, on their nature, on their energy, or their arrival direction is much more important, in particular thanks to the contribution of the Pierre Auger Collaboration. Nevertheless, the physics mechanisms behind the creation of UHECRs are still unclear as explained later in this chapter. The identification of UHE neutral particles among the flux of charged UHECRs is one key to understand these physics mechanisms as well as the potential sources from which UHECRs originate.

2.1.2 The cosmic ray spectrum above 10 TeV

The spectrum of cosmic rays covers a large band of 11 decades in energy ranging from a couple of GeV up to energies higher than 10^{20} eV. The flux of cosmic rays decreases with increasing energy as roughly a power law of a spectral index -3, falling from ~ 1 per m^2 per second at 10^{11} eV to only 1 per km^2 and per year above 10^{18} eV. Depending on the energy range considered, the detection method differs. From the lower end of the spectrum up to $\sim 10^{14}$ eV, cosmic rays can be detected directly on top of the atmosphere with detectors whose size allows them to be carried by balloons or satellites, for instance by AMS (Alpha Magnetic Spectrometer) [14] on the International Space Station. The flux being too weak at above $\sim 10^{17}$ eV, the detection of cosmic ray cannot be achieved with such devices as the effective size of the detector must compensate the fall flux.

When arriving to Earth, cosmic rays interact with the nuclei in the molecules present in the atmosphere and generate a cascade of particles called air showers (see Sec. 4.1), like those produced in calorimeters. The more energetic the cosmic ray is, the more penetrating the shower becomes. At sufficiently high energies, the shower is deep enough for a large part of the produced secondary particles to reach ground at a given altitude above

sea level. Therefore, the detection of cosmic rays is performed indirectly at ground by measuring the signals created by these secondary particles. Fig. 2.1 shows the cosmic ray spectrum for energies above 10 TeV measured by ground experiments. The flux on the vertical axis is multiplied by $E^{2.6}$ to highlight the features of the spectrum and especially the change of spectral index in the power law. Four main features are visible: the knee around 3×10^{15} eV, the second knee around 10^{17} eV, the ankle at 5×10^{18} eV and the flux suppression above $\sim 5 \times 10^{19}$ eV. These features are of great interests for the understanding of cosmic ray production at the source as well as their propagation mechanisms. Their interpretation in terms of astrophysical phenomena is detailed below:

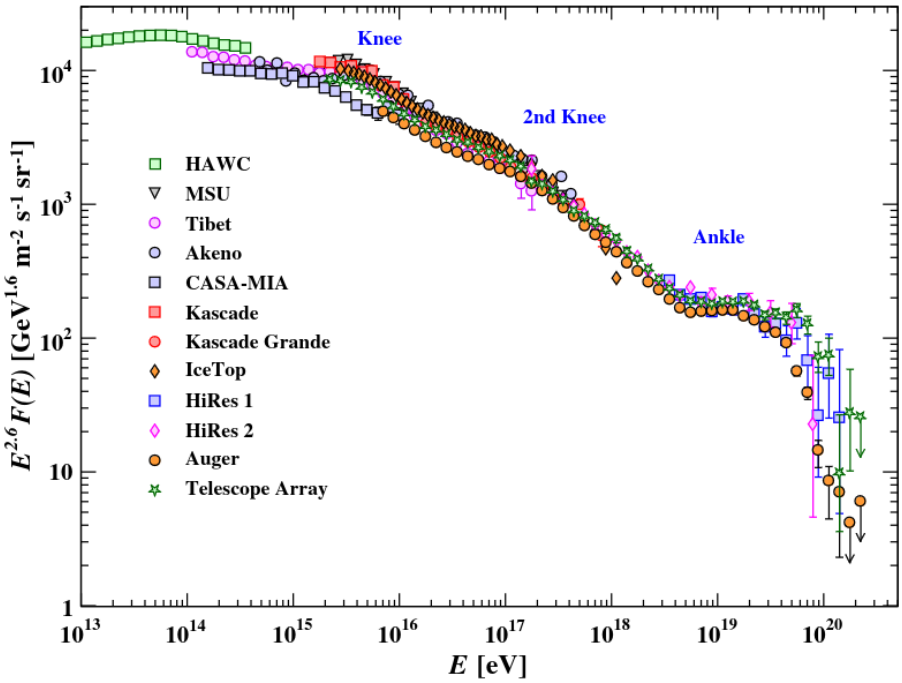

Figure 2.1: The all particle of cosmic rays above 10^{13} eV measured by ground experiments (see legend). Taken from [15] (see references therein).

- **Knee**: The steepness of the spectrum increases as spectral index γ changes from ~ -2.7 to ~ -3.1 at the knee region and was first reported in [16]. The most common scenario to explain this inflection in the spectrum is that this energy corresponds to the maximal energy reachable by proton accelerated in galactic sources. Light elements contribute to the majority of the CR flux up to this region, and the composition gradually evolves towards heavier elements [17].
- **Second knee**: The transition to heavier elements ranges for two decades in energy above the knee. Therefore, the second inflection observed at the second knee is thought to originate from similar mechanisms as for the knee region but for the heavier nuclei (i.e. iron) [18].
- **Ankle**: The steepness of the spectrum changes again as the spectral index increases from -3.3 to -2.5. This behaviour is interpreted as the possible transition from galactic to extra-galactic sources of cosmic rays.

- **Suppression**: The suppression at the end of the cosmic ray spectrum is predicted by the interaction of UHECR with the low energy CMB photon during their propagation [9] [10]. The so-called GZK effect is explained in Sec. 2.2.3. It could be also linked to sources of UHECRs reaching their maximal accelerating power.

In addition to these spectral features, the Pierre Auger Collaboration recently reported a steepening point referred to as the "instep" around 10^{19} eV [19]. To interpret the changes observed in the UHECR spectrum, information like the composition of the flux and the arrival directions are needed, and experimental measurements must be confronted to the models describing the production and propagation of UHECRs.

2.1.3 Multi-messenger astronomy to identify UHECR sources

The understanding of the spectrum of UHECRs measured on Earth is conditioned by our knowledge on the astrophysical accelerators that could be producing particles of such energies. The detection of the photons and neutrinos pointing in their direction would allow the identification of UHECR sources and to derive constrains on the models of sources. In the next section, the different searches for sources of photons and neutrinos at UHE, above $\sim 10^{17}$ eV, are presented.

The search for UHE photons is limited by the distance to the sources. Along their propagation, they can be absorbed when interacting by pair production with low energy photon fields permeating the universe. In consequence, the search horizon is restricted to a few kpc at 10^{15} eV to a few Mpc at 10^{19} eV (see Fig. 2.5). On the contrary, neutrinos can travel very large distances without interacting.

In this context, observatories of UHECRs are great tools to search for these neutral messengers. The Pierre Auger Observatory (presented in Sec. 4.2) is sensitive to UHE photons and neutrinos, while the Telescope Array is only sensitive to UHE photons. The two collaborations are searching for UHE neutrals among their data mostly composed of charged cosmic rays. Besides UHECR observatories, the IceCube Neutrino Observatory deployed at the South Pole, is designed to detect neutrinos from $\sim$ 100 GeV to above 10^{18} eV. Different types of searches can be performed and are presented below with a focus on UHE photons and results from the Pierre Auger Collaboration.

Searches for a diffuse flux

These searches consist in looking for a direction-independent flux of UHE photons and neutrinos. The photon search analyses above 10^{17} eV are presented in Sec. 4.4. In the absence of unambiguous UHE photon candidates, upper limits on the flux have been computed (see Fig. 4.21). The latest results for the search of a diffuse flux of UHE neutrinos [20] are mentioned in Sec. 3.6 (Fig. 3.12). No neutrino were identified and the upper limits set by the Pierre Auger, IceCube and ANITA collaborations[21] [22] [23] constrain several models of cosmogenic and astrophysical neutrino production.

Searches for sources

Blind searches look for an excess of events from a given direction. The search for a directional flux of photons published in [24] by the Auger Collaboration is performed for energies between 2×10^{17} and 3×10^{18} eV. The expected background is estimated for each direction and no significant excess has been found. Accordingly, the directional upper limits derived in [24] are reported in Fig. 2.2 on a celestial map. A similar search above 10^{18} eV has been reported in [25] by the Telescope Array collaboration: no excess has been identified in the field of view of the observatory and upper limits were derived as well. A search for point-like sources of UHE neutrinos has been performed in [26] by the Pierre Auger Collaboration and upper limits were derived as function of the source declination and compared to the ones obtained by the neutrino observatories IceCube [27] and ANTARES [28].

The photon search can be targeted to certain source candidates: the analysis principle is identical to the blind search but is restricted to specific astrophysical sources classes (pulsars, galactic centre, Centaurus A...). The targets are mainly galactic because of the attenuation length of photons which limits their detection from far away sources. Such study was performed for photon energies ranging from $10^{17.3}$ to $10^{18.5}$ eV in [29] by the Auger Collaboration: the results showed no evidence of the emission of photons by any candidates.

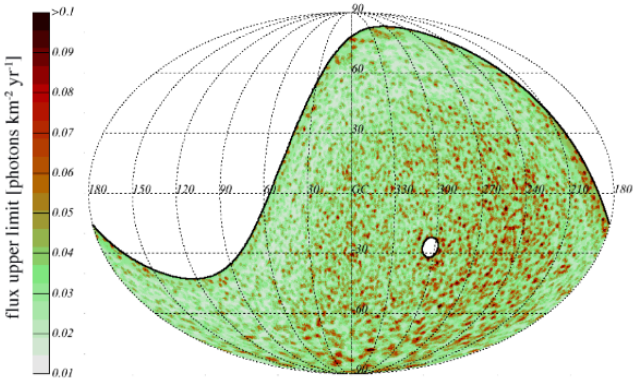

Figure 2.2: Upper limits on the UHE photon flux on a celestial map in galactic coordinates set with the hybrid data of the Pierre Auger Observatory. From [24].

Follow-up searches for UHE neutral particles from gravitational wave (GW) events and other transient sources

Since the breakthrough in multi-messenger astronomy generated by the first detection of gravitational waves in 2015 [30], searches for the indication of signals in coincidence with GW events have been developed. Sources producing gravitational waves observed by the GW detectors provide extreme astrophysical environments in which UHECRs could be produced, along with photons and neutrinos. Recently, the Pierre Auger Observatory

performed a follow-up search of UHE photons above 10^{19} eV with GW events detected by LIGO/Virgo [31]. This analysis searches for coincidences in time and space with the UHE photon candidates from the search for a diffuse flux published in [32]. The GW events are selected based on the quality of their localisation and distance, as the detection of UHE photons is limited to a certain distance horizon. UHE photons are looked for in specific time windows after and around the gravitational wave event: a short time window of 1000 s starting 500 s before the GW event and a long time window of 1 day starting 500 s after the event. Events are distributed in four classes depending on their distance and localisation: sources at large distance are interesting for hints of new physics as no photons are expected, while UHE photons are expected from closer sources. Ten of the selected events are within the Auger field of view. No coincidences were found and the first upper limits on the spectral fluence from the selected GW sources were derived and are shown in Fig 2.3 [31].

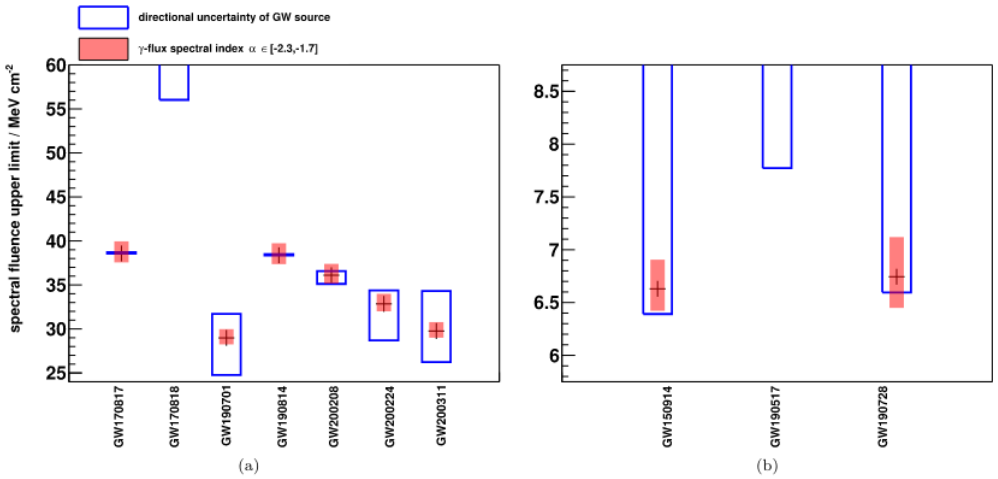

Figure 2.3: Upper limits on the spectral fluence of UHE photons from the 10 selected GW events. The left (right) panel corresponds to GW sources in the long (short) time window. The blue error bars arising from the directional uncertainty of the GW source. The red bars account for the impact of the variation of the power law spectral index of the energy spectrum of photons at the source. From [31].

Similar follow-up searches can be performed for UHE neutrinos. A GW signal generated by a binary neutron star merger (GW170817) was observed by LIGO/Virgo. Following the merger, a short gamma ray burst was detected by Fermi-GBM at the same location, as well as optical, ultra-violet and infrared emissions. The neutrino observatories IceCube and ANTARES, as well as the Pierre Auger Observatory, looked for coincident neutrino signals for energies between 100 GeV up to 10^{20} eV but no such signal was observed [33]. Moreover, the analysis published in [21] presents the search for UHE neutrinos from several binary black hole (BBH) mergers detected by LIGO/Virgo during the three runs carried by the GW detectors. In the absence of neutrino observations in coincidence with any BBH, the analysis set an upper limit on the total energy emitted in UHE neutrinos from all mergers. Also, following the detection of a $\sim$ 300 TeV neutrino at the IceCube

Observatory in significant coincidence with a gamma ray signal observed at Fermi-LAT in the direction of the TXS0506+056 blazar, a follow-up search for UHE neutrinos was performed at the Pierre Auger Observatory but no neutrino signal was found [34].

Neutrons

Besides UHE photons and neutrinos, neutrons can also be useful to point back at their sources locations. However, they cannot be distinguished from proton primaries and the search for a UHE neutron flux is done by looking for an excess of UHECR events in the source direction. Because they undergo β-decay, the distance they can travel is restricted to a few kpc (from $\sim$ 10 kpc at 10^{18} eV and increasing with energy), which corresponds to galactic-like distances. The targeted search for galactic accelerators published in 2014 in [35] reported no evidence for a neutron flux from any source candidates.

2.2 The production of UHE neutral particles

The emission of UHE photons and neutrinos could be directly related to the production of UHECRs and could originate either from acceleration processes, in Bottom-Up models, or by non acceleration processes in the Top-Down approach. The neutral particles can either be directly emitted or can result from the decay of the charged and neutral pions produced in these mechanisms. Besides the Top-Down and Bottom-Up approaches, UHE neutral particles can also be produced during the propagation of UHECRs when they interact with the photons of the Cosmic Microwave Background (CMB) according to the GZK effect. The different mechanisms mentioned here are presented in the following sections, alongside the potential sources of UHECRs.

2.2.1 Production of neutral particles in the source environment

In the Bottom-Up approach, the cosmic rays reach ultra high energies by being accelerated in magneto-hydrodynamic processes occurring in the source environment. In such environments, charged particles are accelerated through several interactions with the magnetised plasma. Today, two main kinds of acceleration processes are considered: the collision-less magnetic diffusion and the diffuse shock acceleration.

The first scenario was proposed by Enrico Fermi in 1949 [36] to explain the high energies reached by CRs. This model, later called Second Order Fermi Acceleration, is a stochastic model in which the incident charged particle interacts elastically with magnetised molecular clouds moving with a velocity V. Fermi demonstrated in [36] that the energy gained by the charged particle after each collision with a cloud can be expressed as in Eq.2.1. This model can lead to a power law spectrum for CRs. However, the limitation of this model relies in the important number of interactions required to reach the highest energies, resulting in a slow acceleration process, which is not compatible with the observations of the power law of the UHECR spectrum.

$$< \frac{\Delta E}{E} >= \frac{8}{3}\frac{V^2}{c^2} \tag{2.1}$$

In contrast to the model proposed by Fermi, the energy gain in the diffuse shock acceleration mechanism is faster, as expressed in Eq. 2.2. In this approach, which is called the Fisrt Order Fermi Acceleration [37], the particle is accelerated to high energies through interactions with a shock wave of magnetised matter. In this scenario the particle goes in and out of the shock wave several times and acquire each time a certain energy.

$$< \frac{\Delta E}{E} >= \frac{4}{3}\frac{V}{c} \tag{2.2}$$

Let's note E_0 the initial energy of the particle before encountering the shock wave, and β the factor describing the energy gain following each interaction. After n interactions the energy of the particle is $E = \beta^n E_0$. Moreover, let's consider N_0 initial particles and the probability p that a particle stays withing the shock wave after interacting. After n interaction, the remaining number of particles is $N = p^n N_0$. By matching n in both expression, we deduce:

$$\frac{\ln \frac{N}{N_0}}{\ln \frac{E}{E_0}} = \frac{\ln p}{\ln \beta} \tag{2.3}$$

and,

$$\frac{N}{N_0} = (\frac{E}{E_0})^{\frac{\ln p}{\ln \beta}} \Rightarrow \frac{\mathrm{d}N}{\mathrm{d}E} \propto E^{(\frac{\ln p}{\ln \beta}-1)} \tag{2.4}$$

The power law spectrum generated by this acceleration mechanism is expressed by Eq. 2.4. It was shown in [37] that the spectral index produced in this case is ~ -2, which is consistent with the UHECR spectrum presented in Sec. 2.1.2 when accounting for propagation effects. This model is the main acceleration process for UHECRs.

Although the nature of UHECRs sources is still undecided, with the acceleration scenarios described in this section, constraints on their nature can be derived. These constraints rely on the size R of the source, the average magnetic field intensity B and the charge of the cosmic ray $Z \times e$. To be accelerated to sufficient energies before escaping the acceleration site, the cosmic ray Larmor radius must remain smaller than the source size so that it stays confined. Therefore, the stronger the magnetic field B is, the less the source needs to be large. This is described by the Hillas criteria [38] (Eq. 2.5) which expresses the maximum energy E_{max} to which a source can accelerate the charged particle. This relation can also be illustrated by the Hillas plot seen in Fig. 2.4 [39]. The diagonal lines delimit the regions of size and magnetic field strength in which astrophysical sources can accelerate particles to 10^{20} eV. Only candidates above the lines are able to accelerate particles to this energy. It is important to note that the Hillas criteria is a necessary condition but not a sufficient condition. The energy losses are not accounted for and, in reality, they constrain more drastically the maximum reachable energy. Therefore each acceleration site candidate needs to be studied individually.

$$E_{max} \leqslant Z(\frac{R}{\text{kpc}})(\frac{B}{\mu G}) \times 10^{18} \text{ eV} \tag{2.5}$$

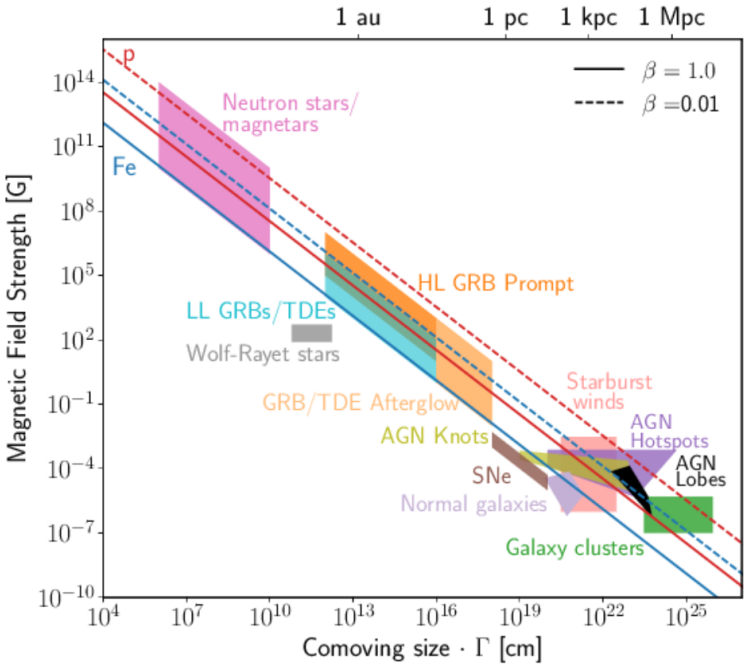

Figure 2.4: Hillas diagram showing candidates for acceleration sites of UHECRs as function of their magnetic field strength (vertical axis) and size (horizontal axis). The red (blue) lines delimit the region in which protons (iron nuclei) can be accelerate to 10^{20} eV. The plain (dashed) lines are reported for $V/c = 1$ ($V/c = 0.01$). Taken from [39].

Among the possible sources are Active Galactic Nuclei (AGNs) [40]. They define galaxies containing a massive accreting black hole in their centre which could be an accelerator site for UHECRs. About 15% of AGNs have relativistic jets and are classified as blazars if the jets point in our direction. UHECRs could be accelerated close to the black hole or within the jets. Another type of candidate sources are starbust galaxies [41] in which the level of star formation activity is high, especially in their centre. The star formation activity implies a high rate of supernova explosions and stellar winds. The shocks generated by these winds is considered as potential accelerators of UHECRs. A study of the arrival directions of UHECRs carried by the Pierre Auger Collaboration hints that they could be indeed sources of UHECRs [42]. Other important accelerators candidates are Gamma Ray Bursts (GRBs) [43] [44], intense and short pulses of gamma rays. Besides these three candidates, several other astrophysical objects can be considered as potential accelerators: pulsars [45], tidal disruption events (TDE) [46], galaxy clusters, binaries of black holes, black hole mergers, neutron stars.

UHE neutral astroparticles are expected to be produced in the sources environments by interaction of UHECR with the local matter. They are created by the decay of pions produced either by proton-proton collision or by photo-pion production. The latter is due

to UHECRs interacting with lower energy photons in the source environments and is probably the dominant process for UHE neutral particle production. The UHE photons and neutrinos produced in sources environments could help in identifying and understanding the UHECR sources. As these neutral particles are not deflected by magnetic fields, it is possible to point in the source direction. This last point is limited by the distance to these astrophysical sources. This is illustrated by Fig. 2.5 [47] in which the mean free path of photons for pair production is reported as function of their energy. Below 10^{14} eV, photons mostly interact with the infrared/optical background (IR/O). Above this threshold and up to 10^{19} eV, the background limiting the distance to the sources is the microwave background radiation (MBR or CMB). Finally, the radio background takes over.

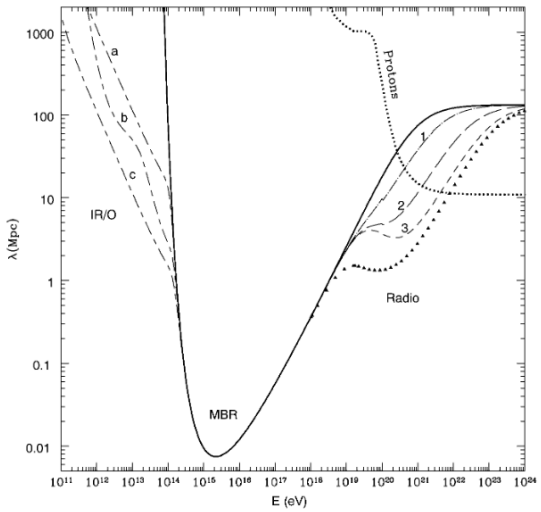

Figure 2.5: Pair production mean free path in Mpc for photons as function of their energy at redshift z=0 due to their interactions with several photon fields: the IR/O below 10^{14} eV, the CMB from 10^{14} to 10^{19} eV, and the radio background above. The lines a, b and c correspond to different models of IR/O backgrounds and the lines 1, 2 and 3 are for different radio backgrounds. The mean free path of UHE protons is also represented on the figure by the dotted line. Taken from: [47].

2.2.2 Production of neutral particles from non-acceleration processes

In the previous section, we presented the acceleration mechanisms that could produced UHECRs and consequently UHE photons and neutrinos in the vicinity of accelerator sites. Other models, in what is called the Top-Down approach, state that UHECRs could be the results of the decay of super heavy unknown meta-stable particles (with masses above 10^{11} GeV), relic neutrinos, or topological defects.

Super heavy dark matter (SHDM) particles X are the favoured candidates for the first hypothesis [48]. In this scenario, these dark matter particles are produced in the early universe during the reheating period after the inflation phase. Because of their cosmological-long lifetimes, they could decay today by emitting particles known in the Standard Model, among which we find UHE photons and neutrinos. Other candidates in

the hypothesis of super heavy particles are cosmological topological defects [49]. They are predicted to be formed also in the early universe as a result of symmetry-breaking phase transitions.

The annihilation of UHE neutrinos with relic neutrinos has also been proposed to explain the origin of UHECRs. In this scenario known as the Z-burst model [50], the UHE neutrino interacts with the relic neutrino through a Z-resonance. The Z boson decays into fermions as expressed in Eq. 2.6 and could produce hadrons and leptons.

$$\nu_{relic} + \nu_{UHE} \rightarrow Z \rightarrow UHECRs \tag{2.6}$$

Although they have been studied for years, the great majority of Top-Down models has been disfavoured as the expected fluxes from such models are much greater than current limits on the fluxes of UHE photons or neutrinos. However, SHDM models were recently developed [51] [52] and their expected flux of UHE photons are lower than the latest limits on photon fluxes (Fig. 6.8) which contributes to motivate the search for photons.

The study of UHECRs and neutral particles gives the opportunity to probe new physics beyond the Standard Model as the scenarios presented here. For instance, as it will be mentioned in the next chapter in Sec. 3.5, constraints on the mass and lifetime of SHDM particles X can be inferred from the limits on UHE photon fluxes. Also, from the non observation of photons or neutrinos in the Auger data, upper limits on the UHE neutral fluxes originating from the decay of SHDM particles can be derived [53].

2.2.3 Production of neutral particles during the propagation of UHECRs

Besides the production of UHE neutrals particles in Top-Down or Bottom-Up models, photons and neutrinos can also be produced during the propagation of UHECRs when they interact with the cosmic microwave background (CMB) [8]. This is called the Greisen-Kuzmin-Zatsepin effect [9] [10] and impacts the propagation of UHECRs for energies above $\sim 10^{19}$ eV.

In the case of an UHE proton the GZK threshold energy is $\sim 5 \times 10^{19}$ eV. The interaction with CMB photons γ_{CMB} results in a pion production through a Δ^+ resonance (see Eq. 2.7). Indeed, in the rest frame of this proton, due to the Lorentz boost, the low energy CMB photon is seen as an high energy gamma ray with an energy greater than $\sim$150 MeV, which is the threshold energy for the Δ^+ resonance. Following this interaction, the incident proton looses about $\sim 20\%$ of its energy. The proton can undergo several interactions during its propagation before its energy drops below the GZK threshold.

$$\begin{aligned} p + \gamma_{CMB} &\rightarrow \Delta^+ \rightarrow p + \pi^0 \\ p + \gamma_{CMB} &\rightarrow \Delta^+ \rightarrow n + \pi^+ \end{aligned} \tag{2.7}$$

The same effect can also occur for UHE nuclei composed of A nucleons. The interaction in this case is a nuclear photo-disintegration as expressed in Eq. 2.8. The photon is

absorbed by the nuclei A and a lighter nuclei is produced alongside x nucleons N. In this case, only one nucleon carrying an energy of E/A interacts with the CMB photon. Therefore, the threshold in energy for the nuclei to undergo the GZK effect is higher than for protons.

$$A + \gamma_{CMB} \rightarrow (A - xN) + xN \tag{2.8}$$

The pions resulting from the Δ^+ resonance for GZK proton, decay and produced either two UHE photons in the case of neutral pions or UHE neutrinos for charged pions. In the case of nuclei, the produced nucleons can also generate neutral particles: the protons can interact with CMB photons (Eq. 2.7), and neutrons produces neutrinos by decaying. The GZK effect impacts the propagation of UHECRs as well as their energy. It creates a distance limit, the GZK horizon, above which the detection of UHECRs above the GZK threshold is not possible. This limit amounts to a couple of Mpc depending on the nature of the UHECR and its energy. This should result in a suppression at the end of the spectrum of UHECRs, which is observed (Fig. 2.1). The suppression could also be the consequence of the maximal accelerating power reached by sources. In this context, an increased sensitivity of the UHE neutral particle searches reaching the level of the expected GZK fluxes, would allow us to probe the contribution of the acceleration of sources at the end of the spectrum.

Summary

Since their discovery by Hess more than 100 years ago, the knowledge on cosmic rays (nature, energies, arrival directions) is much more important, as illustrated by the measured spectrum and its features. Nevertheless, the question of the sources of UHECRs is still open.

In the context of multi-messenger astronomy, the emission of UHE neutral particles alone or in coincidences with GW events is crucial as it offers the opportunity to identify potential astrophysical sources of UHECRs. The different type of searches for UHE photons and neutrinos above 10^{17} eV performed by UHECR observatories and neutrino observatories were presented. In the future, new facilities will provide opportunities to find sources of neutral particles such as the Cherenkov Telescope Array (CTA) for PeV photons.

Finally, the production of these neutral messengers alongside UHECRs in Bottom-Up (acceleration mechanisms) or Top-Down (non-acceleration mechanisms) models, or during their propagation were detailed. In the next chapter, we estimate the diffuse flux of UHE photons and neutrinos originating from the interactions of UHECRs with the interstellar gas in the Milky Way.

Chapter 3

Diffuse flux of UHE photons from the interactions of UHECRs in the Milky Way

Contents

In the previous chapter, we presented the importance of multi-messenger searches as a way to understand the origin of the high energy cosmic rays and the astrophysical sources they could originate from. We also went through the different processes intervening in the production of the messengers that are UHE neutral particles. In the search for cosmic photons, we are facing some difficulties. As we have seen, high energy photons can be absorbed following their interactions with the different photon fields which limits the detection distances. We also face other diffuse fluxes of high energy photons which can become a background in the search for UHE astroparticle sources. Therefore, the determination of such background fluxes is necessary and has been done in the case of the GZK photon flux [54]. In this chapter, we concentrate on the diffuse UHE photon flux

generated by the interaction of UHECRs with the interstellar gas in the galactic disk.

Indeed, when propagating to Earth, UHECRs can interact with the gas in our Milky Way and produce secondary particles including photons. This could lead to a diffuse flux of photons which eventually constitute a background when searching photons above 10^{17} eV produced in the environment of astrophysical sources mentioned in Sec. 2.2.1. For instance, the Pierre Auger Observatory (Sec 4.2) is sensitive to photons from $\sim 10^{17}$ eV [21] and the knowledge of this cosmogenic flux, coupled with that of the GZK expected photon flux presented in Sec 2.2.2, would allow to evaluate the diffuse flux limiting the detection of UHE photons originating from sources. In this chapter, we give an estimate of the diffuse flux coming from the interactions of cosmic rays in the galaxy above 10^{17} eV, using the UHECR flux and composition measured by the Pierre Auger collaboration and two different interstellar gas distribution models. We also discuss the impact of these results on super-heavy dark matter searches (SHDM), as the diffuse flux computed here can be considered as a floor below which other signals would be overwhelmed. This study, in which I participated in particular to produce necessary inputs concerning the secondary photon production, led to a publication in the Astrophysical Journal [55].

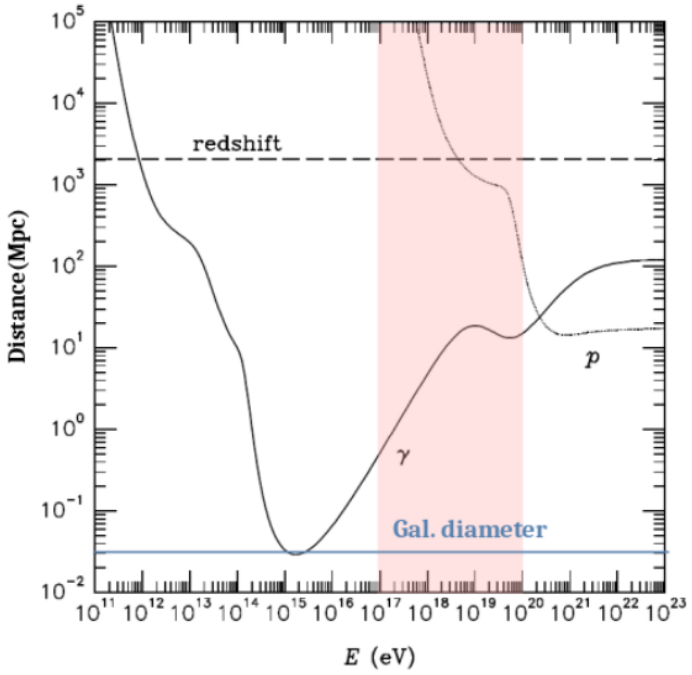

Figure 3.1: The attenuation distance of photons in Mpc as function of the photon energy. The energy range considered in this chapter is shown by the pink area. The galactic diameter is reported by the blue line. Figure taken from [56].

At the high energies considered here, above 10^{17} eV, the cosmic ray flux composition consists of protons and heavier nuclei [57]. Thus, the cosmic rays interact with the interstellar gas through nucleon-nucleon collisions. Following these interactions, UHE photons are produced along with other secondary particles. They essentially propagate through the galaxy without interacting, as their mean free path is greater than the galactic

diameter ($\sim$ 30 kpc) in this energy range, above 10^{17} eV, as shown on Fig. 3.1 [56]. Therefore, the diffuse flux per steradian of UHE photons with an energy E_γ, $\phi_\gamma(E_\gamma, \mathbf{n})$, can be estimated by integrating the emission rate at position $\mathbf{n}$, $q_\gamma(E_\gamma, \mathbf{n})$, per unit of volume and energy along the line of sight as follows :

$$\phi_\gamma(E_\gamma, \mathbf{n}) = \frac{1}{4\pi} \int_0^\infty ds \; q_\gamma(E_\gamma, s\mathbf{n} + \mathbf{x}_\odot) \tag{3.1}$$

where $\mathbf{x}_\odot$ is the position of the solar system in the galaxy, and $\mathbf{n} = \mathbf{n}(l, b)$ is a unit vector on the sphere pointing to the longitude l and latitude b in galactic coordinates. It is important to note that above 10^{17} eV, the observation of UHECRs shows a high degree of isotropy as reported in [58]. This leads to an equally isotropic irradiation of the interstellar gas and therefore to an isotropic emission of UHE photons, hence the $\frac{1}{4\pi}$ factor in Eq. 3.1.

To compute the emission rate $q_\gamma(E_\gamma, \mathbf{x})$, corresponding to the number of photons of energy E_γ produced by UHECRs with energy above $E_0 = 10^{17}$ eV at position $\mathbf{x}$ in the galaxy, we consider:

- $\sigma(E_{CR})$: The inelastic cross-section of the interaction gas-UHECR, depending only on the UHECR energy E_{CR}. The dependency on the target energy is neglected as the nucleus can be considered at rest when looking at the cosmic ray energy range.
- $\Phi_{CR}(E_{CR})$: the UHECR flux with energy E_{CR}.
- $\frac{dN}{dE_\gamma}(E_{CR}, E_\gamma)$: The differential production rate of UHE photons of energy E_γ produced per interaction of an UHECR of energy E_{CR} with the interstellar gas.
- $\rho(\mathbf{x})$: The Milky Way interstellar gas density in nuclei per cm^3 in at position $\mathbf{x}$.

In Eq. 3.2, the summation over j corresponds to the different interstellar gas elements X: molecular and atomic hydrogen, and helium. The summation over i accounts for the different nuclei A present in the UHECR flux.

$$q_\gamma(E_\gamma, \mathbf{x}) = 4\pi \sum_{i,j} \rho_j(\mathbf{x}) \int_{E_0}^\infty dE_{CR} \; \Phi_i(E_{CR}) \; \sigma_{i,j}(E_{CR}) \; \frac{dN_{i,j}}{dE_\gamma}(E_{CR}, E_\gamma) \tag{3.2}$$

In the following, we first discuss the UHE cosmic ray flux and its mass composition, then the different models of interstellar gas distribution are presented. We address the production of UHE photons and finally give the resulting estimate of the diffuse UHE photon flux and discuss the implications on the search for super-heavy dark matter (SHDM).

3.1 The flux of UHECRs

To obtain the cosmic ray flux for a defined group of primaries $\Phi_i(E_{CR})$, we combine the all particle spectrum of UHECRs, $\Phi(E_{CR})$, with the energy-dependent relative abundances of the primaries f_i, giving : $\Phi(E_{CR}) = \sum_i f_i.\Phi_i(E_{CR})$. For the spectrum, we used the one measured at the Pierre Auger Observatory, shown in Fig. 3.2 [59] (left), using the

surface detector (see Sec. 4.2.1). This choice was made considering several arguments. First, the observatory owns the largest cumulated exposure, namely the time-integrated observational capabilities of the detector. It also uses a single type of detector avoiding the combination of measurements and therefore the addition of systematics to the study. Moreover, the primary energy is known calorimetrically as it is measured by the fluorescence telescopes of the observatory (see Sec. 4.2.2). This direct measurement of the energy is independent of the interaction models and assumptions in the mass composition. The uncertainties on the spectrum must be propagated when calculating the diffuse flux.

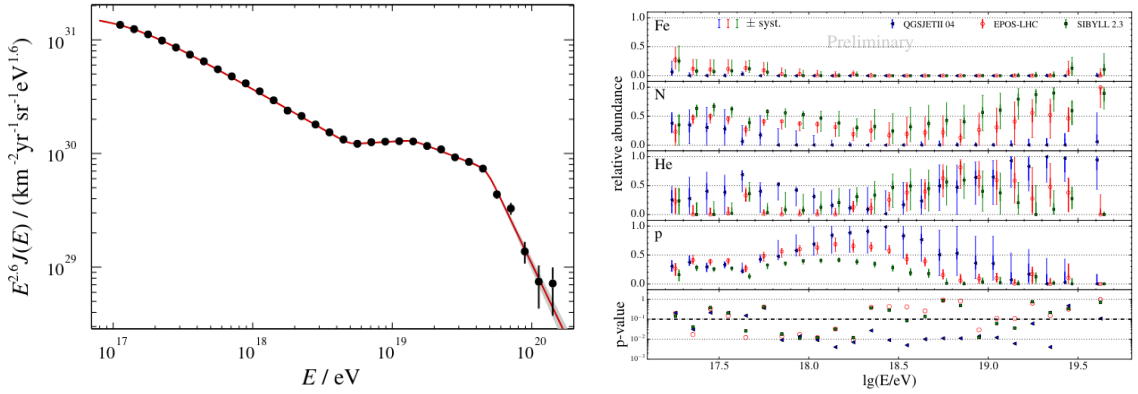

Figure 3.2: Left: The all particle spectrum measured at the Pierre Auger Observatory [59]. Right: Relative abundances of primary groups measured at the Pierre Auger Observatory as function of the primary energy [60], for three hadronic interaction models : EPOS-LHC [61] (red), Sibyll2.3 [62] (green) and QGSJetII-04 [63] (blue).

Concerning the relative abundances of the primary CRs, they are also obtained from measurements carried at the Pierre Auger Observatory [60]. In this study, we consider the interactions between a cosmic ray of type A with a nuclei of type X. At ultra high energies, the spectrum of the cosmic ray flux and its mass composition are obtained via the indirect measurements of extensive air showers, a cascade of particles produced by an UHECR following its interaction with the atmosphere (see Sec. 4.1). Thanks to measurements of X_{max}, the depth of the maximum of the shower development, a robust observable strongly correlated to the mass of the primary cosmic ray, the composition is determined on a statistical basis. In the work published by the Pierre Auger Collaboration in [60] [57], the determination of the mass composition of cosmic rays above $10^{17.2}$ eV is presented. The mass is deduced by comparing the X_{max} distributions with those predicted from EAS MC simulations of different primaries, the comparison being done for different hadronic interaction models (see Sec. 4.1.4). Only four groups of nuclei A are considered in [60]: H, He, CNO and Fe. The same groups are used in this chapter. The four cosmic ray primaries considered interact with the interstellar gas nuclei X composed of H and He: the UHE photons resulting from these collisions are produced by 8 possible interactions. We use the results showed in Fig. 3.2 (right) from [60], where the fractions of the different primary groups are reported as a function of the cosmic ray energy, for three hadronic interaction models, namely EPOS-LHC [61], Sibyll2.3 [62] and QGSJettII-04 [63].

Fig. 3.3 shows the combination of the all particle spectrum with the fractions of the

different nuclei types. The species have been scaled for clarity issues (see legend). The systematic uncertainties arising from both the all-particle spectrum of UHECRs and the fractions of mass groups inferred from the three different hadronic interaction models, are propagated when calculating the estimate of the diffuse flux in Sec. 3.4.

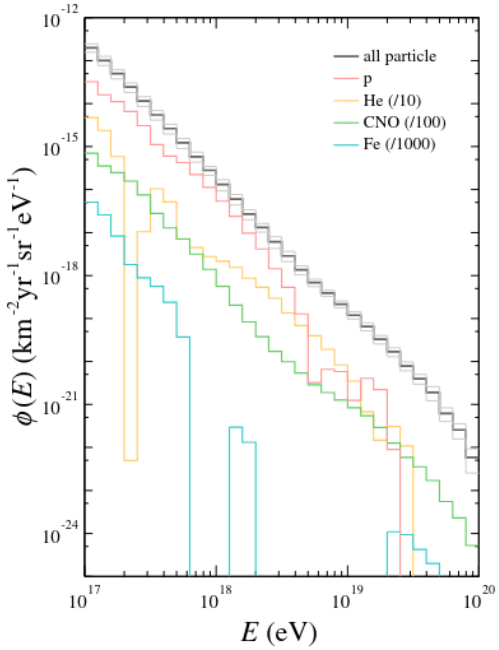

Figure 3.3: The all particle spectrum from [59] (black) combined with the contributions of H (red), He (orange), CNO (green) and Fe (blue) from [60] for the hadronic interaction model Sibyll2.3 [62]. The two grey lines above and below the all particle spectrum indicates the +16% and −16% quantiles of the distribution of the uncertainties.

3.2 Interstellar gas density in the Milky Way

The vast majority of the galactic baryonic matter consists of the interstellar gases. The interstellar gas in the Milky way is mostly composed of Hydrogen and Helium, with a density ratio of about 10 to 1, distributed essentially in the disk. Hydrogen, contributing to most of the interstellar gas mass, can be found in three different forms depending on its temperature: atomic H_I, molecular H_2 and ionised. On the other hand, Helium stays neutral as its first ionisation potential is higher (13.6 eV for H and 24.6 eV for He). The case of ionised hydrogen will not be considered in this work as its contribution is smaller (13.5% of the total hydrogen mass).

The distribution of the H_I component, representing about two thirds of the total interstellar hydrogen mass, is rather constant in the distance range [4-10pc] from the galactic centre and falls at larger distances. The density decreases exponentially in the perpendicular direction to the galactic plane with a scale length depending on the gas temperature. This distribution is known following observations via the 21-cm radio hyperfine line. In

the case of H_2, the observation is not direct. Indeed, a homo-nuclear diatomic molecule like H_2 does not possess a permanent electric dipole moment, and therefore has no simple rotational transition. Thus, the column density of H_2 is inferred through the observations of carbon dioxide (CO) emission lines. Molecules of CO, the second most abundant molecule in the interstellar medium, are excited by their collisions with H_2 molecules, resulting in a correlation between the integrated line intensity of CO lines and the column density of molecular hydrogen. Finally, the distribution of Helium is not really known, being only observable in a specific ionised state. Therefore, it is assumed to follow the hydrogen distribution but with a factor 10%.

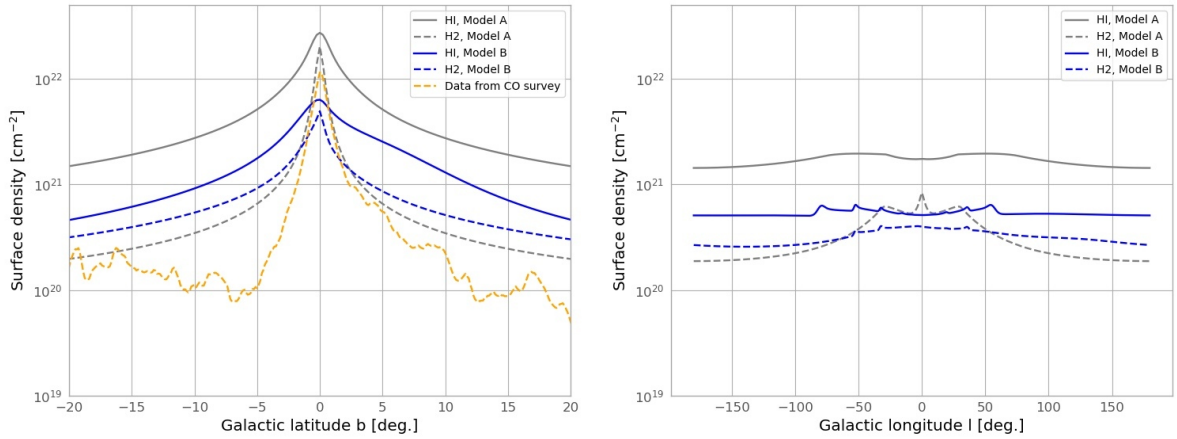

Figure 3.4: Left: The surface density averaged over the galactic longitude l as a function of galactic latitude b for H_I and H_2, for model A in grey and in blue for model B. The surface density of molecular Hydrogen as obtained from the composite survey in [64] is shown by the orange line. Right: The surface density average over the galactic latitude b as a function of galactic longitude l for H_I and H_2 and the two density models.

We used two recent models of gas distribution relying on observations data, and computed the diffuse flux for both. The differences between the results are contributing to the systematics of $\phi_\gamma(E_\gamma, n)$.

The first model considered published in [65], labelled as model A in the following, captures the large-scale characteristics of the distribution without attempting to describe finer details such as filaments and individual clouds. Thus, this distribution is axially and up-down symmetric neglecting features like the spiral arms and the disk wrap of our galaxy. In this model, the gas is concentrated along the galactic plane with a thickness increasing with the distance to the galactic centre r. With r and z being the cylindrical coordinates, the hydrogen density is written as :

$$n(r,z) = n_0(r).\exp\left[-\frac{z^2}{2\sigma_Z^2(r)}\right] \tag{3.3}$$

where $n_0(r)$ is the mid-plane density and $\sigma_Z(r) = H_W(r)/\sqrt{2.\ln 2}$ and $H_W(r)$ is the half width at half maximum of the $z(r)$ distribution. Using a parametrization of $H_W(r)$ and

$n_0(r)$, which can be found in [65], the model describes the three forms of Hydrogen.

The second model of interstellar gas distribution, referred as model B hereafter, was published in [66]. This is a more detailed description with the modelization of the spiral arms as well as the wrapping of the disk. The full parameterisation of the model can be found in [66]. Fig. 3.5 extracted also from [66], shows the surface density maps in solar masses per pc^2 for H_I (left) and H_2 (right).

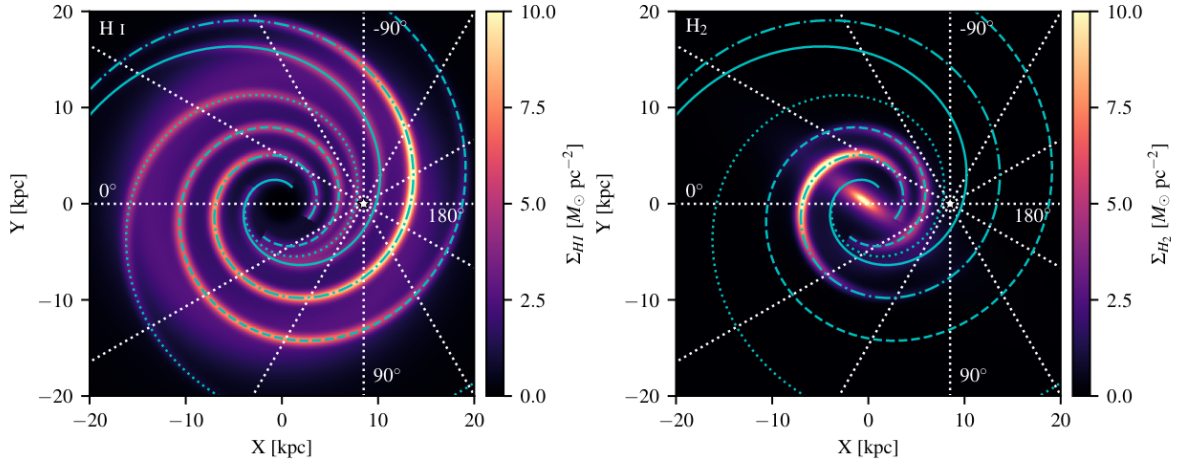

Figure 3.5: Surface density maps for model B. The H_I component is on left and H_2 component is on right. The Sun is marked as a white point and the white-dashed lines mark the longitude grid with 30° step. The blue curves on the surface density maps trace the cores of the spiral arms with each arm marked with a different line style. Figure taken from [66]

The column density averaged over the galactic longitude l (latitude b) as function of the galactic latitude b (longitude l), is reported in left (right) panel of Fig. 3.4 for model A in grey and model B in blue, with plain lines for H_I and dashed lines for H_2. Moreover, the large-scale CO line survey of the Galactic plane and large clouds performed in [64] is indicated by the orange line. They combined several surveys together and obtained a composite survey of the entire Milky Way with an angular resolution ranging from $9'$ to $18'$. Finally, when summing the surface density of H_I and H_2, we observe a difference of the order of a few units of 10^{22} cm^{-2} in the surface density averaged over the galactic longitude between the two density models. Theses differences contribute in the systematics when calculating the photon flux in Sec. 3.4.

3.3 Production of UHE photons

UHECRs interacting with the interstellar medium results in the production of secondary particles. Among those particles are neutral pions π_0, whose most probable decay mode is two photons:

$$\pi^0 \rightarrow 2\gamma \tag{3.4}$$

These π^0 can be produced directly after the collision, but can also be created following

mesons decays such as K, ρ, and η, resulting in an additional flux of UHE photons.

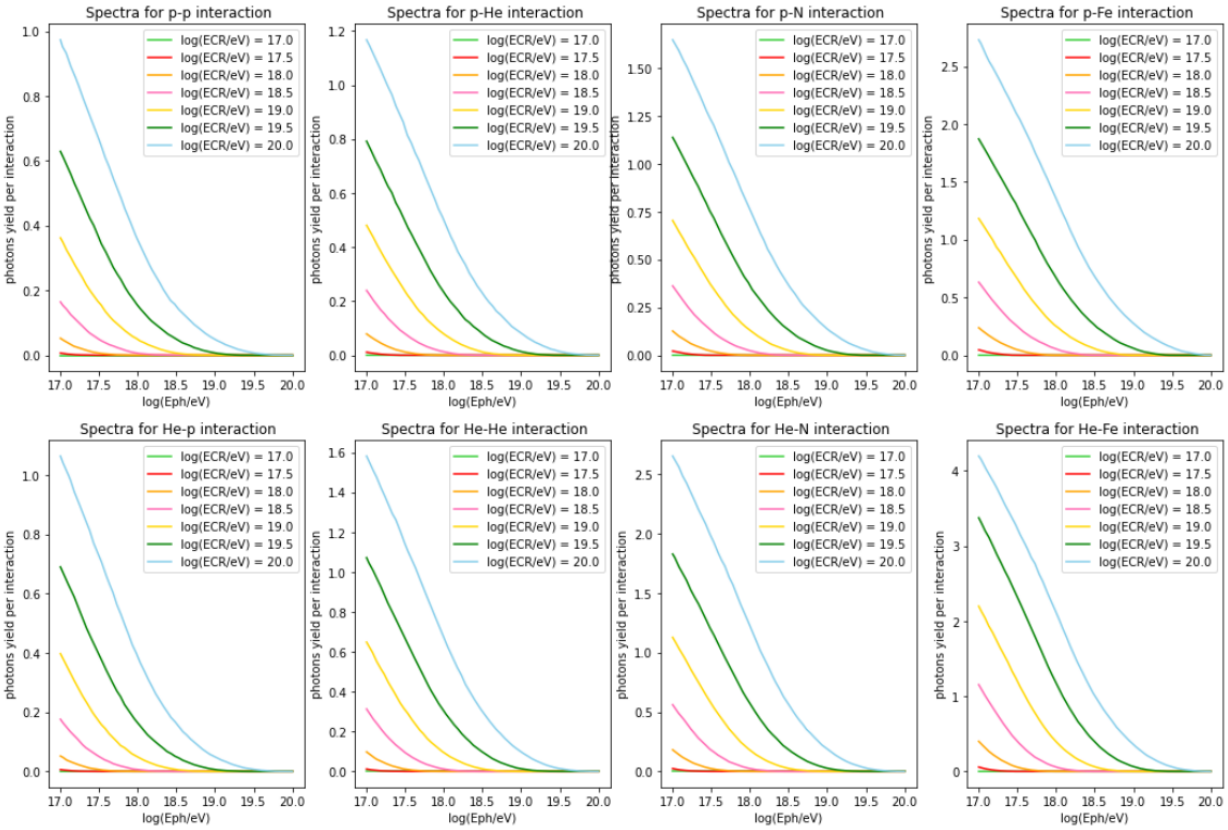

Figure 3.6: The energy spectra of photons obtained using CRMC [67] for the seven cosmic ray energies. The spectra at the top are for Hydrogen targets, those at the bottom for Helium targets.

To obtain the inelastic cross sections $\sigma_{i,j}(E_{CR})$ along with the energy spectra of UHE photons $\frac{dN_{i,j}}{dE_\gamma}(E_{CR}, E_\gamma)$, we use Cosmic Ray Monte Carlo (CRMC) [67]. This package gives access to several cosmic ray event generators that model the production of secondary particles in a hadronic interaction. It also allows the follow-up of the decays of the secondary particles that are likely to produce photons. The hadronic interaction model EPOS-LHC [61] is chosen in this study, but the choice of the hadronic interaction model here is not important as the uncertainties provided by abundances (Fig. 3.2) are dominant in the final determination of the uncertainties on the diffuse photon flux.

Using CRMC, and for each couple UHECR-gas, we simulated $100,000$ collisions for 7 different energies of UHECR, ranging from 10^{17}eV to 10^{20}eV, in steps of 0.5 in logarithm. Thus, we obtained the energy spectra of the photons produced in the interactions, with a chosen bin width of $\Delta\log_{10}(E_\gamma/1eV) = 0.05$. The spectra for the 8 couples (i, j) are reported in Fig.3.6. Moreover, Fig. 3.7 (left) shows the yields of different primaries for three different comic ray energies (10^{18}, 10^{19} and 10^{20} eV), that is to say the mean number of photons of energy E_γ produced during one interaction. For a fixed photon energy, the number of photons produced increases with the CR energy, as expected. On

the other hand, for a fixed cosmic ray energy, the yield depends on the cosmic ray mass. Indeed, during the interaction, only a single pair of nucleons contributes. The energy per nucleon decreasing when the element gets heavier, as it is divided by the atomic number A, the number of photons produced is higher for higher CR energies and lighter masses. The inelastic cross sections $\sigma_{ij}(E_{CR})$, obtained also with CRMC, are reported in figure 3.7 (right) as function of the CR energy. A log-linear interpolation was perfomed between the different cosmic ray energies. The continuous lines are for Hydrogen targets and dashed lines for Helium targets.

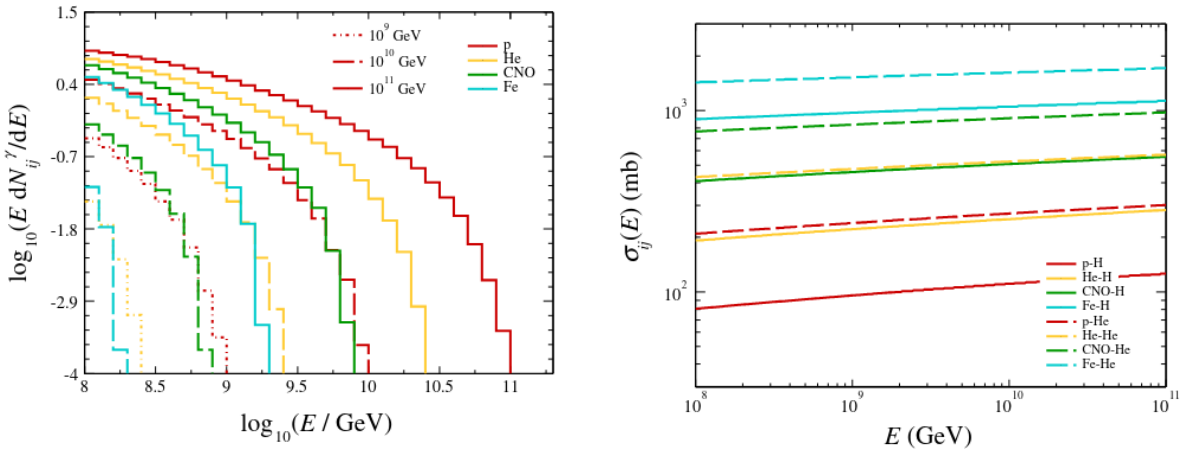

Figure 3.7: Left: The photon yields $\frac{dN_{i,j}}{dE_\gamma}(E_{CR}, E_\gamma)$ obtained with CRMC, for different cosmic ray energies and UHECR masses. Right: The inelastic cross sections $\sigma_{i,j}(E_{CR})$ obtained with CRMC, as function of the cosmic ray energy, for each couple (i,j) of cosmic ray and gas element.

3.4 Estimate of the diffuse flux of UHE photons

By combining the various ingredients introduced previously in this chapter in Eq. 3.1, then Eq. 3.2, we obtain the diffuse flux of UHE photons. These results are obtained with two different codes (one in C++, one in Python) developed inside the team working on this study. It allows performing several checks for the different stages of the computation. Consistent results were found.

The obtained diffuse photon flux for each model of interstellar gas distribution are reported in Fig. 3.8. As expected, the flux is concentrated along the galactic plane following the distribution of the interstellar gas, reaching $\simeq 8.7 \times 10^{-2}\text{km}^{-2}\text{yr}^{-1}\text{sr}^{-1}$ when averaged over $|b| < 5°$ in case of model A ($\simeq 3.2 \times 10^{-2}\text{km}^{-2}\text{yr}^{-1}\text{sr}^{-1}$ for model B).

The energy spectrum has a similar slope as the UHECR spectrum, but is down-shifted by a decade earlier. When averaged over a 5° band around the galactic plane, we find that its value is about 10^{-5} that of the UHECRs when considering energy thresholds between 10^{17} to 10^{18} eV. For higher thresholds however, the spectrum of UHE photons becomes steeper, and this ratio decreases to 10^{-6} for thresholds above 10^{19} eV, before dropping

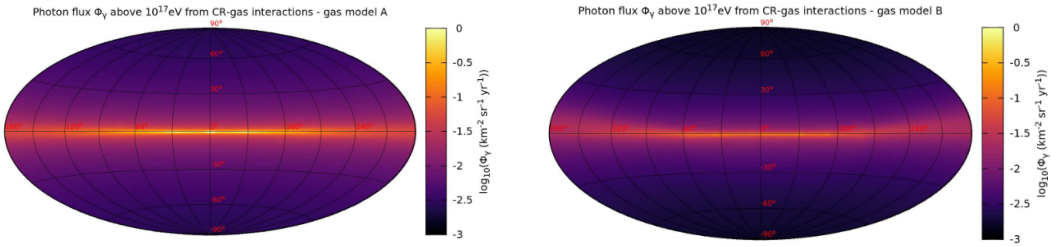

Figure 3.8: The diffuse flux UHE photons with $E_\gamma > 10^{17}$ eV in Galactic coordinates, for model A (left) and model B (right).

sharply at highest energies.

3.4.1 Comparison to searches for a diffuse photon flux

The calculated photon fluxes can be compared to the results from searches for a diffuse flux above 10^{17} eV, performed by several ground array experiments like EAS-MSU [68], KASCADE-Grande [69], Telescope Array [70], and the Pierre Auger Collaboration [71]. The upper limits for each of them are reported of Fig. 3.9 by orange dots, black dots, pink triangles and blue squares respectively, while our results correspond once again to the blue and grey bands. To compare to upper limits on the diffuse fluxes illuminating the whole field of view of the observatory considered, it is needed to normalize the expected fluxes over the whole sphere, as showed in Eq. 3.5. The limits obtained by the different observatories appear to be between 2.5 to 3 orders of magnitude above our expectations for energy thresholds between 10^{17} and 10^{18} eV, and even higher for larger thresholds.

$$\Phi_\gamma(E) = \frac{1}{4\pi} \int_E^\infty \int_{4\pi} d\mathbf{n}.\phi_\gamma(E', \mathbf{n}) \tag{3.5}$$

In Fig. 3.9, the orange band represents the expected GZK photon flux arising from the interaction of UHECRs with the photon fields present in the universe, as explained in Sec. 2.2.2, for a mixed composition fitting the Pierre Auger Observatory data [54], namely the measured energy spectrum and mass composition. The systematic uncertainties arising from these measurements lead to the orange band.

For energy thresholds between 10^{17} and 10^{18} eV, we expect the cosmogenic flux originating from the interactions of UHECRs with the interstellar gas to be the dominant one, while the GZK takes over for higher thresholds.

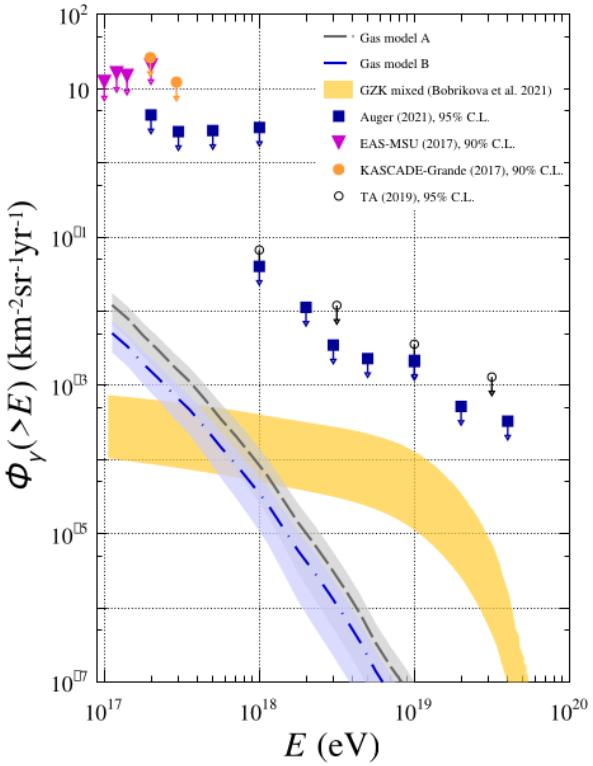

Figure 3.9: Upper limits on diffuse photon fluxes reported by [68] (pink triangles, EAS-MSU), [69](filled orange circles, KASCADE-Grande), [70](open circles, Telescope Array), and [71](dark blue squares, Auger). Expected fluxes from UHECRs interactions with the gas distribution in the Galaxy are shown as the grey dashed line (model A) and grey dashed- dotted line (model B), as well as from UHECRs interactions with background photon fields (GZK mixed) estimated in [54].

3.4.2 Comparison to a search for point-like sources

The calculated photon fluxes can also be compared to the results of other searches for UHE photons fluxes above 10^{17} eV. The directional limits reported in [24], for energies ranging from $10^{17.3}$ to $10^{18.5}$ eV, come from a search for point-like sources in the exposed sky of the Pierre Auger Observatory (zenith angles below 60°). This is performed by reducing the background of hadronic UHECRs using mass-sensitive observables in a multivariate analysis, and looking for an excess in a specific direction. These limits averaged over a 5° band around the galactic plane are reported as the red line in Fig. 3.10, as function of the galactic longitude l. To compare the results of our study to these results, we convert our directional fluxes into a collection of point-like sources detected through the point-spread function of the Pierre Auger Observatory f_{θ_0} (Fisher-von Mises function). This is equivalent to applying a Gaussian filter on the sphere with an angular scale of $\theta_0 = 1°$, as seen in Eq. 3.6, describing the response of the detection device. The integration range of the photon energy is the one mentioned before, and b ranges from -5 to 5°. The fluxes in this work are computed using the EPOS-LHC hadronic interaction model [61]. They are reported for model A and B by the grey and blue bands respectively. The bands depict the systematics coming both from those in the UHECRs spectrum and in the different

hadronic interaction models used in the determination of the mass composition. They are about three orders of magnitude below the limits reported in [24]. The propagation of uncertainties can be found in the paper we published [55]. One can conclude easily that these limits cannot be reached with current observation capabilities. Although these fluxes could be improved by a factor two or three by collecting more data at the Pierre Auger Observatory, the conclusion would be the same. Moreover, the fluxes reported here are for a E^{-2} photon spectrum, the difference would be higher for steeper spectra.

$$\psi_\gamma(l) = \frac{1}{2.sin(5)} \int dE \int dsin(b) \int d\mathbf{n}'.f_{\theta_0}(\mathbf{n},\mathbf{n}')\phi_\gamma(E,\mathbf{n}) \tag{3.6}$$

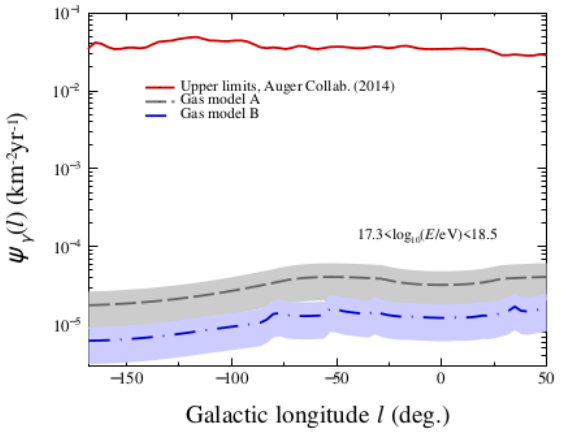

Figure 3.10: The directional photon fluxes averaged over an 5°-band along the galactic plane, when converting the fluxes into a collection of point-like sources detected through the point-spread function of the Auger Observatory. The energy range considered ranges from $10^{17.3}$ to $10^{18.5}$ eV and the hadronic interaction model used is EPOS-LHC. Dashed: gas model A. Dotted-dashed: gas model B. Continuous red line: upper limits at 95% confidence level obtained at the Pierre Auger Observatory [24].

3.5 Implications for the search of SHDM

During the period of reheating after the inflation phase of the universe, the creation of super-heavy particles X could take place and in this scenario, these X particles are possible candidates for the nature of dark matter. The production of UHE photons following the decay of these SHMD particles could occur if these particles have a long enough life-time (of the order of the age of the universe, or greater). Such cosmological-long lifetimes cannot be explained by pertubative mechanisms. However, they could occur when the particles are protected from decays in the perturbative domain, but do disintegrate by what is called instanton non-perturbative effects [72]. This mechanism produces small effects in weakly coupled theories and provides meta-stable particles X of life-time τ_X

which can produce secondary standard model particles such as photons.

The region between 10^{17} to 10^{18} eV, where the diffuse photon flux evaluated in this work is above the one expected from GZK photons, is of interest [21] (Fig. 4.21). Indeed, it can been seen as a floor that could prevent probing sources of UHE photons, in particular in the galactic disk. It could also hide indications on the presence of this SHDM decaying today generating a photon flux ϕ_γ^{DM} in the direction of the galactic centre where the density of dark matter is more important. In the field of SHDM searches, a photon flux in this peculiar direction has important implications. Depending on the mass of the super heavy particle M_X, the photon flux can be translated into a ceiling for the life-time τ_X region of this particle. The expected photon flux from these decays can be obtained by integrating the position-dependent emission rate per unit volume and energy along the direction $\mathbf{n}$ as [73]:

$$\phi_\gamma^{DM}(E, \mathbf{n}) = \frac{1}{4\pi M_X \tau_X} \frac{dN}{dE} \int_0^\infty ds . \rho_{DM}(\mathbf{x}_\odot + s\mathbf{n}) \tag{3.7}$$

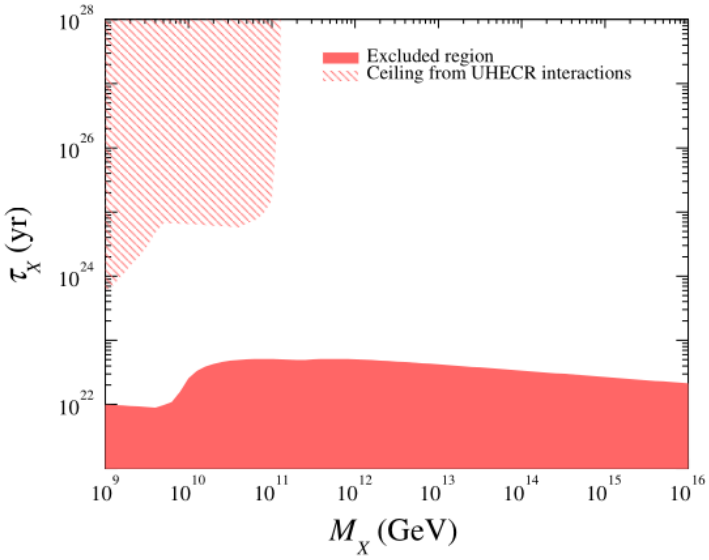

Figure 3.11: Allowed region of mass and life-time of SHDM particles decaying into standard-model ones. The filled red region is excluded from the upper limits in UHE photon fluxes. The hatched one corresponds to the ceiling region inferred from the limits computed in this chapter.

In Eq. 3.7, ρ_{DM} is the energy-density profile of dark matter in the galaxy, and $\frac{dN}{dE}$ represents the energy spectrum of UHE photons produced in the decay which depends on the hadronization process. In this work we considered the Navarro-Frenk-White profile found in [74] where it was shown with N-body simulations that dark matter haloes have a universal density profile that can be fitted by a double power low. The profile is normalised so that $\rho(x_\odot) = 0.3$ Gev.cm^{-3}. In [75], it is shown that the spectra of the final state particles, varies as $E^{-1.9}$, and we use this energy dependence in the following.

It is possible to infer constraints in the (M_X, τ_X) plane from the limits on UHE photon fluxes by requiring that $\phi_\gamma^{DM}(E)$, the flux presented in Eq. 3.7 averaged over all directions $\mathbf{n}$, is smaller than the limits. For an upper limit at a certain energy threshold, one can scan the value of M_X in order to obtain a lower limit on the lifetime τ_X. By repeating the procedure on all energy thresholds, we obtained a collection of excluded regions of (M_X, τ_X) whose sum is reported as the red area on Fig. 3.11.

Finally, by scanning M_X we can also determine the corresponding τ_X for which $\phi_\gamma^{DM}(E) < \phi_\gamma(E)$, meaning that the flux originating from dark matter is overwhelmed by the cosmogenic photon fluxes. This results in a ceiling region showed in Fig. 3.11 as the pink hatched area. The ceiling affects masses up to 10^{11} GeV, which corresponds to the cut-off in the cosmogenic photon fluxes. While masses below 10^{10} GeV are constrained by the photon flux discussed in this chapter, for masses above this threshold the GZK expected photon flux from [54] takes over. In the end, a large region of the plane remains unaffected by the ceiling.

3.6 UHE neutrinos from UHECR interaction in the Milky Way

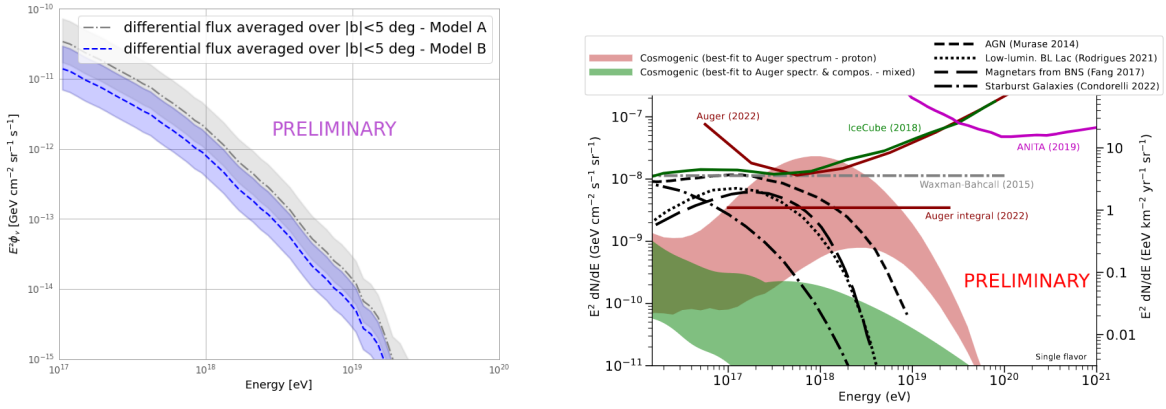

Figure 3.12: Left: All-flavour differential UHE neutrino flux above 10^{17} eV, averaged over $|b| < 5°$, for model A in grey and B in blue. Right: Latest results on the search for UHE neutrinos [21]: the limits set by IceCube [22], ANITA [23] and Auger [21] are displayed with the expectations from cosmogenic and astrophysical production of neutrino: the red (green) band represents the expected cosmogenic neutrino flux for a pure proton (mixed) UHECR flux composition fitting the Auger data.

As stated in the first chapter of this manuscript, UHE neutrinos could also be produced in the environments of energetic astrophysical sources, by top-down mechanisms, or during their propagation when interacting with CMB photons. Similarly as photons, the diffuse neutrino flux following the interactions of UHECRs with the interstellar gas can also act like a background in the search for UHE neutrino sources. In consequence, a similar study can be performed for UHE neutrinos above 10^{17} eV produced by the decays of charged

pions after the interaction with the gas. Eq. 3.8 shows their most probable modes of decays:

$$\begin{aligned} \pi^+ &\rightarrow \mu^+ + \nu_\mu \\ \pi^+ &\rightarrow e^+ + \nu_e \\ \pi^- &\rightarrow \mu^- + \bar{\nu_\mu} \\ \pi^- &\rightarrow e^- + \bar{\nu_e} \end{aligned} \tag{3.8}$$

Although no ν_τ neutrinos are produced following the interaction of the primary cosmic ray with the gas, the oscillations of the neutrinos flavours during their propagation results in a flux of ν_τ and $\bar{\nu_\tau}$ different from zero when arriving at Earth. Neutrinos are produced in a defined flavour state which is a superposition of eigen states of neutrino mass. This superimposed state is not stationary and evolves with time. The mixing probabilities of neutrino flavours during the propagation to Earth are calculated with the Pontecorvo–Maki–Nakagawa–Sakata (PMNS) matrix with the assumption that the distances travelled are large with respect to the oscillations lengths. The energy spectra of all six kinds of neutrinos were produced with CRMC in the same way as in the photon case.

The number of neutrinos per interaction is the only changing parameter in the computation of the diffuse flux. Accordingly, the differential all-flavour neutrino flux above 10^{17} eV and averaged over $|b| < 5°$ is displayed in Fig.3.12 (left) for the two models of interstellar gas density. The latest upper limits on UHE neutrino fluxes set by the IceCube [22], Pierre Auger [21] and ANITA [23] collaborations are shown in the right panel along with neutrino flux expectations from cosmogenic and astrophysical models of neutrino production. The differential flux obtained in this study lays below 3 to 4 orders of magnitude below the limits between 10^{17} eV and 10^{18} eV, and more at the highest energies. The diffuse flux obtained is also not dominant with respect to other expectations from cosmogenic production of neutrinos. In terms of observational capabilities, the conclusion is similar to the one inferred from the computation of the UHE photon flux in Sec.7.2.

Summary

In this chapter we estimated the diffuse UHE photons flux, above 10^{17} eV, originating from the interactions of UHECRs with the interstellar gas in the Milky Way. The spectrum of UHECRs and the relative abundances of the four groups of nuclei are obtained from Auger results. The diffuse photon flux is obtained for two interstellar gas density models. The mean number of UHE photons of energy E_γ produced in each interaction UHECR-gas are obtained using CRMC [67], a cosmic ray event generator allowing the follow-up of secondary particles.

The computed flux is compared to the results of other searches for a diffuse photon flux and is found to be 2.5 to 3 orders of magnitude below upper current limits which is not reachable with today's observatory capabilities. Another important result is that the flux computed in this work is greater than the one expected from GZK interactions in the energy range between 10^{17} and 10^{18} eV. Constraints on the lifetime τ_X

and mass M_X of SHDM particles can be inferred by identifying the regions for which the photon flux from dark matter decay is overwhelmed by the cosmogenic photon fluxes. Finally, the flux created by the interactions of UHECRs in the galactic disk affect masses up to 10^{11} GeV before the GZK photon flux takes over.

The same flux computation is performed and still ongoing for the diffuse flux of UHE neutrinos, also produced in the interaction of UHECRs with the interstellar gas. The obtained differential fluxes for the two gas density models are several orders of magnitude below the latest experimental upper limits. The results also lay below the expectations of cosmogenic and astrophysical production of neutrinos.

Chapter 4

The search for UHE photons at the Pierre Auger Observatory

Contents

The search for photons at ultra high energies, and neutral particles in general, is motivated by the models describing the origin of UHECRs (Sec. 2) which predict the production of neutral particles alongside the cosmic rays in astrophysical sources or during their propagation. As they are not deflected by magnetic fields they are great messengers

to study the most energetic objects in the universe. Up to now, photons with energies of $\sim 10^{15}$ eV have been detected [76], but over this value no UHE photons have been identified so far. The UHE photon flux originating from the interactions of UHECRs in the galactic disk (Sec. 3), as well as the GZK photon flux, are possible backgrounds in the search for UHE photons from astrophysical sources. Moreover, unlike neutrinos, the search for UHE photons has to take into account their absorption by the different photon fields permeating the universe. This limits the distance horizon for the observations to about 30 kpc at 10^{15} eV with an increase to about 10 Mpc between 10^{19} and 10^{20} eV (see Fig. 3.1).

As mentioned in Chap. 2, the cosmic ray flux falls with increasing energy and the study of UHECRs is feasible only via the detection of extensive air showers. In this chapter, simple models describing the EAS development in the atmosphere and the underlying physics are presented. The Pierre Auger Observatory has been designed to detect EAS: the deployment of a surface detector and a fluorescence detector allows a high level quality for the reconstruction of these showers. Both the detection of the EAS particles at ground, of the fluorescence light by the telescopes, and the reconstruction of the properties of the primary cosmic ray are presented. Then, the identification of UHE photons among the events detected at the observatory is discussed. The search relies on the development specificities of photon-induced EAS with respect to nuclei-induced showers. Finally, the status of the photon search in the Pierre Auger Collaboration is reviewed.

4.1 Extensive air showers

In 1933, Rossi had concluded that cosmic rays produced secondary particles when entering the Earth's atmosphere [77]. The discovery of extensive air showers was made in the late 1930s and is credited to Pierre Auger. With his collaborators, he deployed several Geiger-Müller counters with a 300 m spacing [5]. They observed that the rate of coincidences was higher than expected between the counters. Following these observations, Auger and his group demonstrated using the newly developed ideas of quantum electrodynamics (QED), that the incoming particles which had produced these extensive showers should have an energy of $\sim 10^{15}$ eV. Prior to these studies, it was known that the energy range of cosmic rays could extend to 10 GeV. The impact in the field was huge as the energy scale was extended by about 5 orders of magnitude. This discovery was made possible by the important improvement of coincidence techniques [78] and a new generation of Geiger-Müller counters with better timing resolution [79].

In 1934, Bethe and Heitler described the processes of cascade occurring in air showers with QED [80]. Three years later, Bhabha and Heitler formulated the cascade in terms of pair production and Bremsstrahlung processes [81]. This was completed the same year by Carlson and Oppenheimer [82] when they implemented the energy losses of electrons by ionisation using diffusion equations. Their calculations were in agreement with the experiment carried by Regener and Pfotzer in 1935 [83] in which they observed an unexpected high rate of threefold coincidences. The work of Auger and his group allowed a better understanding of air showers. The presence of muons (discovered in 1937), and

hadronic particles in the showers was established just a couple of years after the discovery.

Nowadays, it is known that the spectrum of UHECRs extends to energies up to 10^{20} eV. Moreover, the electromagnetic processes occurring along the development of the showers they create in the atmosphere are well understood, while it is not the case for hadronic processes. In the next sections a simple model describing the development of electromagnetic showers is presented. We also discuss its extension to realistic air showers, which contain hadronic cascade processes. These models highlight the physics involved. However, a detailed description of this complex phenomenon is only possible through simulations of EAS using Monte-Carlo codes. This is what is addressed in the last part of this section.

4.1.1 Electromagnetic air shower

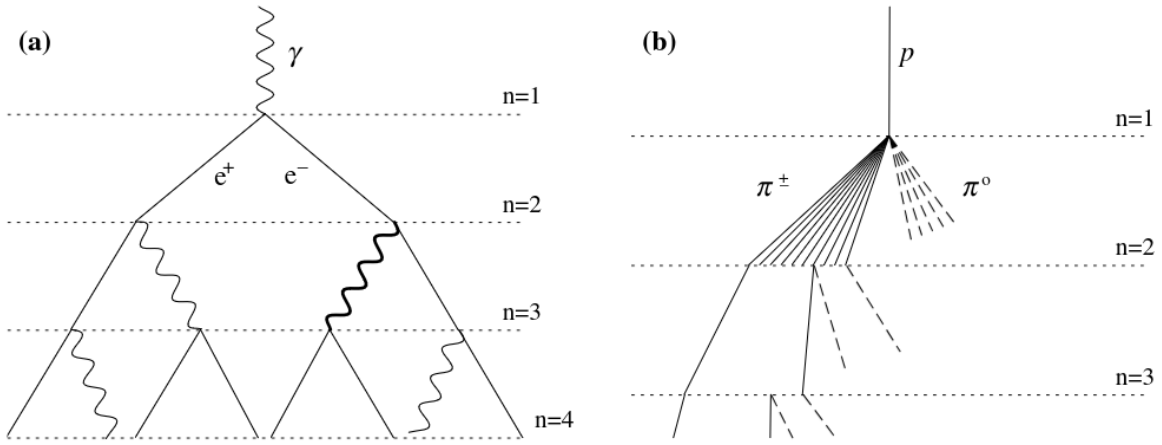

Figure 4.1: Left: illustration of the Heitler model for electromagnetic showers. Right: illustration of the extension of the Heitler model for an EAS initiated by a proton. Taken from [84].

A simple model of electromagnetic showers developed by Heitler [6] [84], gives an accurate description that highlights their main features relying on Bremmstrahlung processes and pair production of e^+/e^-. Electrons, positrons and photons are assumed to interact after travelling a fixed distance $d = \lambda_r \ln 2$, related to the radiation length λ_r in the medium. The radiation length is assumed to be the same for all particles, and $\lambda_r = 37$ g/cm^2 in air. At each interaction the energy is assumed to be equally distributed between the two resulting particles. The first four steps of the Heitler model for electromagnetic showers are shown in Fig. 4.1 (left) for a photon-initiated shower. After n steps, the resulting number of particles is $N = 2^n$. The size of the shower ceases to grow when the energy of individual particles drops below what Heitler calls the critical energy ξ_c^{EM}, corresponding to the threshold at which the energy loss following the interaction exceeds the radiation loss. In other words, the individual energy of particles is too low for Bremmstrahlung or pair production processes. In air, $\xi_c^{EM} = 85$ MeV.

The maximum size of the shower is reached when the particles get to the critical energy ξ_c^{EM} at step n_c. The corresponding atmospheric depth X_{max} is reached when the

number of particles is at its maximum value N_{max}. If one considers a shower initiated by a particle with energy E_0, then:

$$E_0 = \xi_c^{EM} N_{max} \tag{4.1}$$

The maximum depth X_{max} is determined by obtaining the number of splitting necessary for the energy of particles to drop below ξ_c^{EM}. As $N_{max} = 2^{n_c}$ and $X_{max} = dn_c$, from Eq. 4.1 one gets:

$$E_0 = \xi_c^{EM} 2^{n_c} \Rightarrow X_{max} = \lambda_r \ln\left(\frac{E_0}{\xi_c^{EM}}\right) \tag{4.2}$$

This rather simple model was compared with shower simulations and the resulting maximum depths is in good agreement. There are several limitations to this approach. The model overestimates the number of electrons with respect to photons and predicts the electrons size to be $N_e = \frac{2}{3} N_{max}$. This estimation is too large for the main reason that during the Bremsstrahlung processes several photons are emitted. Nevertheless, the Heitler model is able to highlight the two main features of electromagnetic shower: the maximum depth of the shower X_{max} is proportional to the primary energy logarithm $\ln(E_0)$ and the maximum number of particles reached at X_{max}, is proportional to E_0.

4.1.2 Hadronic air shower

The hadronic interactions taking place in a nucleus-induced showers can be approximated in a similar way. When a nucleus interacts in the atmosphere several pions are created: the neutral pions π^0 most probable mode of decay is two photons, which in turn generate electromagnetic showers like those described previously, on the other hand, the charged pions $\pi^{\pm}$ generate another generation of pions. Similarly to the case of electromagnetic showers, the cascade process stops when the pions energy reach the critical threshold ξ_c^{π}, when the probability of interaction is lower than the probability for pions to decay into muons and neutrinos (Fig. 4.1, right panel).

At each step of the development, each charged pion generates N_{ch} other charged pions along with $\frac{1}{2} N_{ch}$ neutral pions. While the latter initiate electromagnetic showers, $\pi^{\pm}$ travel through a fixed layer of atmosphere of $\lambda_I \ln 2$, where λ_I is the interaction length of strongly interacting particles and is assumed constant at $\lambda_I \simeq 120$ g/cm^2. After n interactions, the number of charged pions is $N_{\pi} = N_{ch}^n$. Considering a primary proton with energy E_0, each particle at step n has an energy expressed by:

$$E_{\pi} = \frac{E_0}{(\frac{3}{2} N_{ch})^n} \tag{4.3}$$

The pions reach the critical energy ξ_c^{π} after n_c interactions. n_c is inferred from Eq. 4.3.

$$n_c = \frac{\ln\left(\frac{E_0}{\xi_c^{\pi}}\right)}{\ln\left(\frac{3}{2} N_{ch}\right)} \tag{4.4}$$

The primary energy E_0 is distributed between the electromagnetic and the hadronic component of the shower. The energy of electromagnetic shower component is carried by

N_{max} particles while the rest is carried by the N_π charged pions. These pions eventually decay into one muon each after their individual energy drops below ξ_c^π. Therefore, $N_\mu = N_\pi$ where N_μ is the total number of muons in the shower. Thus, the total energy can be written linearly as function of the respective critical energies as:

$$E_0 = N_{max}\xi_c^{EM} + N_\mu \xi_c^\pi \tag{4.5}$$

The number of muons is $N_\mu = N_{ch}^{n_c}$ and can be expressed in log-scale with the help of Eq. 4.4:

$$\ln N_\mu = n_c \ln N_{ch} = \ln\left(\frac{E_0}{\xi_c^\pi}\right)\frac{\ln N_{ch}}{\ln\left(\frac{3}{2}N_{ch}\right)} = \beta \ln\left(\frac{E_0}{\xi_c^\pi}\right) \tag{4.6}$$

where $\beta = \ln N_{ch}/\ln\left(\frac{3}{2}N_{ch}\right)$ and $N_\mu = (E_0/\xi_c^\pi)^\beta$. The energy E_{EM} carried by the electromagnetic particles can be obtained as function of the critical energy of pions ξ_c^π and the primary energy of the proton. By combining Eq. 4.5 and Eq. 4.6 we obtain:

$$\begin{aligned} E_0 &= N_{max}\xi_c^{EM} + N_\mu \xi_c^\pi \\ \Rightarrow E_0 &= E_{EM} + \xi_c^\pi (\frac{E_0}{\xi_c^\pi})^\beta \\ \Rightarrow E_{EM} &= E_0(1 - (\frac{E_0}{\xi_c^\pi})^{\beta-1}) \end{aligned} \tag{4.7}$$

The depth corresponding to the maximum development of the shower is reached when the number of particles is maximum. Here, the estimation of X_{max} is done by determining only the maximum depth of the electromagnetic part of the shower. This approximation is quite accurate. Indeed, from Eq. 4.7, the fraction of the primary energy going into the electromagnetic part is estimated at 70% at $E_0 = 10^{14}$ eV and 90% at 10^{17} eV, taking $\xi_c^\pi = 20$ GeV. Moreover, for the sake of keeping the model simple, only the electromagnetic showers initiated by the first generation of neutral pions are used. These assumptions result of course in an under-estimation of X_{max}, as the other electromagnetic sub-showers created from the second generation are not accounted for. The first interaction takes place at the atmospheric depth $X_1 = \lambda_I \ln 2$. As stated previously, the number of neutral pions is $N_{ch}/2$ which all decay, giving N_{ch} photons. Each photon initiates an electromagnetic shower of energy $E_0/(3N_{ch})$. The maximum depth for a electromagnetic shower of this energy starting at depth X_1, inferred from Eq. 4.2, is:

$$X_{max}^p = X_1 + \lambda_r \ln\left(\frac{E_0}{3N_{ch}\xi_c^{EM}}\right) \tag{4.8}$$

In this simple model, the energy dependence of the hadronic cross sections and the multiplicity of hadronic interactions are not accounted for. Both increase with the particle energy and, therefore, tend to reduce the depth of maximum shower developments. Indeed, an higher hadronic cross section means that the shower will start earlier in the atmosphere. In the same way, if more pions are produced, their individual energy is smaller and the sub-showers they generate have shorter development. Concerning the case of nuclei, the *superposition model* is used: a nucleus-induced shower is the sum of A showers of energy E_0/A, where A is the number of nucleons. Accordingly, from Eq. 4.6

and Eq. 4.8 we express the muon number N_μ^A and the maximum depth X_{max}^A of a nuclei shower:

$$X_{max}^A = X_{max}^p - \lambda_r \ln A \qquad (4.9)$$
$$N_\mu^A = A^{-\beta} N_\mu^p$$

Therefore, nucleus-induced showers have more muons than proton showers resulting in a smaller X_{max} by $\lambda_r \ln A$, not depending on the primary E_0. Finally, another important point has been neglected in the model. All interactions have been considered perfectly elastic with all the energy is going into the production of new particles. However, in realistic hadronic interactions, a leading hadron tends to take an important fraction of the available energy. As less energy is given to electromagnetic showers, the resulting muon content is shown in [84] to be more important because β is reduced. In the same way, X_{max}, estimated from the first generation of neutral pions, should be smaller.

The description of EAS induced by a nuclei, based on an extension of the Heitler model of electromagnetic showers, is in good agreement with simulations. Important features can be extracted. Firstly, the primary energy can be expressed as a linear combination of the electron and muon numbers (Eq. 4.5). Secondly, as shown by Eq. 4.6 the muon number N_μ increases with the energy following a power law of index $\beta < 1$. When considering the inelasticy of hadronic interactions, N_μ grows faster with the energy as β is larger. Finally, for nuclei induced showers, the muon content is more important and results in a smaller X_{max} as less energy is given to the electromagnetic part of the shower.

4.1.3 Lateral and longitudinal profiles of particles in EAS

As the majority of the primary energy goes into the electromagnetic component, the shower X_{max} is mainly determined by the electromagnetic X_{max}. The left panel of Fig. 4.2 shows the longitudinal profiles, namely the number of particles as function of the atmospheric depth, for secondary photons (blue), electrons (red), muons (green) and hadrons (black) obtained from a simulated shower (see next section). A multiplicative factor is applied for clarity (see legend). As expected from the Heitler model whose conclusions were tested with simulations [84], the most numerous particles are photons.

The right panel of Fig. 4.2 shows the lateral distributions of these particles, i.e. the particle density as function of the distance from the shower core. These are mostly determined by the characteristics of the interactions: hadrons and muons are produced with larger transverse momentum and tend to travel further from the core with respect to electromagnetic particles and they undergo less scattering, resulting in a less steeper profile.

The relative contribution of each type of particles in the shower is dependent on the nature of the cosmic rays: the hadronic channel is more fed when the primary cosmic ray is heavier. The longitudinal and lateral developments being different for each, these characteristics are exploited in the search for UHE photons (Sec. 4.3).

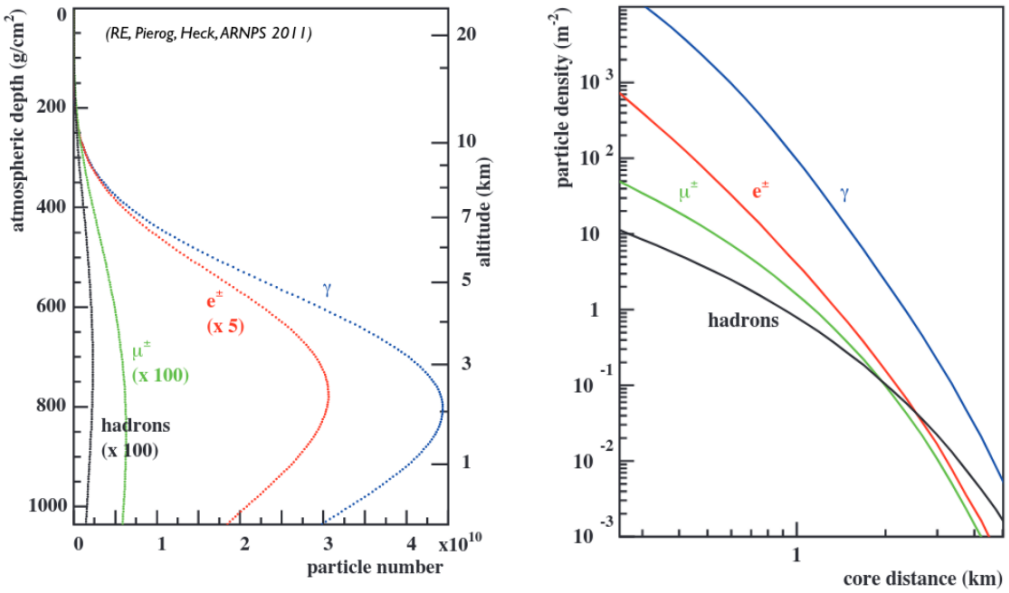

Figure 4.2: Left: Longitudinal distributions of photons (blue), electrons (red), muons (green) and hadrons (black) in a simulated EAS. Right: Lateral distributions of photons (blue), electrons (red), muons (green) and hadrons (black) in a simulated EAS. Taken from source.

4.1.4 Air shower simulations

A detailed description of the development of EAS requires the use of Monte-Carlo simulations. These simulations of EAS are mandatory to understand and interpret UHECR data. For instance, up to now, the nature of the primary can only be inferred by using the information collected from libraries of simulated showers. The electromagnetic and weak interactions are well understood and correctly described by quantum electrodynamics within the Standard Model. In this case, the interactions can be computed analytically in the perturbative domain. The case of strong interactions in the frame of quantum chromodynamics (QCD) is more difficult to handle: only interactions with large momentum transfers can be calculated analytically and phenomenological parameterisations must be performed to describe interactions with lower momenta. There is also a lack of experimental data from particles accelerators for interactions at ultra-high energies. The maximal energy reached at the Large Hadron Collider (LCH) at CERN is of the order of 10^{14} eV, which is a million times lower than the highest CR energies observed.

The MC simulations of EAS used at the Pierre Auger Observatory, presented in Sec. 4.2, rely on the CORSIKA [85] code package, standing for COsmic Ray SImulations for KAscade. Because of the very large number of particles present in EAS at UHE, more than 10^{11} for a 10^{20} eV proton, the tracking of each individual particle would be overwhelming in terms of computing time. To overcome this problem, a thinning method is used, in which a sub-sample of particles is tracked instead. A weight is given to each particle of the sub-sample to account for the unrepresented particles. This method can generate artificial fluctuations because of large weights given to one of the sub-samples, thus requiring some unthinning method to simulated the detector response reliably [86]. The Pierre Auger Collaboration uses the Offline software [87] to simulate the detectors

responses and analyse data. It is also within this framework that simulated showers and real showers are reconstructed (see Sec. 4.2).

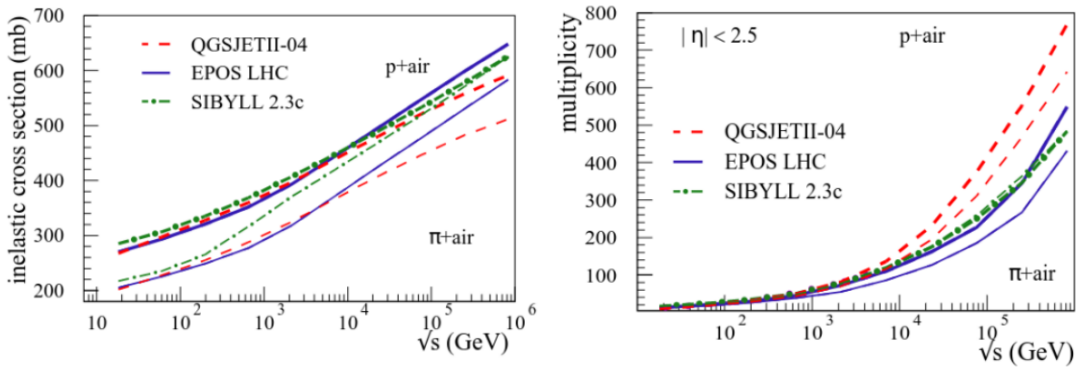

Figure 4.3: Left: inelastic cross sections of proton-air and pion-air interactions as function of the energy for three hadronic interaction models (EPOS LHC, QGSJet, Sibyll). Right: multiplicity of proton-air and pion-air interactions as function of the energy. Taken from [88].

In the CORSIKA framework, the electromagnetic shower component is simulated with ESG4 [89] that takes into account phenomena like the LPM effect occurring at UHE (see Sec. 4.3.1). Different models are used to simulated hadronic interactions at lower energies like FLUKA [90] or UrQMD [91]. At the highest energies, mainly three models are used: Sibyll [62] [92], QGSJet [63] and EPOS-LHC [61]. Because measurements from accelerators do not exist at the highest energies, the phenomenological models of hadronic interactions are used to extrapolate the data, leading to important uncertainties on these extrapolations which increase as the energy grows. The different models treat hadronic interactions in different ways leading to differences in the multiplicities and cross sections, among other parameters. This is shown in Fig. 4.3 [88] in which the inelastic cross sections (left) and the multiplicity (right) of proton-air and pion-air interactions are plotted as function of the energy for three hadronic interaction models. This leads for instance to differences in the values predicted for the maximum depth of development as well as the number of muons (Fig. 4.4 [93]), for different models (EPOS, Sibyll and QGSJet) and primaries (photons, protons and iron).

Above 10^{16} eV, and increasing with energy, a muon deficit in Monte-Carlo simulations of EAS with respect to data has been observed by several experiments. It was first reported in [94] by the collaboration HiRes/MIA and was then also highlighted by other experiments: NEVOD-DECOR [95] [96], SUGAR [97], Auger [98], Telescope Array [99]. However, the KASCADE-Grande [100] and EAS-MSU [101] collaborations found no muon deficit with respect to data. While X_{max} is mainly linked to the electromagnetic part of the shower, the muon number is related to the hadronic component and is therefore more impacted by the extrapolations mentioned previously. Thus, the interpretation of the measurements based on the simulations could be affected by the deficit in muon production by the hadronic models, in particular it could lead to infer an heavier composition of the flux than it actually is. In this thesis, simulations of photon-induced showers are used (see Sec. 5.3). Like all simulations they are impacted to some extent by the muon deficit.

The number of muons in photon-shower being less important than in nucleus-induced showers as explained in more details in Sec. 4.3, these simulations are less impacted by the choice of the hadronic interaction model. This can be observed in Fig. 4.4, the number of muons does not variate as much for photons than for nuclei primaries.

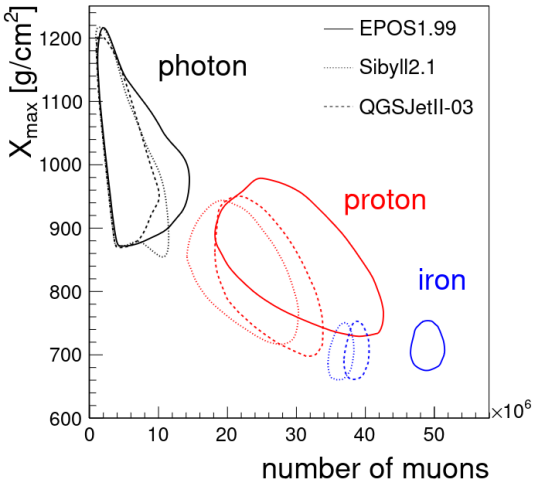

Figure 4.4: The depth of maximum development as function of the muon number in simulated showers of photon (black), protons (red) and iron (blue) primaries for different hadronic interaction models. The contours include 90% of the distributions. Taken from [93].

4.2 The Pierre Auger Observatory

The measurement of EAS generated by the UHECR can be performed by detecting the particles at ground with an array of detectors, or by measuring the fluorescence light emitted by nitrogen molecules during the passage of the particles in the atmosphere. Above 10^{17} eV, the showers are deep enough in the atmosphere for the secondary particles to reach the ground at high enough altitudes. The discrepancy in the UHECR spectrum between AGASA and HiRes (Sec. 2.1.1) as well as the too few measurements at the highest energies led to the construction of larger ground arrays to detect EAS. In 1991, Cronin and Watson decided to form a collaboration to build a large array of a few thousands km^2. After the choice of Water Cherenkov detectors for the ground detector, it was decided to add fluorescence telescopes to overlook the ground array making the project an hybrid observatory. The chosen site was in the pampa Amarilla, close to the town of Malargüe. This flat land is at 1400 m a.s.l., equivalent to a vertical atmospheric depth of 880 g/cm^2. The region offers good atmospheric conditions and is surrounded by small hills convenient to install the FD telescopes. The construction began in 2002 and lasted until 2008. The observatory started taking data in 2004. Today the collaboration is composed of 18 countries from all over the globe.

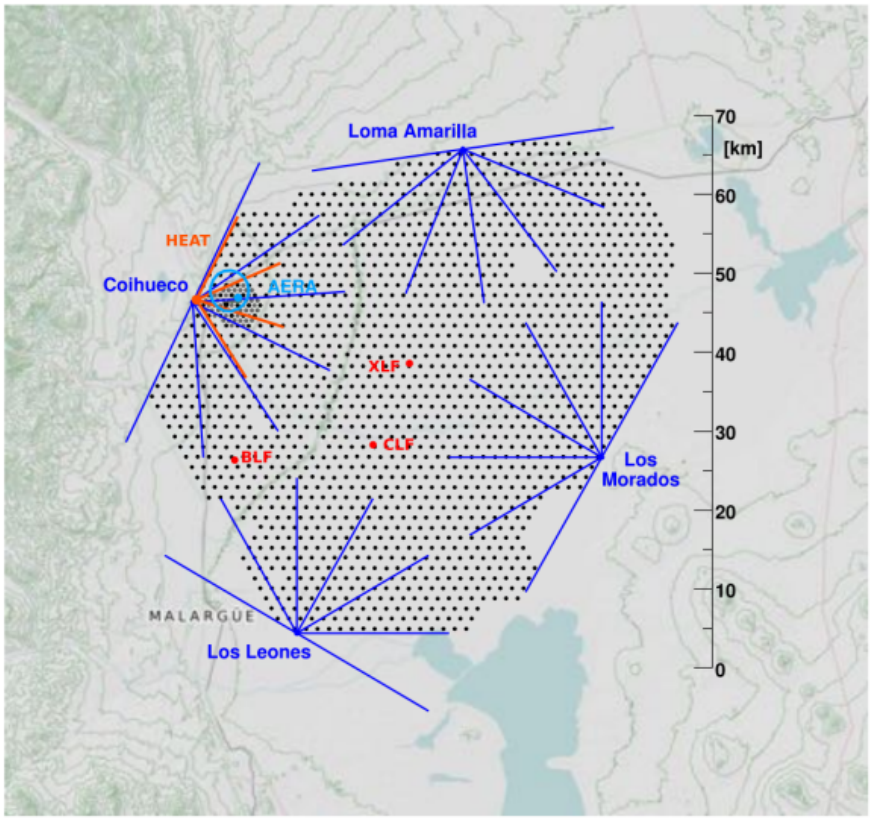

Figure 4.5: Map of the Pierre Auger Observatory, Malargüe, Argentina. The black points represent the WCD which compose the Surface Detector. The field of view of the FD (HEAT) are delimited by the blue (red) lines. From [102]. The laser facilities CLF and XLF are indicated by red dots along with the BLF.

The surface detector (SD) of the Pierre Auger Observatory consists in a triangular network of 1600 water Cherenkov detectors, referred to as stations hereafter, spread over 3000 km^2 and separated by 1500 meters from one another. This array, called the SD-1500, detects showers efficiently above 10^{18} eV and was completed by another array of 60 stations covering about 28 km^2 with a smaller spacing of 750 meters between stations aiming to detect showers with a smaller energy threshold ($\sim 10^{17}$ eV). The SD-750 itself was also completed by 12 additional stations to create an array with spaces of 433 m which aims to detect lower energy showers at $\sim 10^{16}$ eV. These arrays are shown in Fig. 4.5. The surface detector provides a duty cycle of almost 100% and measures the lateral profile of the shower from which an estimation of the primary energy is done. The arrival direction of the cosmic ray can be retrieved thanks to temporal information coming from the detectors hit by the secondary particles.

The fluorescence detector (FD) is composed of 27 fluorescence telescopes, 24 of them are divided in four groups located around the SD : Loma Amarilla, Los Morados, Los Leones and Coihueco. Each of the telescopes have a field of view of 30° in azimuth and 30° in elevation (from 0° to 30°). The azimuthal field of view of the different units are depicted by the blue lines in Fig. 4.5. Three additional telescopes are deployed at the Coihueco site for the detection of lower energy events ($\sim 10^{17}$ eV). They are reported by

the red lines on the map and referred to as High Elevation Auger Telescopes (HEAT). The FD gives access to the longitudinal profile of the shower by collecting the fluorescence UV light emitted by the interactions of the showers particles with atmospheric nitrogen molecules. The cosmic ray energy can then be measured calorimetrically and with a better resolution than with the SD. The telescopes can only work during moonless nights, when the intensity of background light is lower, and with good atmospheric conditions, to ensure a good reconstruction. This results in a duty cycle of about 14%, significantly smaller than the SD. In the following, the focus will be given to the SD which is the detector used in the analysis developed in this thesis work but a description of the FD is given in Sec. 4.2.3.

Other facilities are present at the Observatory's site (see Fig. 4.5). Two high powered laser facilities are installed in the array: the Central Laser Facility (CLF) and the eXtrem Laser Facility (XLF). They are used for atmospheric measurements. The Auger Engineering Radio Array (AERA) is devoted to the radio detection of the air shower.

4.2.1 The surface detector

The detector

A water Cherenkov detector (WCD) is shown in Fig. 4.6 (left). It consists in a 3.6m diameter plastic tank made of polyethylene, filled with 12 tons of ultra-pure water. A sealed liner with a reflective inner surface is installed inside the plastic tank. Three photo-multipliers tubes (PMTs), directed downwards, are located at the top to collect the Cherenkov light emitted by the passage of the particles in the water. They are at 1.20m from the centre of the tank and are equally spaced from one another (Fig. 4.6, right). The detector is autonomous thanks to the solar panels fixed on its top and the batteries. The communication between the WCD and the central data acquisition system (CDAS) is done through the radio antenna to transmit the data collected and a GPS device provides an accurate time information.

The Cherenkov light pulses collected by the PMTs are emitted by the relativistic particles travelling through the water volume. The depth of the water in the tank makes it sensitive to high energy photons converting to electron-positron pairs. The reflective liner intensifies the amount of light reaching the PMTs which convert the light into electric signals collected by the electronics set inside a dome on top. The signals are digitised by 10-bit flash-analog-to-digital converters (FADCs) every 25ns. Each PMT has two outputs: an anode (low gain) and a dynode (high gain) providing a signal of 32 times the charge gain in the anode. These two outputs allow a large enough dynamic range to provide a good precision either close or far from the shower core. Saturation can occur when the signal is over 650 times the peak current from a vertical muon traversing the WCD. It corresponds to the signal at 500 m for a 100 EeV shower. As an example, the signals recorded by each PMT after calibration (see below) is shown in Fig. 4.7.

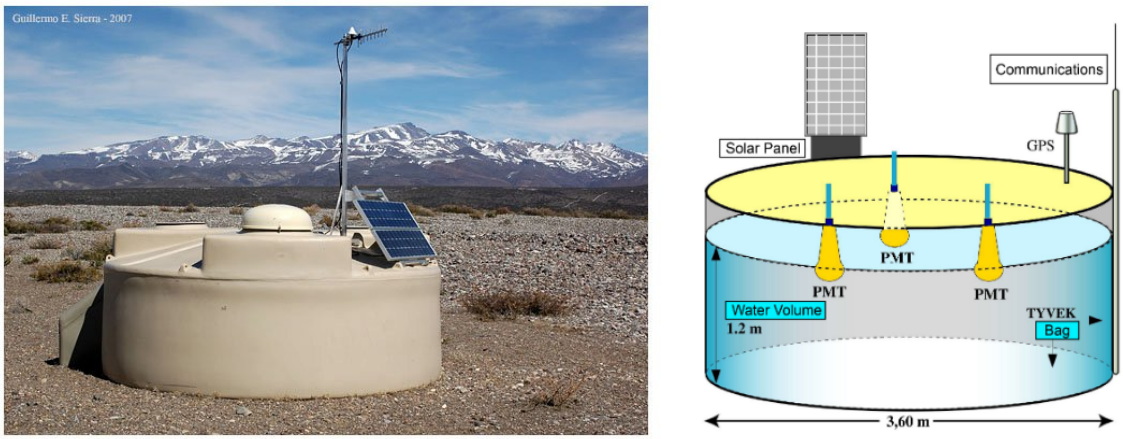

Figure 4.6: Left: photo of one of the 1660 water Cherenkov detectors (WCD) at the Pierre Auger Observatory. Right: Scheme of the WCD with legends referring to the main elements.

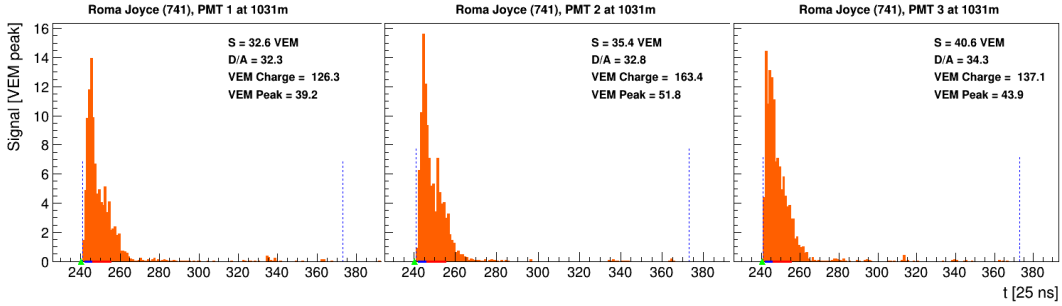

Figure 4.7: The signals recorded by the three PMTs in bins of 25 ns for a station at ~ 1000 m from the shower axis.

Prior to the calibration of PMT signals, the baseline of the low gain and high gain traces of each PMT and the range of signal (start and stop time) are determined. The latter is determined from the high-gain channel only because of its higher resolution. After the subtraction of the baseline in each PMT traces are calibrated.

The calibration of the signal recorded by a station is performed locally by the electronics. It is done using an unit called Vertical Equivalent Muon (VEM), corresponding to the signal produced by a muon going through the water vertically [103]. The 1 VEM value is measured by identifying the peak produced by omni-directional muons in the charge histograms, which is correlated with the VEM charge. By applying the appropriate conversion factor which has been measured using one WCD instrumented with a muon hodoscope, the actual VEM value is obtained.

The total signal of a station is obtained by integrating the final trace, which consists of the bin-average of the high gain or low gain (if the high-gain is saturated) traces of the working PMTs, between the start and stop times.

The stations have two local threshold triggers called T1 and T2 requiring a certain signal intensity in one bin, or in several bins within a specific time window. The next

trigger level, T3, is a global one. It is generated if the T2-triggered stations verify spacial and timing criteria. The reader can find more information on the triggers deployed at the Observatory in [104].

4.2.2 Reconstruction with the SD

In this section, the reconstruction of events with zenith angles below 60° using the surface detector are considered. The reconstruction for inclined showers (zenith angles above 60°) is different and will not be discussed [105], since the photon search with the SD [32] is done only with the "vertical" data set of events.

When a T3 is identified, it is sent to the CDAS. There, a physic trigger called T4 is applied to select an event as a shower candidate from the T3 data. It requires a coincidence between neighbouring stations and the propagation time of the shower front. Among the stations of the selected event, some can be flagged as accidental when their trigger timing is not compatible with the estimated shower front. This timing cut was designed so that 99% of the stations with physical signal are kept. A fifth level of triggers is based on the number of active stations surrounding the WCD with the higest signal. The 6T5 thus requires a number of 6 such stations, and is used in particular to select events for the spectrum reconstruction. This ensures a good detection and reconstruction accuracy, by avoiding for instance the showers falling at the borders of the array in which information would be missing. The trigger efficiency for nuclei-induced showers below 60° and energies above 2.5 EeV is 100% [19].

The reconstruction procedure consists of three main steps. First, the geometry of the shower, namely the core position at ground and the arrival direction, is determined using the timing information of the stations as well as their signal sizes. Then, looking at the signal sizes as function of the distance to the shower axis, the lateral distribution function (LDF) is fitted to an empirical-derived function. The energy of the primary cosmic ray can be determined using an estimator based of this LDF.

Shower geometry

The geometry of the event is reconstructed by fitting the start times of the signals, weighted by their individual signal sizes (integrated signal over time), to a plane shower front. For cases with more than four triggered stations, the plane shower front is replaced by a more detailed and realistic spherical model with a speed of light inflating sphere. Both cases of shower front are illustrated in Fig. 4.8, left and right respectively. The determination of the geometry is done using a χ^2-minimisation of three parameters: two parameters representing the arrival direction and the time at which the core reaches the ground (t_b on Fig. 4.8). In case of the spherical model, an additional parameter, the radius of curvature R_c, is reconstructed.

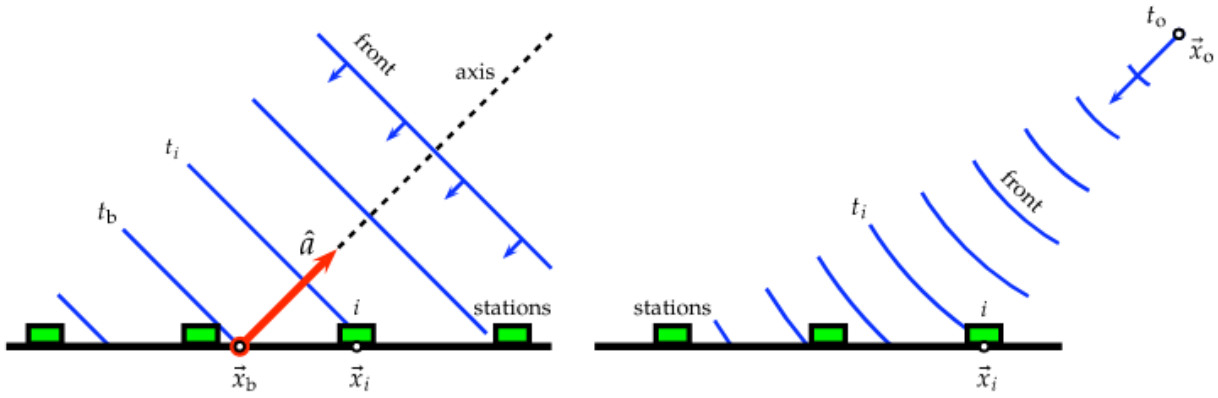

Figure 4.8: Left: Illustration of a plane front approximation for air shower development. Right: Scheme of the spherical shower front development. Figure is taken from [106].

Lateral distribution function

The geometry of the shower being reconstructed, it is possible to visualise the signal sizes of triggered stations as function of the perpendicular distance to the shower axis r. From this, the stations signals are fitted with a scaled average function, a modified Nishimura-Kamata-Greisen (NKG) function 4.10 [107] [108], given by:

$$f_{LDF}(r) = S(r_{opt})(\frac{r}{r_{opt}})^{\beta}(\frac{r+r_1}{r_{opt}+r_1})^{\beta+\gamma} \tag{4.10}$$

which describes the lateral distribution of the signal S at ground. An example of an LDF fit is shown as the blue plain line on the right panel of Fig. 4.9. The left panel shows the footprint left by the event on the SD-1500 array.

In Eq. 4.10, β and γ are the parameters governing the logarithmic slope of the LDF describing the fall of the signal with increasing distance from the core, $r_1 = 700$ m and the optimal distance r_{opt} is the distance at which the shower to shower fluctuations in the expected signal $S(r)$ are minimised. This distance depends on the detector geometry, and in the case of the SD-1500 is equal to 1000 m, as shown in [109]. The fluctuations in the expected signal for identical primary parameters (energy, arrival direction and mass), are mainly linked to the characteristics of the first interaction, such as its position and multiplicity. The value of $S(r_{opt})$, referred to as S_{1000} here after, is called the shower size and is shown as the bright red point on the LDF in Fig. 4.9. It is the parameter from which the energy is estimated.

The fit of the LDF is based on a maximum likelihood method which takes also into account the probabilities associated to the non-triggering and saturated stations. In most cases the signal can be recovered as described in [110]. For events with only three stations, the shape parameters β and γ are obtained through a parametrisation depending on S_{1000} and the zenith angle θ.

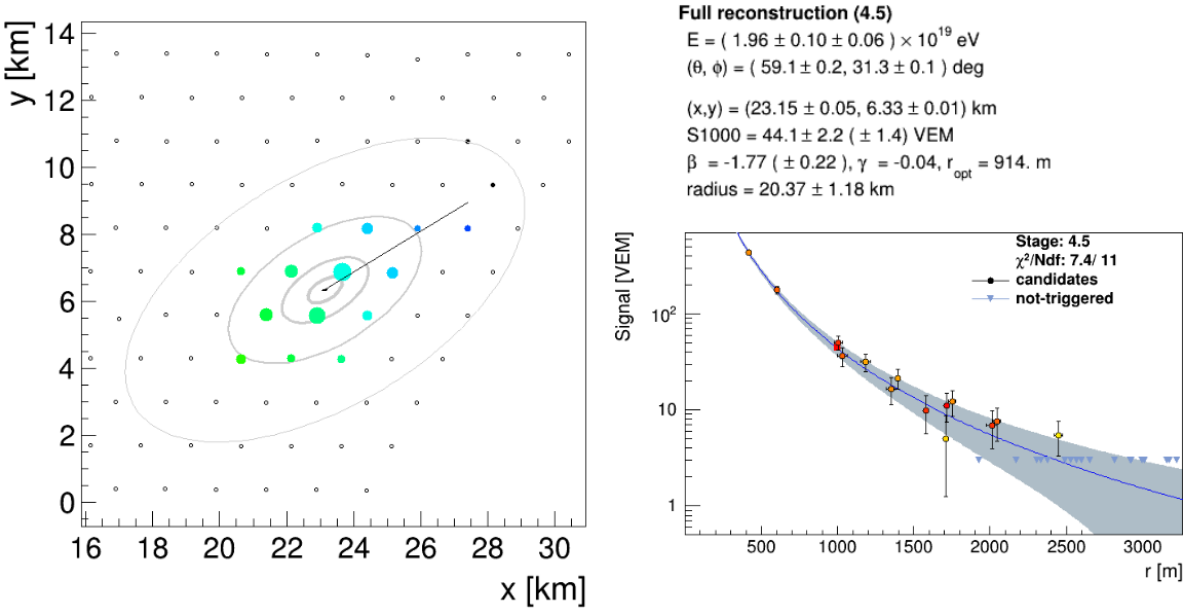

Figure 4.9: Left: example of a shower footprint on the SD-1500. The colour scheme give the temporal information and the size of the circle the signal size. The projection of reconstructed axis is reported by the black line. Right: The corresponding LDF fit of the event (blue line) and the different triggered stations (time-integrated signal as function of the perpendicular distance to the core). Stations used in the fit are represented by filled circles, non-triggered stations by blue triangles and removed stations by empty circles. The event reconstructed parameters are written at the top.

The uncertainty in the reconstruction of the shower size S_{1000} has three main contributions: the sampling fluctuations of the signal, the assumptions in the shape of the LDF, and statistical fluctuations in the shower development. The first one contributes to a factor of about 10%, while the contribution from the two others depends on the energy and varies from about 20% to 6% for lowest to highest energies.

Primary energy

As stated previously, the energy is estimated from S_{1000}. The shower size depends on the energy as well as the zenith angle θ. Considering an identical energy, S_{1000} is attenuated with increasing θ because of the larger depth of atmosphere the shower has to cross to reach the detectors. Thus, to estimate the energy, the attenuation of the shower as function of the zenith angle must be corrected. The shape of the attenuation curve $f_{CIC}(\theta)$ is obtained from data using the CIC method [111] (Constant Intensity Cut) and is shown in Fig. 4.10 [106] assuming an isotropic flux of cosmic rays at the top of the atmosphere.

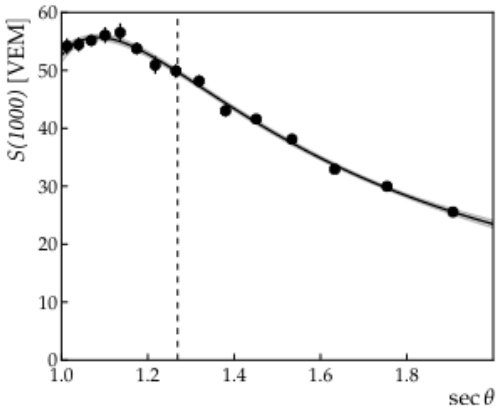

Figure 4.10: Attenuation curve of the shower size S_{1000} as function of sec(θ). The median of 38° is reported by the dashed vertical line. Taken from [106].

The median angle $\theta = 38°$ is chosen as reference and is reported by the dashed line of Fig. 4.10. We convert S_{1000} to $S_{38} = S_{1000}/f_{CIC}(\theta)$, that is the value of S_{1000} if the zenith angle of the shower was of 38°.

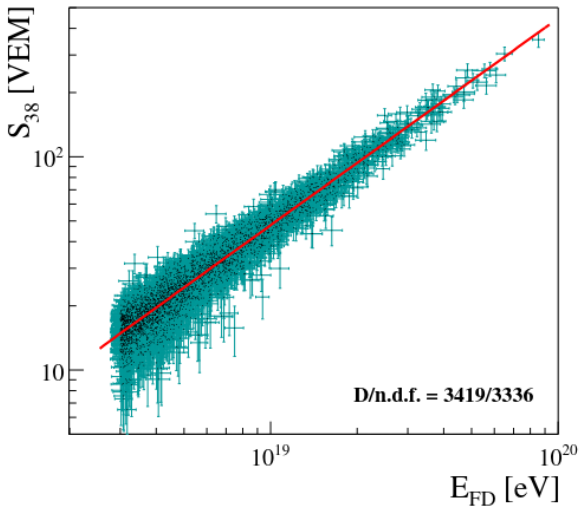

Figure 4.11: The relation between the energy measured with the FD E_{FD} and SD energy estimator S_{38}. Taken from [112].

The SD energy estimator corrected for its zenith dependence is calibrated with a high quality sample of hybrid events, reconstructed both by the SD and the FD. The events selected in this sub-sample pass strict quality and field of view conditions: accurate fit of the longitudinal profile of the shower with an X_{max} resolution better that 40 g/cm^2, FD energy resolution smaller than 18%, and good atmospheric conditions. The simple relation between S_{38} and the FD energy E_{FD} measured calorimetrically is described by a power law function (Fig. 4.11):

$$E_{FD} = A(S_{38})^B \tag{4.11}$$

The systematic uncertainties of E_{FD} increases with the energy and range from 7% at 10 EeV to about 15% at 100 EeV. The SD energy resolution is inferred from the E_{SD}/E_{FD} distribution and is of about 16% at the lowest energy threshold and decreases to 12% for energies over 10 EeV.

4.2.3 The fluorescence telescope

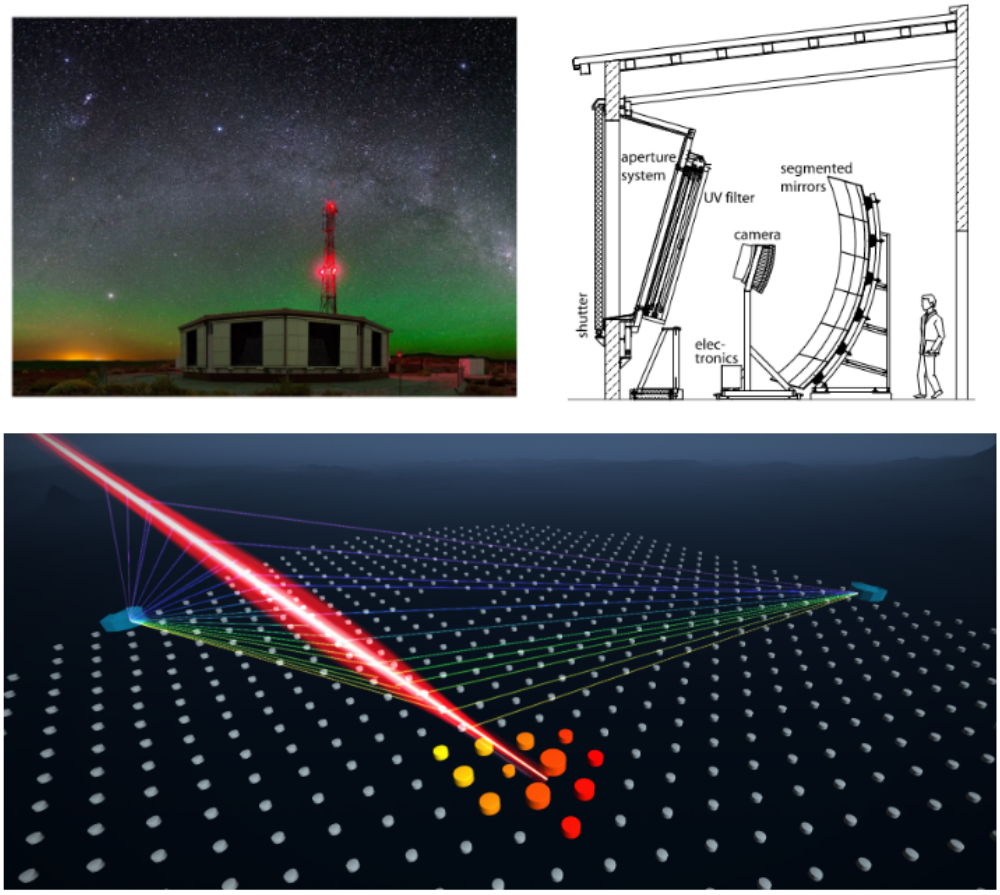

Figure 4.12: Top left: Picture of one of the four FD sites building. Top right: Illustration of a fluorescence telescope featuring the main elements. Taken from [113]. Bottom: Modelisation of an hybrid event detected at the Observatory. The stations colours are linked to the arrival time of particles (yellow for detectors hit first by the particles). Their sizes increase with the signal intensity. The colours of lines joining the shower to the telescopes are representative of the arrival time of the light to the FD. Taken from the Pierre Auger Collaboration website

The telescopes composing the FD measure the UV fluorescence light emitted following the desexcitation of nitrogen molecules of the atmosphere, excited by the charged particles of the showers. Distributed in four sites around the surface detector, they track the longitudinal development of the shower by measuring the intensity of the fluorescence light. The detectors also catch the Cherenkov light emitted by the shower particles. Each of the site with six telescopes gathered in a clean building, provides a 180° coverage

in azimuth. A picture of one of the sites building is visible in the top left panel of Fig. 4.12.

The light enters the telescope building through a diaphragm with a 1.1m radius. This diaphragm is covered by a glass window filter aiming to reduces the background light and improve the signal to noise ratio. The light is then focused by a segmented mirror with a radius of curvature of 3.4 radius on a focal plane equipped by a camera with 440 hexagonal PMTs (pixels) and the recorded signal is shaped and digitised by the electronics unit. The electronics also generate threshold and geometry triggers. All elements are illustrated on the top right panel of Fig. 4.12.

To be operational, the FD needs optimal atmospheric night conditions. Thus, the atmosphere is monitored every night by thousands of collimated UV laser pulses. The calibration of the FD is also done through laser shots. More information about the monitoring and the calibration can be found in [113].

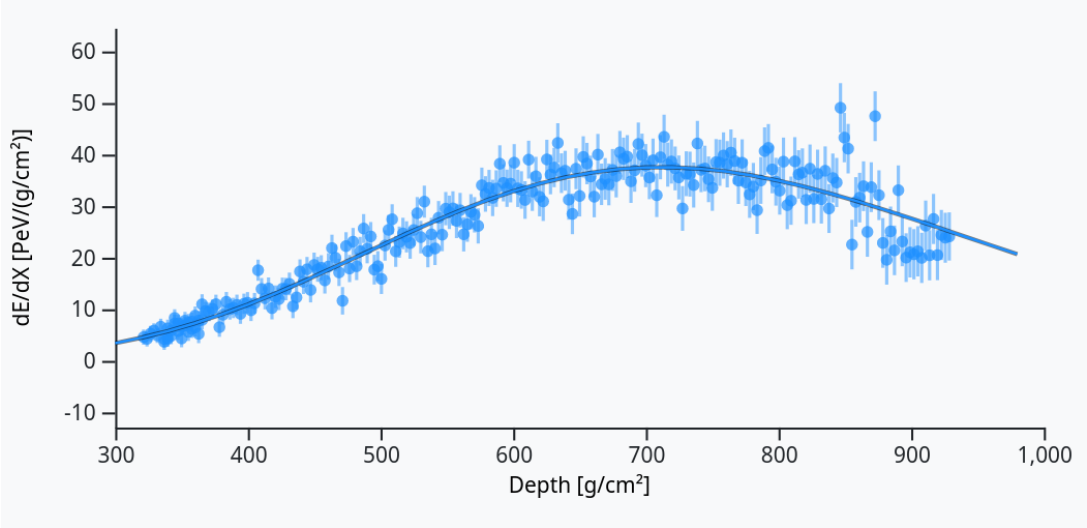

Figure 4.13: Example of the measurement of a longitudinal profile with the Gaisser Hillas function fit. Taken from the Pierre Auger Collaboration websitesource.

As previously stated, the telescopes gives access to the measurement of the longitudinal profile of the shower. The intensity of the light collected is proportional to the energy deposited by the shower particles. An example of the energy deposit as function of the slant depth is shown in Fig. 4.13. After being measured, the profile is fitted by a Gaisser-Hillas function and X_{max} is obtained directly. The integral of the fitted function gives the calorimetric energy of the shower. Since an invisible part of the energy is carried by neutrinos and high energy muons which do not interact in the atmosphere, a data-driven parameterisation of this invisible energy as function of the calorimetric energy was developed and used to correct the energy assignment [114]. At the bottom of Fig. 4.12, an event detected simultaneously by the SD and FD is shown.

4.3 Identification of UHE photons

The development of a shower depends on the nature of the cosmic ray and is therefore different for a photon-induced showers and hadron-induced ones. The search for UHE photons at the Pierre Auger Observatory exploits the specificities of photon showers. In this section, these properties are discussed along with their consequences on the shower development. Two ultra high energy phenomena occurring for photons are also presented. Finally, the observables based on the differences between photon and hadron showers and used in the current SD photon search analyses are addressed.

4.3.1 Particularities of photon-induced air showers

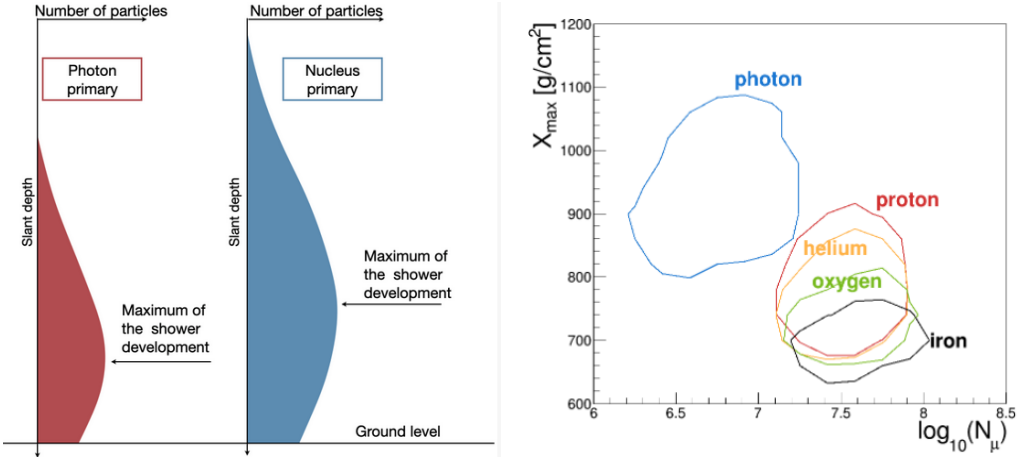

Figure 4.14: Left: Schematic view of the difference in the longitudinal development for nucleus-induced shower (blue) and photon-induced shower (red). The depth corresponding to the maximum of the shower development, X_{max}, is identified by the arrows (from [115]). Right: Distributions of X_{max} as function of the logarithm of the number of muons from shower simulated with different primary types and energies ranging from $10^{18.5}$ eV to 10^{19} eV. The contours include the 90% of each distribution (from [116]).

For a same primary energy and zenith angle, photon-induced air showers develop deeper in the atmosphere than nucleus-induced showers. This is due to the smaller multiplicity of electromagnetic interactions with respect to hadronic ones: more interactions are required for the primary energy to decrease down to the critical energy at which the process of cascade stops. Moreover, this characteristic of photon showers is even more stressed at higher energies because of the Landau-Pomeranchuk-Migdal effect (LPM effect), explained later, which results in the reduction or suppression of pair production and Bremsstrahlung cross sections. This belated development of photon-induced showers in the atmosphere means that on average, the X_{max} measured for photons will be greater than the X_{max} of nucleus-induced showers (see left panel of Fig. 4.14 for a photon and proton primary). Above 10^{18} eV, the average difference is of 200 g.cm^{-2}. On the other hand, the preshower effect, occurring at ultra-high energies, can decrease the value of X_{max} for photons as the photon has a probability of converting to an e^+/e^- pair in the

Earth's magnetic field above the atmosphere as described hereafter.

The photon-induced showers also differ from hadron-induced ones because of their smaller muon content as a result of the properties of hadronic and electromagnetic interactions. The mean free paths for photo-nuclear interactions and pair production of muons/antimuons, from which originate hadrons and secondary muons, are two orders of magnitude above the radiation length. Thus, only a rather small fraction of muons are created along the development of a photon shower, and the most part of the primary energy is transferred into the electromagnetic component.

Preshowering effect

For energies above $10^{19.5}$ eV, UHE photons can convert into an electron/positron pair well above the atmosphere (at thousands kilometres above ground) when interacting in the Earth's magnetic field [117]. This process in called preshowering and leads to a different development for these specific photon-showers [118]. The probability of conversion increases along with the photon energy and the strength of the transverse component of the magnetic field $B_{\perp}$. The pair produced emits synchrotron photons which in turn can convert if their energy is sufficient enough, resulting in a collection of sub-showers initiated by photons, electrons or positrons with a smaller energy. Consequently, the X_{max} of preshowering photons is smaller than the one expected without the magnetic pair conversion. Fig. 4.15 shows the mean X_{max} as function of the energy for photon, proton and iron simulations. The whole of photon simulations are reported as the black stars. The non-preshowering photons are shown as red stars while preshowering photons are marked in blue (with preshower effect evaluated for the Pierre Auger Observatory site).

Landau-Pomeranchuk-Migdal

Another phenomenon called the Landau-Pomeranchuk-Migdal effect [119] (or LPM effect) affects high energy photons and modify the expected development of the shower. It consists in the reduction or suppression of the cross sections for Bremsstrahlung and pair production, and happens when a relativistic particle undergoes several scattering. If the particle wavelength is longer than the distance between scatterings, the successive scatterings cannot be treated as independent. This leads to destructive interferences, reducing the number of radiations expected, and leading to the reduction of the cross sections. Thus, the development of the shower is delayed and the corresponding X_{max} is significantly larger as reported on Fig. 4.15. To highlight the combined effect of LPM and preshower, the grey stars show the average value of X_{max} when both effects are ignored.

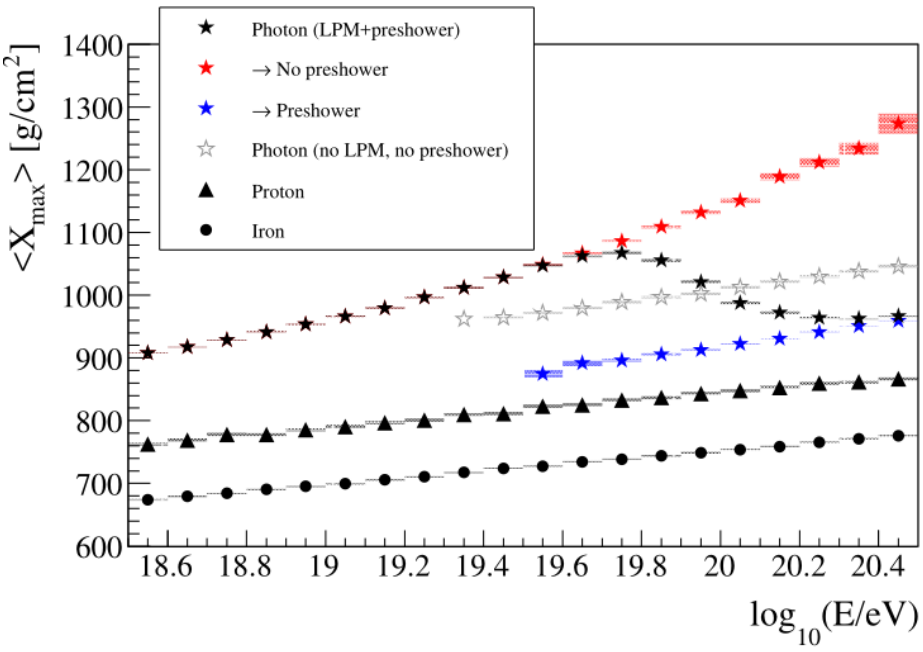

Figure 4.15: Mean X_{max} of simulated showers for photon (stars), proton (triangles) and iron (circles) primaries as function of the Monte-carlo energy. The whole of the photon simulations, with LPM and preshower effects, is shown by the black stars. The non-preshowering photons are reported in red, while the preshowering ones are in blue. Finally, the non-preshowering photons which are not affected by the LPM effect are reported in white. Taken from [120].

4.3.2 Consequences on the shower development

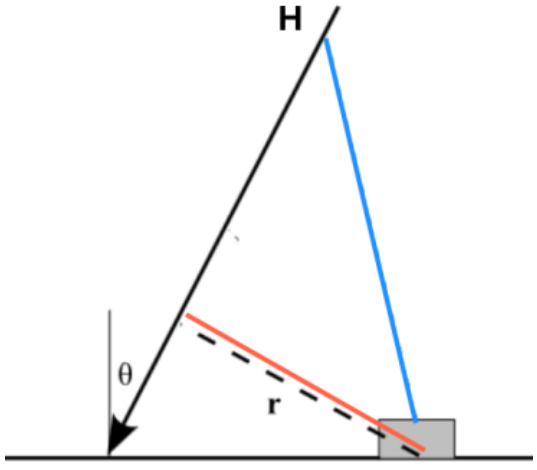

Figure 4.16: Illustration of the delay in the arrival time of particles depending on the production height H and the perpendicular distance between the station and the axis r. Taken from [121] and modified.

In the right panel of Fig. 4.14 are reported the distributions of X_{max} as function of the number of muons for different primaries simulations. It clearly appears that these two parameters allow a good discrimination between nuclei and photon primaries. They firstly result in a difference in the observed lateral profiles of the showers (LDF): the electromagnetic component produce a steeper lateral profile than the muonic component because hadrons tend to acquire a larger transverse momentum and thus travel further away from the shower core. This effect is amplified by the later development of photon showers because the lateral development of the shower grows along with the multiple interactions during its development. Therefore, on average the LDF of photon showers is steeper than for hadrons, and at ground, the footprint left by the shower is consequently smaller, in the hypothesis of identical energy and zenith angle of the primary particle.

Another consequence of the smaller muon content and larger X_{max} is observed in the delay of the arrival times of particles at ground for the same distance r to the shower axis. For geometrical reasons [121], particles produced at higher altitudes arrive earlier than those produced closer to ground, for the same distance r. If one considers a particle created at altitude H, the delay time for it to arrive to a station at distance r (blue in Fig. 4.16) with respect to the shorter path length (orange) is:

$$t(H) = \frac{1}{c}\sqrt{H^2 + r^2} - \frac{H}{c} \tag{4.12}$$

and can be approximated for $r \ll H$ as:

$$t(H) = \frac{H}{c}(\sqrt{1 + \frac{r^2}{H^2}} - 1) \propto \frac{r^2}{H} \tag{4.13}$$

The delay increases with r but more importantly, decreases with altitude H. Therefore, showers developing later in the atmosphere have a bigger delay t in the arrival time of particles for the same distance r, which is the case for photons. Moreover, this effect is amplified by the smaller muon content of photon showers as muons undergo significantly less scattering than electrons or positrons. Thus, the muonic component being more important in nucleus-induced showers, the delay in the arrival time of particles at ground is smaller than photon-induced showers.

4.4 Search for UHE photons at the Pierre Auger Observatory

The search for UHE photons inside the Pierre Auger Collaboration is performed using discriminating variables based on the differences between photon and hadron induced showers. Depending on the energy range considered and the available data sets, different analyses have been developed.

The maximum depth X_{max} measured by the FD is a very robust observable for the photon search. However, as stated previously, the fluorescence telescopes have a duty cycle of about $\simeq 14\%$, working only during moonless nights with appropriate atmospheric conditions. The exposure of the hybrid is therefore too low above $10^{19.5}$ eV and the search

for UHE photons cannot be performed at the highest energies due to the low event rate. Thus, the hybrid search for UHE photons begins at a lower energy threshold ($\simeq 10^{18}$ eV) than the SD ($\simeq 10^{19}$ eV). The hybrid search published in [71] is designed using the universality model from which the muon content of the shower is obtained.

For lower energies, below 10^{18} eV, the low energy extensions of the Observatory are used, namely the denser region of the array, the SD-750, and the HEAT telescopes [122]. In both hybrid searches, the analyses are first performed on proton simulations to evaluate their performances. Proton showers are chosen among other primaries because their X_{max} is higher and muon content smaller than that of heavier nuclei, making their characteristics closer to the photon shower ones (see Sec. 4.1.2). As no photon have been identified in these analyses, limits on the integrated UHE photon flux were derived by taking into account the exposure of the data set and the selection efficiency. In the following, the different searches and their corresponding analysis are presented, with an emphasis on the SD search.

4.4.1 Hybrid searches of UHE photons

The photon search above 10^{18} eV is performed with the hybrid data of the Observatory [71]. The X_{max} measured by the fluorescence telescopes is used to identify photons, combined with a variable related to the muon content of the shower, referred to as F_μ in [71]. The muon content is a parameter of the universality model (Sec. 5) which predicts the individual signals in stations. Thus, F_μ can be obtained by matching the predicted signal from universality with the observed signal in a station. If the event has more than one station, F_μ is set to the average.

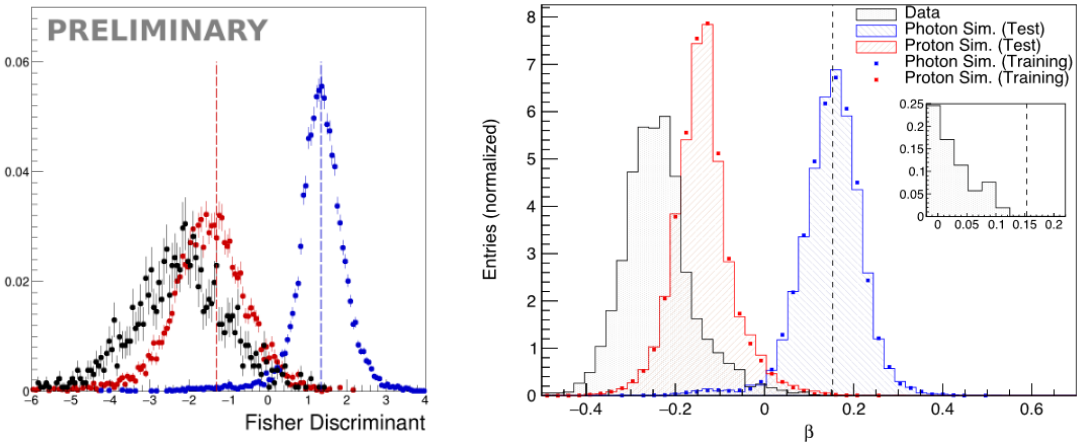

Figure 4.17: Left: Normalised distributions of proton simulations (red), photon simulations (blue) and the burn sample of data (black) on the Fisher axis. The vertical dashed blue line represents the selection cut of photon candidates. The red dashed line correspond to the starting point for the fit of the proton tail. Taken from [71]. Right: Normalised distributions of the BDT output for proton simulations (red), photon simulations (blue) and data (black). The vertical line is the median of photon, indicating the photon candidate selection cut. Taken from [122].

X_{max} and F_μ are then combined in a Fisher discriminant analysis (see Sec. 7.2.2), along with the energy and zenith angle. The distributions of protons (red), photons (blue) and the burn sample of data (or "test sample" in black) are reported on the left panel in Fig. 4.17. The candidate selection cut is chosen as the median of the non-preshower photons distribution on the Fisher axis (dashed blue line). This cut is a good compromise to obtain a reasonable balance between efficiency and purity, and is shown to be stable. Although nuclei primaries are very well separated from the photons, a few events are found to be above the selection cut. Therefore, it is necessary to estimate the expected background. As the number of events in the burn sample is low (5% of data before any selection), the functional form of the burn sample tail is derived from the tail of proton simulations (starting from the red dashed line in the left panel of Fig. 4.17). Eventually, 30 ± 15 background events selected as photon candidates are expected.

The designed analysis is then applied to the search sample consisting of all hybrid data except the test sample. Twenty-two candidates are found which is in agreement with the amount of expected background. Thus, upper limits are calculated and the results are reported in blue on Fig. 4.21.

In a previous analysis published in 2017 [123], a search analysing hybrid events was performed using three observables. Alongside the X_{max} measured by the fluorescence telescopes, two additional variables obtained with the SD-1500 array were used: S_b and $N_{stations}$. The first one is related to the lateral distribution function and is defined as:

$$S_b = \sum_{i=1}^{N_{stations}} S_i \times (\frac{R_i}{1000 \text{ m}})^b \tag{4.14}$$

where S_i is the signal in the SD station i an R_i is the corresponding perpendicular distance to the shower axis. The b parameter is set to 4 as it is the value optimising the photon-hadron discrimination. The second observable $N_{stations}$, also appearing in the definition of S_b, is the number of triggered SD stations. These three observables are combined in a boosted decision tree (BDT). In addition, and to account for the dependencies on the energy and zenith angle, the energy and zenith angle are added in the multivariate analysis (MVA). The MVA is trained on photon and proton shower simulations before being applied to data. The number of candidates is compatible with the background expectations and upper limits were derived. They are reported in dark blue on Fig. 4.18. In comparison the limits obtained with the universality based analysis are in red and the improvement obtained with the use of universality and the more important data set is visible.

The previous hybrid analysis [123] was extended to lower energies , down to 2×10^{17} eV, using the low energy extension deployed at the Observatory: the SD-750 array and the HEAT fluorescence telescopes at the Coihueco site [122]. The normalised distributions for photon (blue), protons (red) and data (black) on the axis found by the BDT is shown in Fig. 4.17. The candidate selection cut is the median of photons, represented by the vertical dashed line on the figure. Zero photon candidate was found above the median and the resulting limits on the photon flux above 2×10^{17} eV are reported in red on Fig. 4.21.

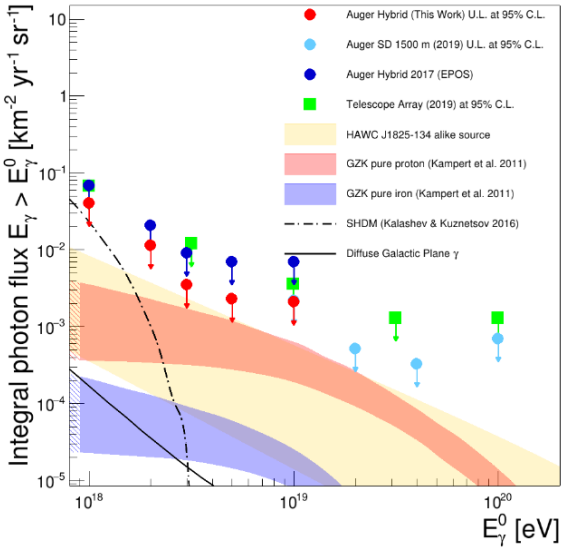

Figure 4.18: Upper limits on the integrated photon flux above 10^{18} eV. The limits derived from the current hybrid search [71] are reported in dark blue and the previous one in red [123]. Limits derived from the SD search are reported in light blue, and the one from Telescope Array in green [124]. Figure taken from [125].

4.4.2 SD-1500: Photon search above 10^{19} eV

At the highest energies, above 10^{19} eV, the search for UHE photons is performed with only the SD due to the limited duty cycle of the FD. From that, several issues arise: the X_{max} cannot be measured, the extraction of the shower muon content from the WCD signals is difficult and not straightforward, the energy is only accessible indirectly from the shower size (see Sec. 4.2.2) and the case of preshowering photons has to be considered.

The search for UHE photons with the SD-1500 published in [32] is performed using two discriminating variables describing respectively the steepness of the LDF and the spread in time of the signals in the WCD, with respect to the bulk of data. This way, potential UHE photon candidates should deviate from the average of data, having signals more spread in time and a steeper LDF.

The spread in time of WCD signals can be estimated in each tank by a variable called the *risetime* and noted $t_{1/2}$. The *risetime*, illustrated on the right of Fig.4.19, corresponds to the amount of time taken by the signal in a station to go from 10 to 50% of its total value. The *risetimes* of all the selected stations of an event are combined in a single variable called Δ. This variable is based on a benchmark function describing the data and the average behaviour of $t_{1/2}$ as function of the distance r from the shower axis [126] and the zenith angle. The benchmark function is drawn on the right panel of Fig. 4.19. For each station i at distance r_i, is determined the deviation between the measured *risetime* $t_{1/2}$ and the value given by the benchmark $t_{1/2}^{bench}$ at the same distance, in units of benchmark standard deviation $\sigma_{t_{1/2}}^{bench}$. Δ represents the average of this "normalised" *risetime* over the selected stations, as in Eq.4.15.

$$\Delta = \frac{1}{N_{sel}} \sum_{i=1}^{N_{sel}} \frac{t_{1/2}(r_i) - t_{1/2}^{bench}(r_i)}{\sigma_{t_{1/2}}^{bench}(r_i)} \tag{4.15}$$

The other variable, L_{LDF}, used in the analysis evaluates the steepness of the LDF with respect to the NKG function introduced in Sec. 4.2.2 and used to describe the bulk of data. This observable describes the average ratio between the integrated signal in a station at distance r_i (with $r_i > 1000$ m) and the expected signal from data at the same distance. With a steeper LDF, stations sufficiently far enough should have a smaller signal for photon primaries, hence the threshold at 1000 m. Therefore, the value of L_{LDF} should then be smaller for photon-induced showers. In Eq. 4.16, N_{sel} is the number of selected stations having $r_i > 1000$ m, $S(r_i)$ is the integrated signal in station i and $LDF(r_i)$ corresponds the expected signal for data at distance r_i.

$$L_{LDF} = \frac{1}{N_{sel}} \sum_{i=1}^{N_{sel}} \frac{S(r_i)}{LDF(r_i)} \tag{4.16}$$

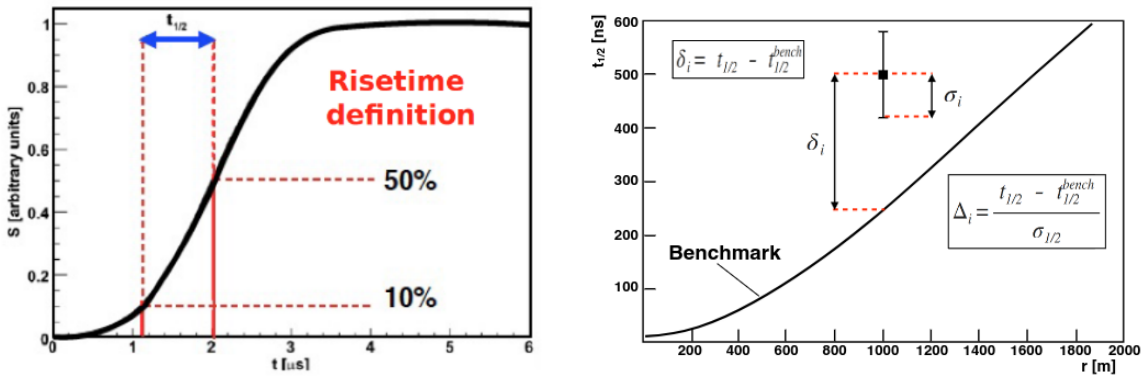

Figure 4.19: Left: Illustration of the risetime $t_{1/2}$. The figure shows the cumulated signal from a station in arbitrary units as function of time. The risetime is indicated by the blue range. Right: Illustration of the individual Δ_i of each station i. Taken from [126].

As explained in Sec. 4.2.2, the energy estimator S_{1000} is derived from the reconstructed LDF parameterised on data, mainly composed of hadronic showers. However, as stated in Sec. 4.3.1 the LDF of photons is on average steeper with respect to hadrons, and this energy estimation leads therefore to an under-estimation of the photon energy. The energy assigned to photons in the analysis is taken from a look-up table in bins of S_{1000} and the zenith angle θ. In this table built using simulations of non-preshower photons, the mean value of the Monte Carlo energy is reported and the events are weighted according to the E^{-2} spectrum (see Sec. 5.3.1). The energy resolution is of $\simeq 30\%$ for non-preshowering photons and the bias is around -30% for preshowering photons.

To ensure a good reconstruction of events and to optimise the photon search, some selection criteria are applied to the data set:

- Only events between 30° and 60° are used. This ensures that most photons reach their maximum of development before hitting the array.

- All the stations surrounding the WCD with the highest signal must be working (the direct neighbours).
- The standard SD energy must be higher than $10^{18.5}$ eV as it corresponds to the minimal energy of the simulations used in the analysis.
- Only non saturated stations above 6 VEM and within a distance range of 600 m to 2000 m are used in the calculation of Δ.
- For the computation of L_{LDF}, it is required to have at least one station above 1000 m from the axis.

The variables used in the analysis are energy and zenith dependant. To remove these dependencies and define a selection criteria for photons candidates that is not dependent on the energy or zenith, the observables are redefined as:

$$\tilde{\Delta} = \frac{\Delta - < \Delta > (S_{1000}, \theta)}{\sigma_{\Delta}(S_{1000}, \theta)} \tag{4.17}$$

$$\tilde{L}_{LDF} = \frac{L_{LDF} - < L_{LDF} > (S_{1000}, \theta)}{\sigma_{L_{LDF}}(S_{1000}, \theta)} \tag{4.18}$$

In Eq. 4.17 (Eq. 4.18), $< \Delta > (L_{LDF})$ corresponds to the mean of the Δ (L_{LDF}) distribution in the corresponding bin of S_{1000} and θ for non-preshower photon simulations, and σ_{Δ} ($\sigma_{L_{LDF}}$) to the standard deviation of the distribution in the bin. Thus, the resulting observables are centered around the average value for non-preshower photons in units of the standard deviation.

A Fisher Discriminant analysis (see Sec. 7.2) with the photon simulations and the burn sample of data is performed combining $\tilde{\Delta}$ and $\tilde{L}_{LDF}$. The candidate selection cut is chosen as the median of the non-preshower photon distribution on the Fisher axis. As the burn sample represents a very small fraction of data ($\simeq 1.8\%$), the tail of the burn sample is fitted with an exponential to estimate the expected background. Finally, the rest of the SD data collected between the 1st of January 2004 and 30 June 2020, apart from the burn sample, is analysed and 16 photon candidates are found. This number is in statistical agreement with the expectations from the fit of the burn sample tail. The left panel of Fig. 4.20 shows the search sample (red) and the photon simulations (contours) in the ($\tilde{\Delta}$,$\tilde{L}_{LDF}$) plan. The plain line indicates the Fisher axis and the dashed line the selection cut. The distributions projected on the Fisher axis are reported in the right panel for photon simulations in blue (light for preshowers and dark for non-preshowers) and for data in red. The burn sample is represented by the normalised grey filled histogram along with the fit of the tail (black dashed line). The selection cut is indicated by the black plain vertical line. In the end, limits on the UHE photons flux with a 95% confidence level are computed and are reported on Fig. 4.21 by grey circles. With the limits derived from the hybrid data set, they are beginning to constrain the prediction from a pure-proton GZK photon flux as well as SHDM models of photon production.

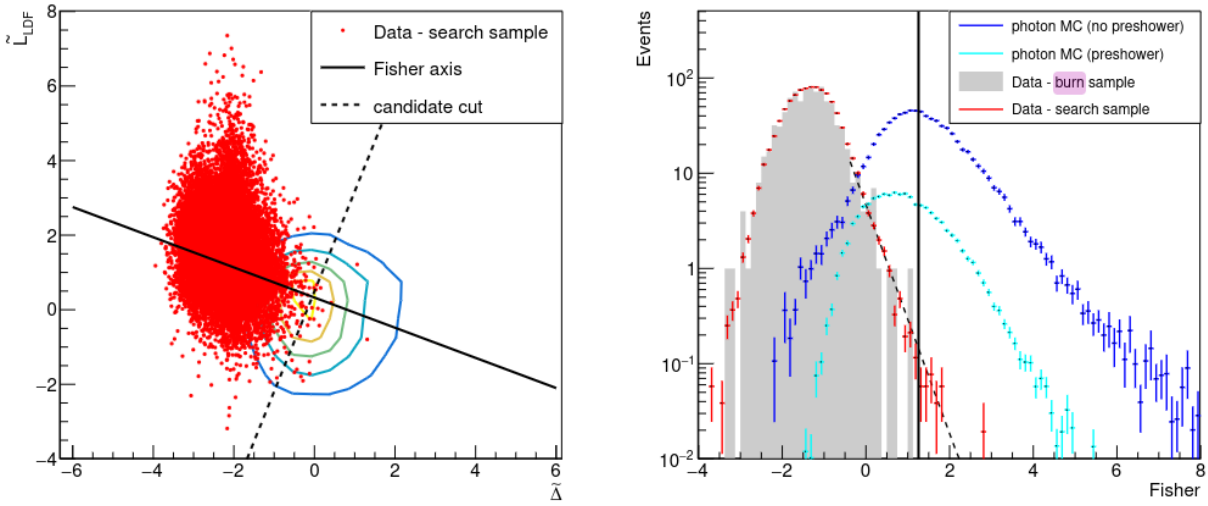

Figure 4.20: Left: The data search sample (red) and the non-preshower photon simulations (contours) in the ($\tilde{\Delta}$,$\tilde{L}_{LDF}$) plan. The Fisher axis is indicated by the plain line while the selection cut is represented by the dashed line. Right: Projection on the Fisher axis of the distribution of data (red), non-preshower photons (dark blue), preshower photons (light blue) and burn sample (grey). The fit of the burn sample tail is also represented. Taken from [32].

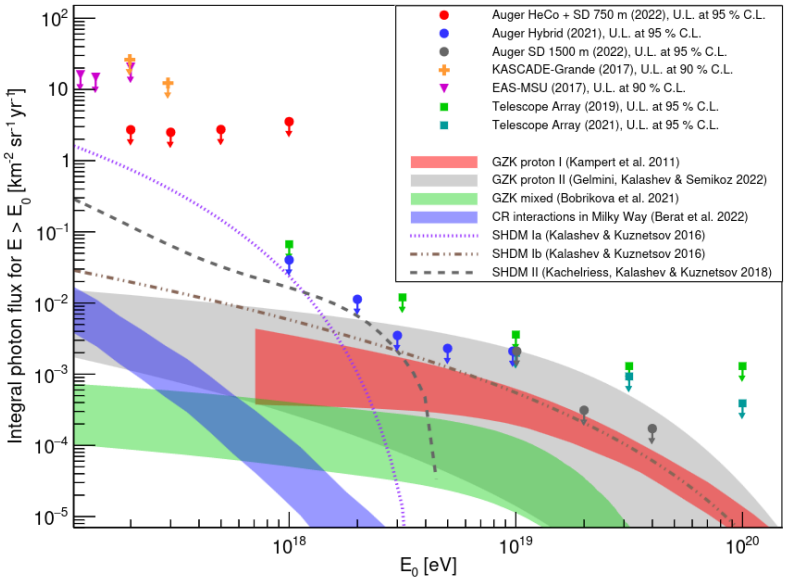

Figure 4.21: Current upper limits of the integrated photon flux for energies above 10^{17} eV [21]. The limits derived from the data collected by the SD-750 and HeCo are reported in red [122], the ones derived from hybrid data and universality are shown in blue [71], and the SD-1500 limits are in grey [32]. Limits from other experiments than Auger are reported: KASCADE-Grande by orange crosses [69], EAS-MSU by purple triangle [68] and Telescope Array by green [70] and blue squares [124]. The expected flux from the GZK effect for protons (red and grey bands) and a mixed composition (green band [54]) are shown. The expected photon flux from different SHDM scenarios are depicted by lines. Finally, the flux computed in Sec. 3 is illustrated by the blue band.

Above 10^{18} eV, the Telescope Array (TA) Collaboration published constraints on the flux of UHE photons in [124]. Their detector consists of the combination of a 700 m^2 ground array (scintillators) with 3 fluorescence telescopes, but the limits reported in [124] are derived only from the data provided by the surface detector. The observables used by the TA collaboration also exploit the specificities of photon-induced showers. 16 observables are combined in a boosted decision tree (BDT) and trained on proton and photon simulated showers. Independent BDT are built for different thresholds in energy. The selection cut to identify photon candidates is zenith dependant and no photon candidate has been found in the data. The limits derived from this are reported by blue squares in Fig. 4.21.

Summary

The underlying physics and the main features of EAS were presented and described analytically by simple models allowing to highlight the main parameters on which the development of these showers depends, namely X_{max}, the primary energy and the number of muons.

In the next chapters, simulations of showers of photon and proton primaries detected at the Pierre Auger Observatory are used to develop an universality-based analysis aiming to identify UHE photon among UHECRs. The Observatory was presented in this chapter with an emphasis on the surface detector as it corresponds to the data sets used in this thesis work.

The specificities of photon-induced shower with respect nuclei primaries, used to design the discriminating observables exploited in the search of UHE photons were explained thoroughly. The analyses designed with the data collected at the Observatory were presented and, in the absence of photon candidates, the limits on the integrated UHE photon flux derived from each of them are reported in Fig. 4.21.

We saw in this chapter that the use of the universality of air showers allowed to put more constraining limits on the UHE photon flux in the hybrid analysis. In the following chapters, an analysis based on the universality and using the SD data is designed, as detailed in Sec. 6, to reconstruct the X_{max} and the energy of photon-induced showers with the goal of improving the performance of the photon search in the SD data.

Chapter 5

Universality of extensive air showers and UHE photons

Contents

In this chapter, we present the concept of air shower universality stating that the average properties of an EAS can be described by a few macroscopic shower characteristics: the primary energy, the slant depth of the maximum of the shower development and the muon content. Afterwards, the model based on this principle developed in the context of the Pierre Auger Observatory predicting the integrated signal and the time distribution of the signals in a WCD is presented. Finally, the validation of this model is performed, aiming to check if the simulated photon showers used in the present work are correctly described by universality. The validation step is mandatory before designing an universality-based reconstruction.

5.1 Concept of air shower universality

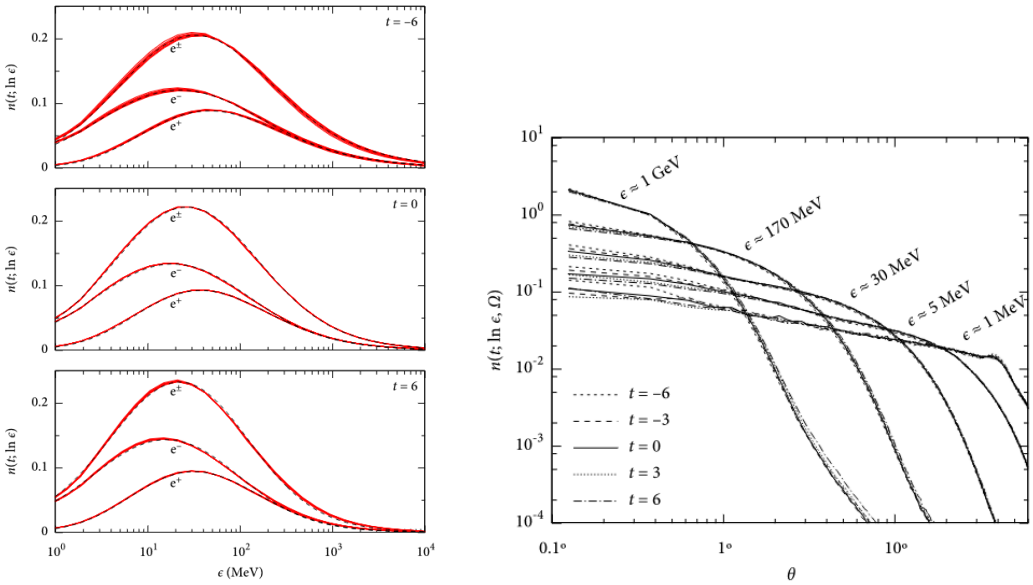

Figure 5.1: Left: Average energy distributions (red) of electrons, positrons and the sum of both are shown for three stages of shower development t (-6, 0, and 6). The distributions are obtained from simulations of proton, iron and photon primaries for three different energies (10^{17}, 10^{18} and 10^{19} eV). The black dashed line indicates the parameterisation developed in [127]. Right: Average angular distributions of electrons for different values of their energies ranging from 1 MeV to 1 GeV. They are reported for 6 stages t and were obtained using 20 simulations of proton-induced showers of $E = 10^{18}$ eV. Taken from [127].

The concept of the universality of extensive air showers appeared in the middle of the twentieth century with the first works on electromagnetic showers by Rossi and Greisen [128]. The main idea behind universality is that the secondary particles of air showers share similar distributions for a same stage of development: energy spectrum, lateral and angular distributions and longitudinal profiles. This results from the very important amount of secondary particles originating from the cascade processes produced following the interaction of the cosmic ray with the atmosphere (more than 10^{11} for a 10^{20} eV proton). The large number of interactions reduces the fluctuations leading to a smoothing of the shower properties. Thus, the distributions of particles can be described only by a few parameters.

The understanding of universality was developed a lot more during the last decades thanks to the progresses in MC simulations. Indeed, the study of simulated showers [129] [130] [127] [131] showed that energy spectrum and angular distributions of electrons and positrons shared a precise universal shape that can be determined only using few shower parameters. In [127], a complete study of the universal features of secondary electrons and positrons in EAS was performed. The distributions of these particles were studied as function of the primary energy, zenith angle, mass and the stage of development of the shower. Some parameterisations of the energy spectra, angular and lateral distributions were performed.

$$t = \frac{X - X_{max}}{X_0} \tag{5.1}$$

$$s = \frac{3X}{X + 2X_{max}} \tag{5.2}$$

In [127], t is used to describe the stage of longitudinal development of the shower and is characterised by the relative depth to the shower maximum as in Eq. 5.1. It is expressed in units of the radiation length of electrons is air $X_0 \simeq 36.7$ g.cm^{-2}. By definition, the maximum of the shower development corresponds to $t = 0$, and is negative before the maximum. In [131], the concept of the shower age s, appearing together with the first observation of EAS universality, is explained thoroughly. Expressed in Eq. 5.2, the age s is a similar way to describe the shower longitudinal development in [127], the authors demonstrated that the longitudinal description of air showers with respect to their maximum, using t or s, shows a higher degree of universality than the only use of the depth X. Although both t and s are appropriate variables to highlight the universal features of secondary particles, the study in [127] shows that t remains the better choice when comparing statistical fluctuations.

The study performed in [127] highlights firstly that the energy spectra of secondary electrons and positrons present a similar shape for a certain stage of development t. Using simulated showers of different primary nuclei and energies, the average energy distributions of secondary electromagnetic particles are computed. In Fig. 5.1, these average energy distributions for electrons, positrons and their sum are reported for three stages t of -6, 0, and 6 from top to bottom respectively in an energy range from 1 MeV to 1 GeV. The parameterisation developed is indicated by the dashed lines and shows a precise description of the distributions. The universal behaviour of the energy distributions is evident.

In the same work, the angular distributions of secondary electromagnetic particles was observed to depend on the particle energy, but not on the stage of development t. The distributions of particles as function of their momentum angle with respect to the shower axis (equal to 0° when parallel and to 90° when perpendicular) are reported in Fig. 5.1 for several values of t and five electron energies. We observe smaller dispersions when close to the axis with a drop depending on the particles energy. However, the dispersions are more important for low energy particles (noted ϵ on the figure). The authors also showed that the distributions are not dependent of the stage, and no dependencies on the primary zenith on energy were found.

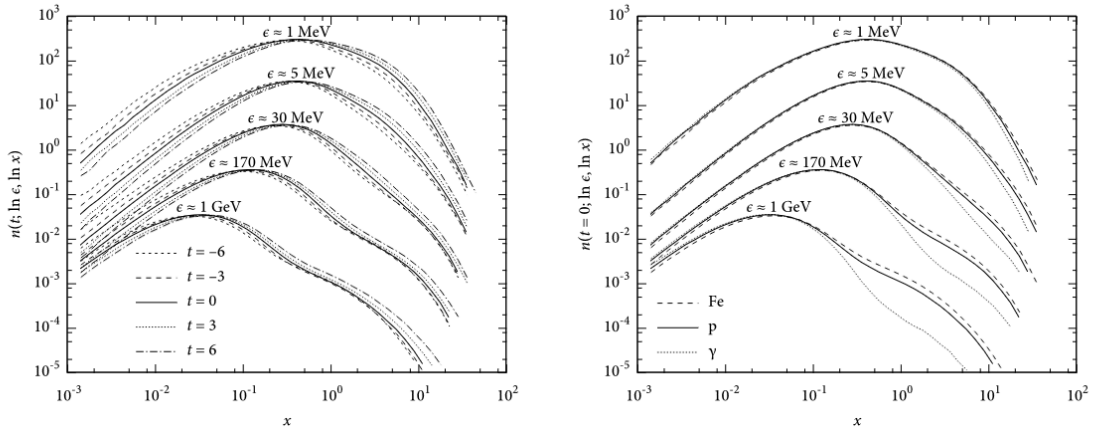

Figure 5.2: Left: Average lateral distributions of electrons for 20 proton showers of 10^{18} eV, for different stages of development t and electron energies. Right: Average lateral distributions for different primaries (proton, iron and photon) and electron energies. Taken from [127].

Another evidence on the universal behaviour of electromagnetic particles in EAS is found by studying their lateral distributions expressed as function of x defined as:

$$x = \frac{r}{r_M} \tag{5.3}$$

where r is the the distance to the shower axis and r_M is the Molière radius characterising the lateral development of electromagnetic cascades by taking into account the air density and the radiation length of electrons in air. These distributions of electrons are reported in the left panel of Fig. 5.2 [132] for several stages t and electron energies, and for several primary nuclei in the right panel (proton, iron and photon). We observe a dependence on the electrons energies and the stage of development t. Along the lateral profile, two contributions are present. First, close to the axis, the first peak does not depend on the mass of the primary and originates from the electromagnetic part of the shower. The second contribution is clearly dependent on the nature of the primary and is fed by the charged pions channel. These pions are present in the hadronic part of the shower and tends to be further from the axis with respect to electromagnetic particles and is therefore less visible for photons as the hadronic part of the shower is less important.

This mass-dependent behaviour at larger distances from the axis originating from the charged pions channel, led to the introduction of the muonic component into the universality of EAS. In [133] and [134], the longitudinal profile of muons was studied for different primaries and hadronic interaction models, as well as several energies and zenith angles. It was reported in [133] that the longitudinal distributions of muons share an universal shape. Indeed, a high degree of universality is observed when the longitudinal development is expressed as function of $X - X^{\mu}_{max}$ (maximum depth of the muonic component) and the muon number is normalised by its maximum value $N_{\mu,max}$ for each shower. The left panel of Fig. 5.3, shows the muon profile as function of the depth X for proton (red) and iron primaries (blue) with $E = 10^{19}$ eV and $\theta = 40°$. Both X and the muon number are not optimal to highlight universal features in the muon profiles. On the other hand, the right panel of Fig. 5.3 illustrates the same distributions but as function as the depth

centred on the maximum of the muonic component and the normalisation of the muon number, as described previously. Finally, we do observe the universal shape of the longitudinal profiles of secondary muons in EAS.

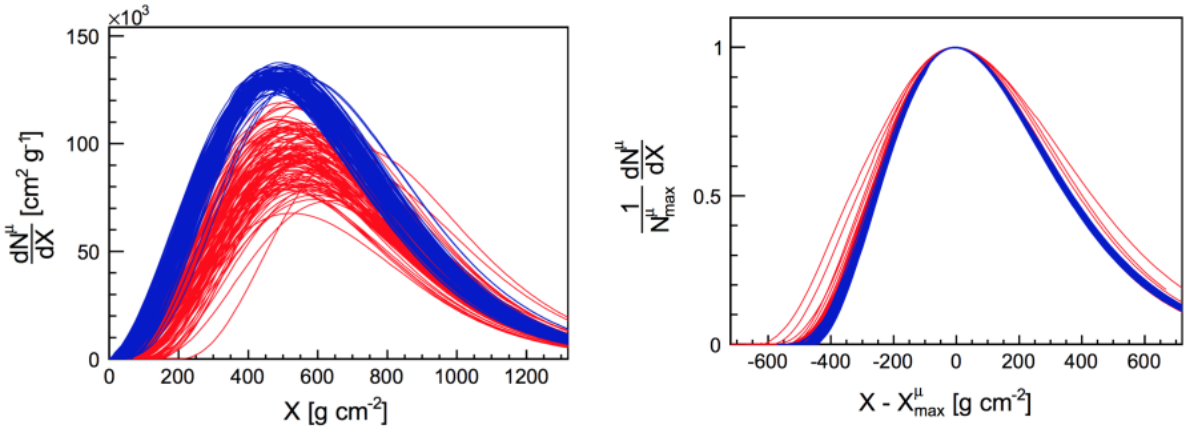

Figure 5.3: Right: Longitudinal profiles of muons as function of the depth X for proton (red) and iron (blue) induced showers of $E = 10^{19}$ eV and $\theta = 40^{\theta}$. Right: The same profiles are centred on X^{μ}_{max} and normalised by $N_{\mu,max}$. Taken from [133].

The universal features of EAS development studied using MC simulated showers have allowed a better understanding of these behaviours. Thus, such properties can be exploited to predict the distributions of particles at ground and therefore predict the signals they create in the SD stations. Accordingly, a model based on universality was developed within the Pierre Auger Collaboration to predict the integrated signals and their shapes in WCDs [135] [132]. In this model, the shower secondary particles are described by four components which all behave universally: the pure electromagnetic component, the electromagnetic component from muon decays, the electromagnetic component from low energy hadrons and the pure muonic component. This model is described in the following sections.

5.2 The universality model for signals in the surface detectors

From the concept of the universality of extensive air showers, we saw that the distributions of secondary particles at ground can be described with good accuracy only using a few global shower parameters: the primary energy E, the maximum depth of development X_{max} and the muon content of the shower N_{μ}. Based on this paradigm, models aiming to predict the signals in ground detectors have been developed.

Initially, the models built predicted the signals at the optimal distance $r_{opt} = 1000$ [136] (see Sec. 4.2.2), and only two shower components were considered: the electromagnetic part and the muonic part. As explained in Sec. 4.1, the electromagnetic part depends only

on E and X_{max}. On the other hand, the muonic component, in addition to its dependence on both parameters, is heavily related to the nature of the CR. The following years, a new parameterisation of the integrated signals in WCDs has been developed [135], and introduced another shower component: the electromagnetic particles originating from low energy hadrons and representing the most part of the electromagnetic component at large distances from the axis due to sub-showers with large transverse momentum.

Finally, the scheme used in [135], for the prediction of the integrated signals in WCDs, is followed in [132] to predict the arrival time distribution of particles in the stations. Both of these models are presented hereafter and will be referred to as the *Signal Model* and *Time Model* respectively.

5.2.1 Signal model: normalisation of the SD signal

In [135], a model describing the integrated signal in a WCD was developed. Indeed, following the observations described in Sec. 5.1, which highlight that the distributions of secondary particles share universal behaviours, an analytical parametrisation of the particles distributions at ground convoluted with the detector response, was derived for each of the four components:

- the pure electromagnetic component
- the electromagnetic component from muon decays
- the electromagnetic component from low energy hadrons
- the pure muonic component

This was done using proton simulations generated with the QGSJetII-03 hadronic interaction model with zenith angle below 60° and energies between 4×10^{18} and 10^{20} eV. The parametrisation is performed for distances from the shower axis ranging from 100 m to 2000 m.

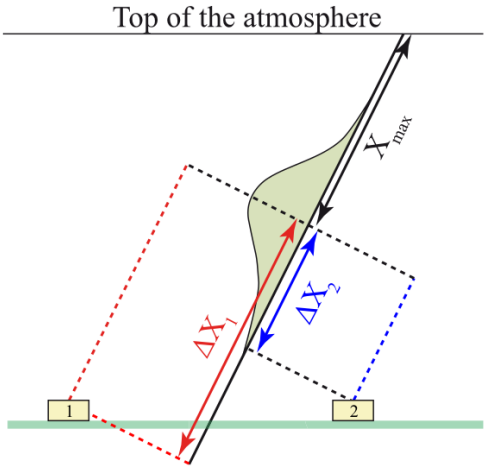

Figure 5.4: Illustration of ΔX, the difference in depth between the maximum of development X_{max} and the projected height of the WCD.

EAS are described using the primary energy E, the depth of the shower maximum X_{max}, the zenith angle θ, the air density at ground ρ^{air}_{ground} and the muon content N_μ. N_μ for a shower is defined as the muon density at 1000 m from the shower axis with respect to proton-induced showers simulated with the hadronic interaction model QGSJetII-03, as explained in more details in Sec. 6.1.3. The average signal in a station at distance r from the axis and with azimuth angle ϕ[1], originating from a shower described by (E, X_{max}, N_μ, θ, ρ^{air}_{ground}) is expressed in Eq. 5.4.

$$S(r,\phi|E,X_{max},N_\mu,\theta,\rho^{air}_{ground}) = \sum_{i=1}^{4} S^i_0(r,\Delta X|E)\ f^i_{mod}(r,\phi|\theta)\ f^i_{atm}(r|\rho^{air}_{ground})\ f^i_{conv}(r,\Delta X,\phi|\theta)\ f^i_{N_\mu fluc}(r|N_\mu) \tag{5.4}$$

where i indicates the four shower components. ΔX describes the stage of development and is defined as the difference in depth between X_{max} and the depth at the projected height of the detector, as illustrated in Fig. 5.4. The definition of the different functions used in the Eq. 5.4 are described in the following:

- S^i_0 is the signal detected in an ideal detector, in which the signal deposited by a particle does not depend on its arrival direction. This means that the ground is not accounted for (particles can comes from all directions), and the zenith angle of the shower is considered to be $\theta = 0°$.
- f^i_{mod} describes the changes of S_0 as function of θ and ϕ. Indeed, the atmospheric profile changes with the zenith angle, and for showers with $\theta \neq 0°$, dependencies on ϕ also arise (see Sec. 6.1.2).
- f^i_{atm} accounts for the changes in the atmosphere profile depending on the season of the year, as well as day and night changes.
- f^i_{conv} converts the signal detected by an ideal detector into a realistic detector. Therefore, the detector response is dependent on the arrival direction of the particles and no particle can arrive from below ground level.
- $f^i_{N_\mu fluc}$ describes the correlations between the signal components and the muon content of the shower N_μ.

The factor f_{conv} takes into account the zenith angle of the particles, θ_p, in order to reject particles with zenith angles greater than 90° which are unable to reach the detectors at ground. The cosine of the angle between the particle direction and the shower axis, p_z is also used. Moreover, the projected area of the detector in the particle direction $A_{mod}(\theta_p)$, equal for all directions in the ideal case, is integrated. Finally, the convolution of the energy spectrum with the detector response $T_{mod}(\theta_p)$ is added and the factor f_{conv} is expressed in Eq. 5.5.

[1]The azimuth angle of a station ϕ is defined as the angle between the projection of the shower axis in the shower plane and the position of the station in the shower plane.

$$f_{conv} = \int_{p_z^{cut}}^{1} \frac{\mathrm{d}S_0}{\mathrm{d}p_z} T_{mod}(\theta_p|r, p_z) A_{mod}(\theta_p) \mathrm{d}p_z \tag{5.5}$$

The parametrisation of $f_{mod}(r, \phi|\theta)$ is presented in Eq. 5.6. M_0 describes the change in the normalisation of S_0 with r and θ for a station azimuth angle of $\phi = 90°$, and M_1 corresponds to the $\cos\phi$ modulation depending on r and θ.

$$f^i_{mod}(r, \phi|\theta) = M_0(r, \theta)(1 - M_1(r, \theta)\cos\phi) \tag{5.6}$$

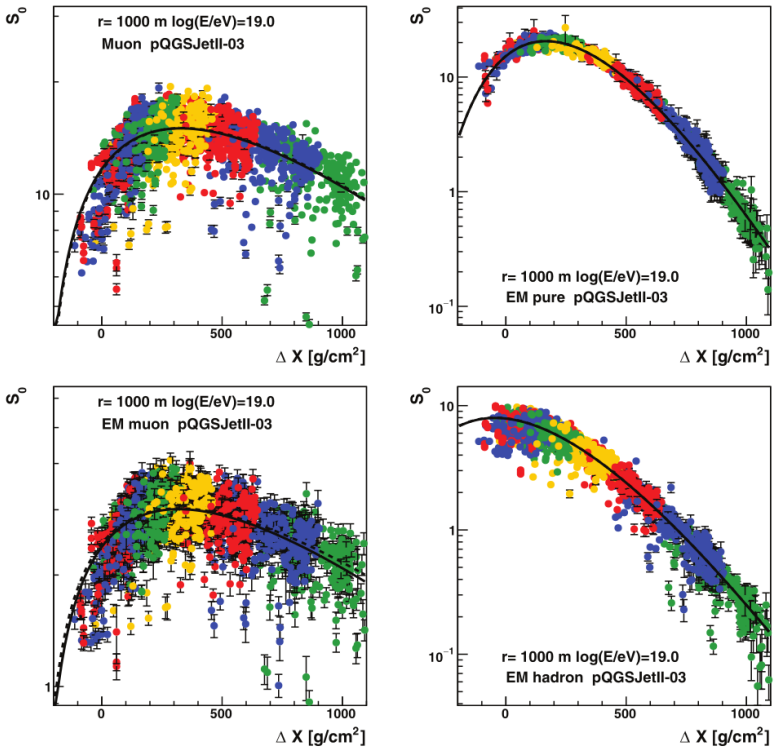

Figure 5.5: Fits of S_0 as function of ΔX for each shower component for $r = 1000$ m, $\phi = 90°$ and $E = 10^{19}$ eV. The fits are indicated by solid black lines. The different colours corresponds to different zenith angles and each point corresponds to a sampling area of the simulated showers. Taken from [135].

The Molière radius fluctuates along with the atmospheric density variations during days and seasons, leading to modifications of the electromagnetic signal at ground. The parametrisation of f_{atm} can be found in [135].

The signal in an ideal detector, S_0, is also estimated using the MC simulations of protons. For each distance r from the shower axis and each shower component, S_0 is parameterised with a Gaisser-Hillas function as:

$$S_0^i = S_{ref}^i \left(\frac{E}{10^{19}\text{eV}}\right)^{\gamma} \left(\frac{\Delta X - \Delta X_0^i}{\Delta X_{ref} - \Delta X_0^i}\right)^{\frac{\Delta X_{max} - \Delta X_0}{\lambda^i(E)}} \exp\left(\frac{\Delta X_{ref} - \Delta X}{\lambda^i(E)}\right) \tag{5.7}$$

In Eq. 5.7, S_{ref}^i is the signal at $\Delta X_{ref} = 400$ g/cm^2 and $\lambda(E) = \lambda_0 + f_\lambda \log_{10}(E/10^{19}\text{eV})$. Along with ΔX_{max}, $\lambda(E)$ have been fitted for each distance r. The value of f_λ and ΔX_0 can be found in [135] and are fixed for each of the four shower components. Fig. 5.5 represent S_0 as function of the longitudinal profile ΔX for each shower component. It is reported for $r = 1000$ m, $\phi = 90°$ and $E = 10^{19}$ eV. The different colours corresponds to different zenith angles and each point corresponds to a sampling area of the simulated showers (slice in the ring centred around the shower axis which depends on the distance r, azimuth ϕ and stage of development ΔX). The fits of S_0 are indicated by solid black lines. One can notice that the muonic component is less attenuated at later stages of development with respect to the pure electromagnetic component.

Finally, the correlations between the signal components and the muon content, $f_{N_\mu fluc}$, are parameterised by studying the correlation between the ratios $S_0^{EM}/S_{0,ref}^{EM}$ of the three electromagnetic components, with $S_0^\mu/S_{0,ref}^\mu$, for $\theta = 36°$, $E = 10^{19}$ eV and $\phi = 90°$ (see Fig. 5.6). S_{ref} refers to the parameterised value of S_0 for the reference of QGSJetII-03 proton MC simulations. The colours represent different simulated primaries and hadronic interaction models. For $r = 100$ m, the left panel shows the ratio for the pure electromagnetic component. On the middle panel is reported the electromagnetic component from muons for $r = 1000$ m, and the third electromagnetic component from low-energy hadrons is in the last panel. In each panel the fit by a linear function as in Eq. 5.8 is indicated by a solid line. α shows a dependence of r only in the case of the electromagnetic component from hadrons and its parametrisation is found in [135].

$$\frac{S_0^{EM}}{S_{0,ref}^{EM}} = 1 + \alpha \left(\frac{S_0^\mu}{S_{0,ref}^\mu} - 1\right) \tag{5.8}$$

Eq. 5.8 provides a good description of the simulated proton reference as well as other interaction models (QGSJetII-03 and EPOS 1.99) and primaries (proton and iron), and with $N_\mu = S_0^\mu/S_{0,ref}^\mu$, $f_{N_\mu fluc}$ can be expressed as:

$$f_{N_\mu fluc} = 1 + \alpha\,(N_\mu - 1) \tag{5.9}$$

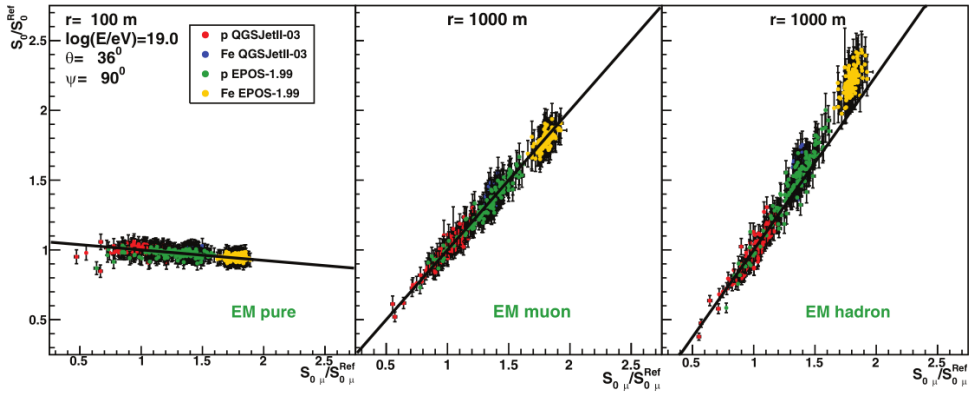

Figure 5.6: Correlations between the ratios $S_0^{EM}/S_{0,ref}^{EM}$ of the three electromagnetic components with $S_0^{\mu}/S_{0,ref}^{\mu}$. The pure electromagnetic component, the electromagnetic component from muons and the electromagnetic component from low energy hadrons are reported respectively from left to right. The showers were simulated for $\theta = 36°$, $E = 10^{19}$ eV, and the azimuthal angle of stations is $\phi = 90°$. Taken from [135].

Overall, the prediction of the integrated signals in WCDs developed in [135] shows an accuracy better than 10% for the whole ranges of zenith angles (below 60°) and energies (between 4×10^{18} and 10^{20} eV). The model has been tested on different hadronic interaction models (QGSJetII-03 and EPOS-1.99) and primary nuclei (proton and iron) and shows similar accuracy. Accordingly, Fig. 5.7 shows the average ratio of the simulated signal with respect to the prediction. It is reported as function of the distance r for different primaries (proton and iron), hadronic interaction models (EPOS-LHC [61] and QGSJetII-03 [63]).

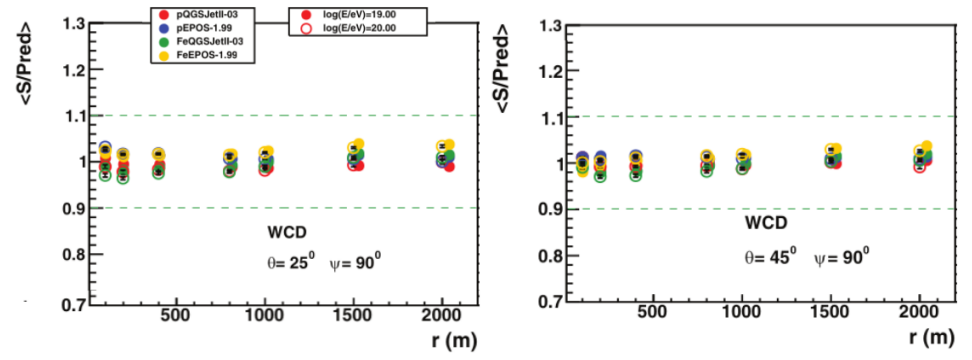

Figure 5.7: Right: The average ratios of the simulated signal with respect to the prediction as function of the distance r for different primaries (proton and iron) and hadronic interaction models (EPOS-LHC [61] and QGSJetII-03 [63]). It is shown for a zenith angle of 25° at two energies and for $\phi = 90°$. Right: Similar figure for a zenith angle of 45°.

5.2.2 Time model: shape of the SD signal

With a procedure similar to the one described in Sec. 5.2.1, the shape of the signals in the WCDs for each of the four shower components was parameterised. The arrival time

distributions of particles at ground measured by the stations are described in [132] and derived from proton MC simulations generated with QGSJetII-03. The zenith angle of these simulated showers ranges from 0° to 60°, and the energies go from 4×10^{18} eV to 10^{20} eV.

In [132], the arrival time distribution of secondary particles in a WCD, $\frac{\mathrm{dS}}{\mathrm{dt}}$, corresponds to the time distribution of particles convoluted with the detector response. It is described by a log-normal ansatz as in Eq. 5.10, in which t_0 corresponds to the time under which no particle is expected.

$$\frac{\mathrm{dS}}{\mathrm{dt}}(\mathrm{t}) = \frac{1}{\sqrt{2\pi}(\mathrm{t}-\mathrm{t_0})\mathrm{s}} \exp\left(\frac{-(\ln(\mathrm{t}-\mathrm{t_0})-\mathrm{m})^2}{2\mathrm{s}^2}\right) \tag{5.10}$$

In this section, we present the origin of times parameterised in [132] as function of the zenith angle θ, the maximum depth of development X_{max} and the primary energy E. Then, the parameterisation of the two other parameters appearing in the log-normal ansatz, namely m and s, are addressed as function of $(r, \Delta L, \phi|\theta, E)$. Here, ΔL describes the longitudinal development of the shower, similarly to ΔX. However, it corresponds to the distance between the maximum development of the electromagnetic shower and the projected height of the detector.

In [132], a spherical shower front is considered with the centre of the sphere being the origin of time. However, the origin of times is not derived from the first interaction depth of the shower X_{fisrt}. Indeed, in a shower, particles starts to deviate from the shower and acquire a sufficient lateral spread only after travelling a depth between 100 and 200 g.cm^{-2} after X_{first}. Therefore, the optimal value of the origin of times is found between X_{fisrt} and X_{max} and is noted D_{T0}, defined as the distance from the origin of times to the electromagnetic X_{max}.

The determination of D_{T0} is necessary to predict the start time of the signals generated by each component. To obtain the parameterisation of D_{T0}, the values of (t_0, m, s) are derived for each component from the 1%, 10%, and 50% quantiles of the average traces at $\phi = 90°$ and for sampling areas at 800 m. Average traces are defined as what would be measured if the same shower was recorded multiple times (a more precised definition can be found in. [135]). The 800 m distance was chosen as a compromise between shower particle statistics and the width of the shower front. For each simulated shower and for each component, the three quantiles are used for the fitting of the trace with the log-normal distribution in Eq. 5.10 from which one obtains (t_0, m, s). On the left panel of Fig. 5.8, the simulated muonic trace of a proton shower with $\theta = 36°$ and $E = 10^{20}$ eV is shown. The blue trace is simulated without taking into account the muon decaying inside the WCD which is not the case for the red one, muon decay inside the WCD is considered. The log-normal trace fit is indicated the by the black dashed line. We observe a deviation from the log-normal ansatz for larger times due to these muon decays. However, the log-normal ansatz provides a good description for the earlier part of the trace, and the issue arising at larger times is not treated in the model.

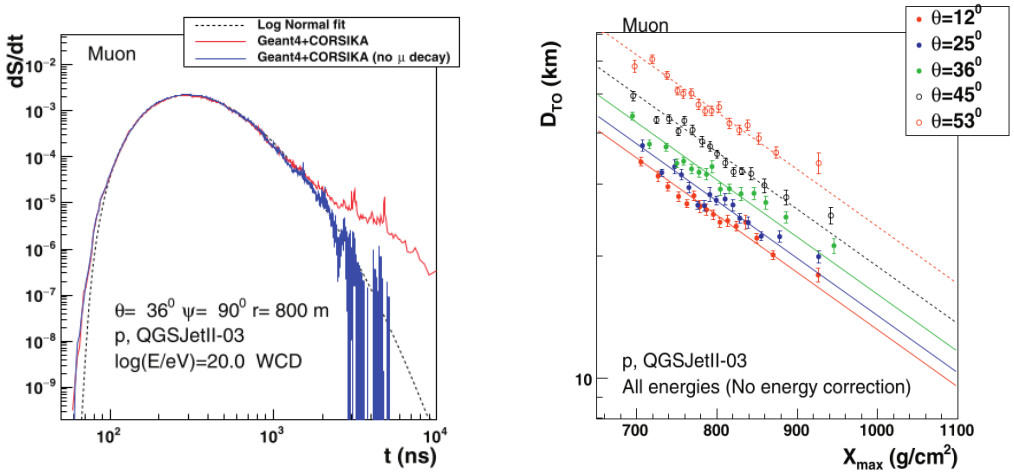

Figure 5.8: Left: Example of a log-normal trace fit for the muonic component. The fit is indicated by the black dashed line. The simulated shower used is a proton shower with $\theta = 36°$ and $E = 10^{20}$ eV. The blue trace is simulated without taking into account the muon decaying inside the WCD which is not the case for the red one, muon decay inside the WCD is considered. Right: The values of D_{T0} for different zenith angles (colours) as function of X_{max} for the muonic component. All energies are used. Taken from [132].

Finally, the values of t_0 obtained through the fit procedure are used to compute D_{T0} for each shower and a parameterisation can be derived as function of the shower global parameters. Electromagnetic particles go through several scattering before entering the stations. On the other hand, muons undergo almost no interactions after their production. Thus, a distinction is made between the shower components because of the differences in the propagation of the electromagnetic particles with respect to the muons. In Eq. 5.11 the parameterisation of D_{T0} is reported for the muonic and electromagnetic from muon components, and in Eq. 5.12 for the two others universality components. The left panel of Fig. 5.8 shows the values of D_{T0} in km for different zenith angles as function of X_{max} for the muonic component. All energies are used, and by looking both at the Fig. 5.8 and Eq. 5.11, we observe that D_{T0} depends primarily on the zenith angle and X_{max} while the dependence on the energy is weak.

$$D_{T0}(X_{max}, \theta, E) = (D_0(\theta) + D_1 \log_{10}(\frac{E}{10^{19}\text{eV}})) \exp\left(\frac{-(X_{max} - 750\text{g/cm}^2)}{D_2}\right) \quad (5.11)$$

$$D_{T0}(X_{max}, \theta, E) = D_0(\theta) + D_1 \log_{10}(\frac{E}{10^{19}\text{eV}}) + D_2 \frac{X_{max} - 750\text{g/cm}^2}{200\text{g/cm}^2} \quad (5.12)$$

As stated previously, the values of m and s in Eq. 5.10 are obtained with the average traces fits of the 10% and 50% quantiles. They are calculated for all showers and sampling areas and the parameterisation is performed as function of $(r, \Delta L, \phi|\theta, E)$. The functional form for m and s is reported in Eq. 5.13. ΔL_{ref} corresponds to the value of ΔL for a

reference X_{max} of 750 g/cm^2 and the corresponding zenith angle. While an analytical form is found for $a_1(r)$, $a_2(r)$, $a_3(r)$ and $a_6(r)$, the values of $a_4(r,\theta)$ and $a_5(r,\theta)$ are interpolated in r and θ. The top panels of Fig. 5.9 show the parameter m as function of ΔL for the muonic (left) and pure electromagnetic component (right). It is reported for different distances r (400, 800 and 2000 m) and azimuth angle ϕ (0°, 90° and 180°), for an energy of 3.2×10^{19} eV. The bottom panels of Fig. 5.9 show the identical thing for s. The accuracy of the parametrisation is found to be better than 2% on the whole parameters space.

$$\begin{cases} m(r,\Delta L,\phi|\theta,E) \\ s(r,\Delta L,\phi|\theta,E) \end{cases} = a_1(r) + a_2(r)\exp\left(\frac{-a_3(r)\Delta L}{1000}\right) + a_4(r,\theta)(\Delta L - \Delta L_{ref}) + a_5(r,\theta)\cos(\phi) + a_6(r)\log_{10}(\frac{E}{10^{19.5}\text{eV}}) \quad (5.13)$$

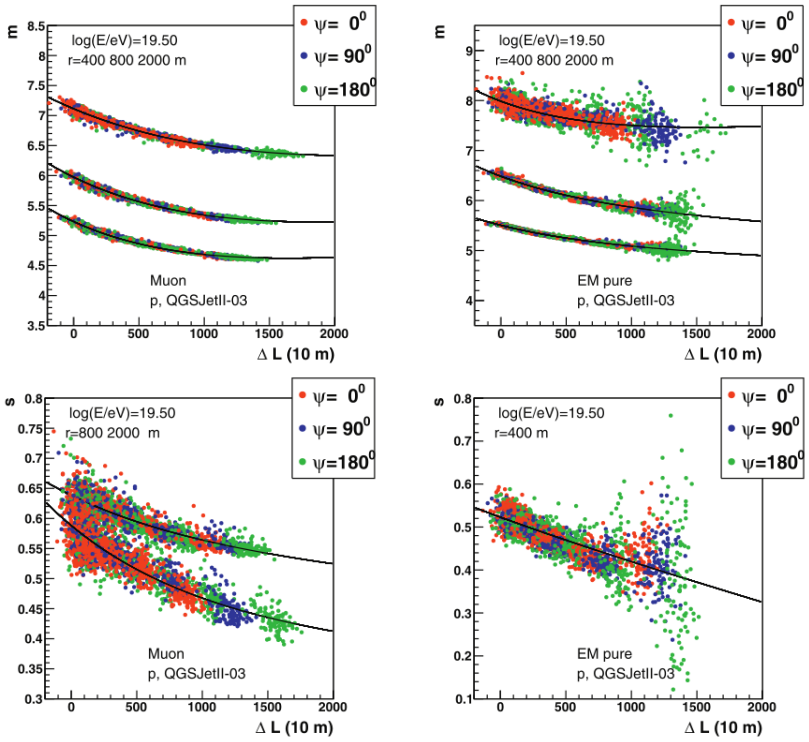

Figure 5.9: Top: The parameter m as function of ΔL for the muonic (left) and pure electromagnetic component (right). It is shown for different distances r (from bottom to top: 400, 800 and 2000 m) and azimuth angle ϕ (0°, 90° and 180°), for an energy of $10^{19.5}$ eV. Bottom: equivalent procedure for the parameter s. Taken from [132].

In [132], to determine the accuracy of the prediction of the traces shapes, the 1%, 10%, 50%, and 90% simulated quantiles are compared to their predicted value inferred from Eq. 5.13. The average ratio of the simulated quantiles with respect to the model are reported in Fig. 5.10 as function of the zenith angle, for different azimuths ϕ and distances

r. The dashed lines in each panels indicate the ±3% deviations. The authors obtain an accuracy better than 3% for the 1%, 10%, and 50% quantiles. However, deviations up to 20% are reached in the case of the 90% quantiles. This is caused by the muons decaying into the WCDs as mentioned previously and shown in Fig. 5.8. The model gives a very good description of the signals shape for the early part of the traces but should be updated for quantiles over 50%.

The Signal and Time Models developed in [135] and [132] demonstrate a good accuracy of the predicted signals obtained from the parameterisation on proton simulations for all zenith angles below 60° and energies between 4×10^{18} to 10^{20} eV. In the following, the universality model is used on a library of photon-induced shower simulations. To verify that the model gives a good description of these simulations, the predictions given by the Signal and Time models are compared to the true MC values.

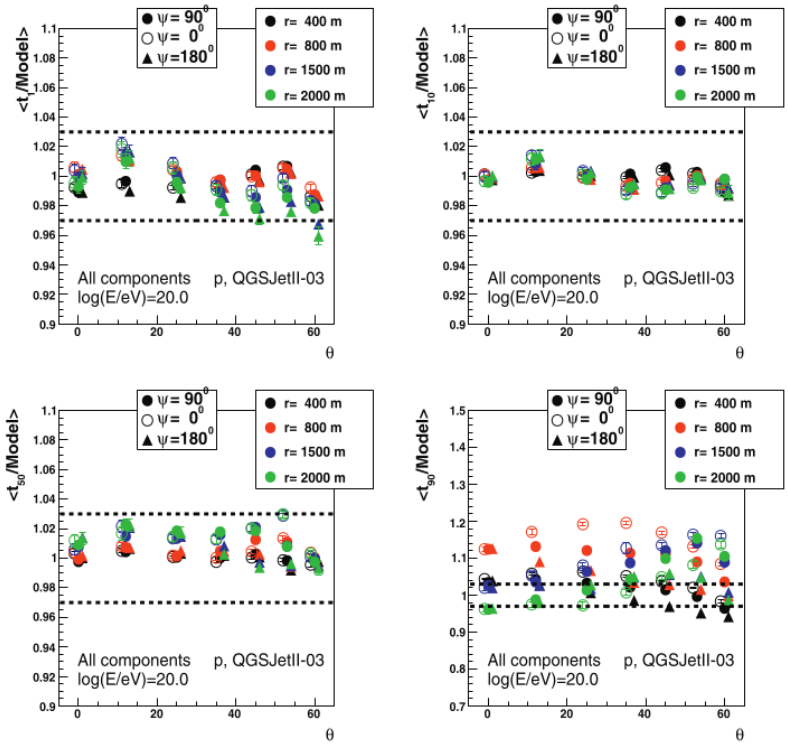

Figure 5.10: The average ratio of the simulated quantiles with respect to the model as function of the zenith angle, for different azimuths ϕ and distances r. The dashed lines in each panels indicate the ±3% deviations. From left to right and top to bottom: the ratio for the 1%, 10%, 50% and 90%. Taken from [132].

5.3 Validation of the model for photons simulations

5.3.1 Set of simulations

Throughout the work presented in this thesis, photon and proton MC simulations of extensive air showers are used. This section aims to describe both simulations sets before

beginning the analysis.

The characteristics of the photon and proton simulations are listed hereafter:

- Energy range: from $10^{18.5}$ eV to $10^{20.5}$ eV
- Energy spectral index: -1
- Zenith angle range: from 0° to 65°, uniformly distributed in $\cos^2(\theta)$
- Azimuth range Φ: from 0° to 360°, uniformly distributed in Φ
- Hadronic interaction model: EPOS-LHC
- Thinning: 10^{-6}
- shower simulated with: CORSIKA v77100
- Offline version : v3r99p1-icrc-2019

The simulations are produced with an energy spectrum following a power law E^{γ} of spectral index $\gamma = -1$. This is not the behaviour followed by the real flux of cosmic rays. Thus, the simulated spectra must be re-scaled to follow the real spectra behaviours, and each event must be re-weighted as function of its simulated energy. In case of protons, the expected spectral index γ is the one inferred from the combined-fit of the UHECRs spectrum [137] and $\gamma = -3$. For photons, the slope of the spectrum cannot be inferred from a fit on data. From the studies of UHECRs production at sources and photon propagation effects, the expected spectral index for photon at Earth is $\gamma = -2$ and is the one used frequently in literature. In the following, the simulated events will be always weighted to the realistic spectra.

5.3.2 Validation of the universality model for photon showers

The universality model was parameterised using proton-induced showers simulated with the hadronic interaction model QGSJetII-03 [63]. The use of universality in this work requires that the photon simulations are well described by the Signal and Time Models. To check that, the predicted values of the integrated signals and the risetimes in WCDs are compared to their values obtained from simulations. Only vertical simulated showers ($\theta_{MC} \leq 60°$) having a Gaisser-Hillas X_{max} not more than 150 g/cm^2 below ground are used (value from the fit of the longitudinal profile of the simulated shower, see Sec. 4.2.3). This is done to avoid non physical values of X_{max} and the muon content N_{μ} (this issue is discussed in Sec. 6.1.2). The model of universality is implemented in the Offline framework [87] of the Pierre Auger Collaboration and the predicted values discussed here are calculated as function of the simulated shower parameters from Eq. 5.10 and 5.4.

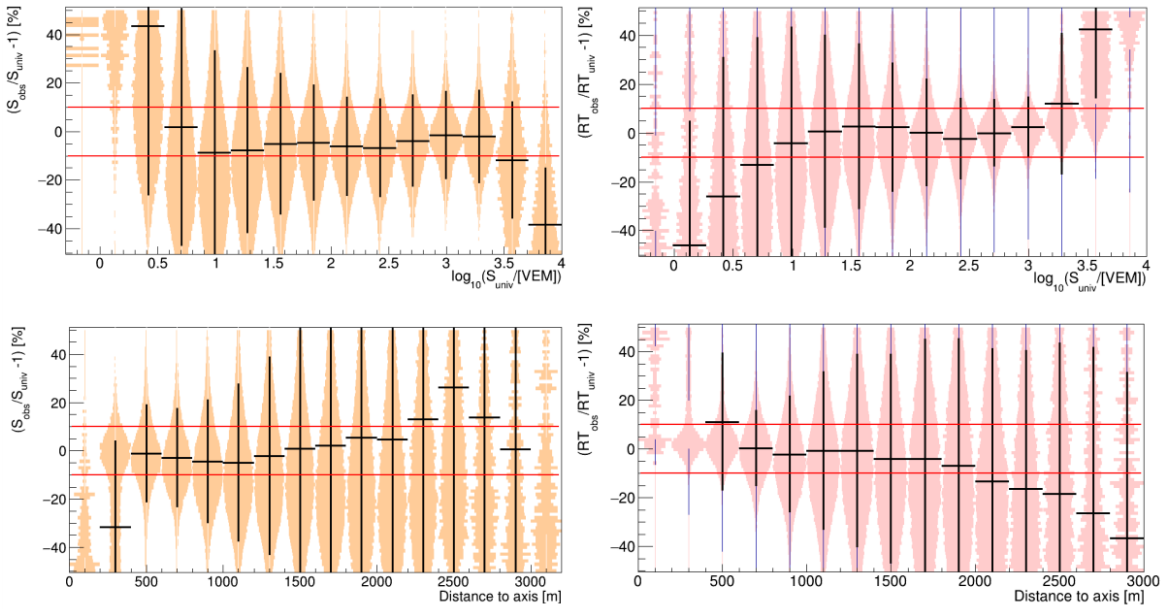

Figure 5.11: Left: Relative difference between the observed integrated signal in a station S_{MC} and the predicted signal from the universality model S_{univ}, as function of S_{univ} (top) and of the distance to the axis (bottom). Right: Relative difference between the observed $t_{1/2}$ RT_{obs} and the predicted $t_{1/2}$ from the universality model RT_{univ}, as function of S_{univ} (top) and of the distance to the axis (bottom).

On the left panels of Fig. 5.11, the relative difference in percentage of the Monte-Carlo integrated signal S_{MC} with respect to the prediction from universality S_{univ} (Eq. 5.14) is reported. It is drawn as function of S_{univ} and r_{MC}, the distance of the WCD to the axis of the simulated shower, at the top and bottom respectively. The distribution in each bin of $\log_{10}(S_{univ}/\mathrm{VEM})$ and r_{MC} is shown by the orange violin plot. The black profile represents the mean value in the bin and the respective standard deviation, while the red lines indicate the $\pm 10\%$ deviation from the prediction. On the right panel of Fig. 5.11, the results for the same study on the difference between the risetime simulated value $t_{1/2,MC}$ and prediction from universality $t_{1/2,univ}$ (Eq. 5.15), is reported with pink violin plots.

$$\frac{S_{MC}}{S_{univ}} - 1 \tag{5.14}$$

$$\frac{t_{1/2,MC}}{t_{1/2,univ}} - 1 \tag{5.15}$$

Fig. 5.11 highlights two main features. For stations with small values of predicted signal S_{univ}, below ~ 5 VEM, a positive bias in the relative difference of signals is caused by station trigger effects. This bias is greater than 10% and increases with decreasing S_{univ}, reaching 40% at 3 VEM. Small signals being produced in the stations at higher distances from the axis, this effect of triggers can also be seen for larger distances (bottom-left panel). On the contrary, saturation effects are observed at high values of S_{univ}, above ~ 1500 VEM, with a negative bias greater than 10% in absolute value, and therefore for stations very close to the axis. When the readout electronics is saturated, a part of the signal is not recorded, leading to an underestimation of the integrated signal. Of course,

these effects of trigger and saturation cause similar biases in case of the *Time Model* (see right panels of Fig. 5.11). Overall, the photon simulations are correctly described by the Signal and Time Models for stations within a range of predicted signals between ~ 5 VEM ($\log_{10}(5/\text{VEM}) \simeq 0.7$) and ~ 1500 VEM ($\log_{10}(1500/\text{VEM}) \simeq 3.2$), where the mean bias stays below $+10\%$ or above -10%.

The validation can also be performed on event-base by looking at the mean relative differences over the candidate stations of the integrated signals and risetimes. Only events with at least four candidate stations are used. It is indeed the number of stations required in the reconstruction presented in Sec. 6. The left panels of Fig 5.12 show the mean relative difference over the candidate stations of S_{MC} with respect to S_{univ}, as function of the logarithm of the MC energy E_{MC} (top) and zenith angle θ_{MC} (bottom). On the right panel of Fig. 5.12, an identical procedure is done for the risetime. We observe a good description of the simulations by both the Signal and Time models. The mean value of the relative difference, reported by the black horizontal line in each bin, stays within a 10% a bias on the whole range of energy and zenith covered by the simulated photon showers. In summary: the photon library is well described by the universality model and can be used in the design of an analysis to search for photons. Hence, the reconstruction of a several shower characteristics for photon-induced shower, based on this model, can be developed. Accordingly, the reconstruction of X_{max}, the energy and the core position is presented in the next chapter.

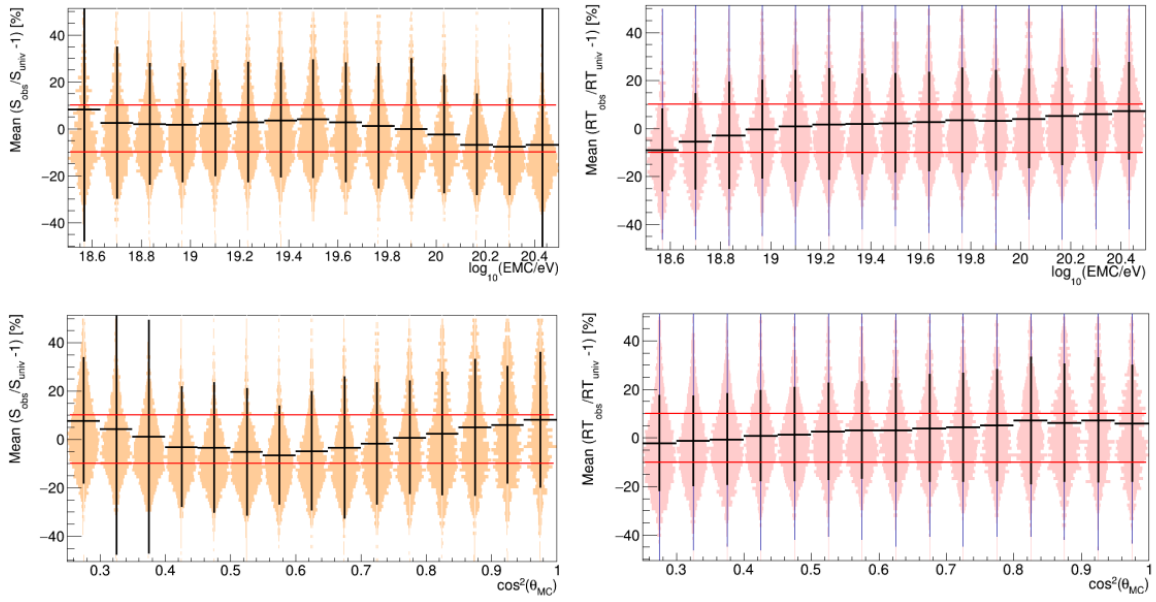

Figure 5.12: Left: Mean relative difference over the candidate stations between the observed integrated signal S_{MC} and the predicted signal from the universality model S_{univ}, as function of the MC energy (top) and of the MC zenith angle (bottom). Right: Mean relative difference over the candidate stations between the observed risetime, noted RT_{obs} on the figure, and the predicted risetime from the universality model, noted RT_{univ}, as function of the MC energy (top) and of the MC zenith angle (bottom).

Summary

In this chapter, the concept of air shower universality was presented. The studies performed on simulated showers highlighted that the energy spectrum, lateral and angular distributions of secondary electromagnetic particles shared an universal shape. The studies on the lateral profiles reported a dependence on the mass of the primary due to the charged pions, more numerous in nucleus-induced showers. This led to the introduction of the muonic component in the universality concept. The longitudinal profiles of muons also share universal behaviour.

The good understanding of universality allows to predict the distributions of secondary particles at ground: a model based on this concept was developed. This model predicts with good accuracy the value of the integrated signals in the WCDs as well as their shape, for the four shower components considered.

The model of universality is used in this thesis on photon MC simulations. Therefore, a validation has been done to check if the photon simulations are well described by the model. This is performed by looking at the relative differences of the simulated integrated signals and risetimes with respect to their predictions. We find that for predicted signal values between 5 VEM and 1500 VEM, the deviations stay within $\pm 10\%$ for the whole range of energy and zenith angle covered by the photon simulations.

Chapter 6

Reconstruction of photon showers with universality

Contents

Using the universality model detailed in the previous chapter and validated with photon simulations, the reconstruction of X_{max}, the slant depth of the shower maximum, can be designed for photon showers, alongside a reconstruction of the energy and core position (i.e. position of the impact of the shower core). The motivations to consider for this new reconstruction method are presented in this chapter and the procedure followed as well. Moreover, the optimisation of the fitting process in the determination of the shower parameters is discussed and the obtained results are presented.

6.1 Universality-based reconstruction of photon showers using SD data

Before the presentation of the universality-based reconstruction of photon showers, the terms, expressions and variables often used in this manuscript are introduced.

6.1.1 Terms and expressions

- X_{max}: the maximum depth of the shower development
  - $X_{max,GH}$: value obtained through the fit of the longitudinal profile of a simulated EAS with a Gaisser Hillas function (see Sec.4.2.3)
  - X^{γ}_{max}: value obtained with the photon showers reconstruction presented in this chapter
- E: primary energy
  - E_{MC}: Monte Carlo energy of the primary cosmic ray.
  - E_{had}: energy value obtained using the SD energy estimator, and the calibration based on hybrid data (Sec. 4.2.2), i.e. hadron-induced showers
  - E_{γ}: reconstructed photon energy obtained with the procedure described in this work, i.e. a calibration designed for photons
- θ: zenith angle of the EAS
  - θ_{MC}: Monte Carlo zenith angle
  - θ_{rec}: obtained by the standard SD reconstruction
- Shower plane (SP): perpendicular plane to the shower axis
- Preshowering photons: primary photons that convert into an electron/positron pair in the Earth atmosphere, resulting into a superposition of two (or more) less energetic air showers
- Core position: position of the impact on ground of the shower core

6.1.2 Motivations and principle of the reconstruction

As mentioned before (Sec. 4.3), X_{max} is an observable highly sensitive to the primary mass. For hybrid data, X_{max} is determined with the fit of the longitudinal profile measured by the FD with a Gailler Hillas function (see Sec. 4.2.3). The analysis searching for photons between 10^{18} eV and 10^{19} eV in the hybrid data set [71] (see Sec. 4.4.2) uses the measured X_{max} as the main separation variable, coupled with the muon content obtained with universality. When using the data recorded by the SD only, the search analysis has to rely on the deviation of photon-induced showers with respect to the the bulk of data. For photon-nuclei discrimination purposes, using only the SD data set, a reconstruction of X_{max} for photon showers based on the universality model, could be a way to improve the search performances.

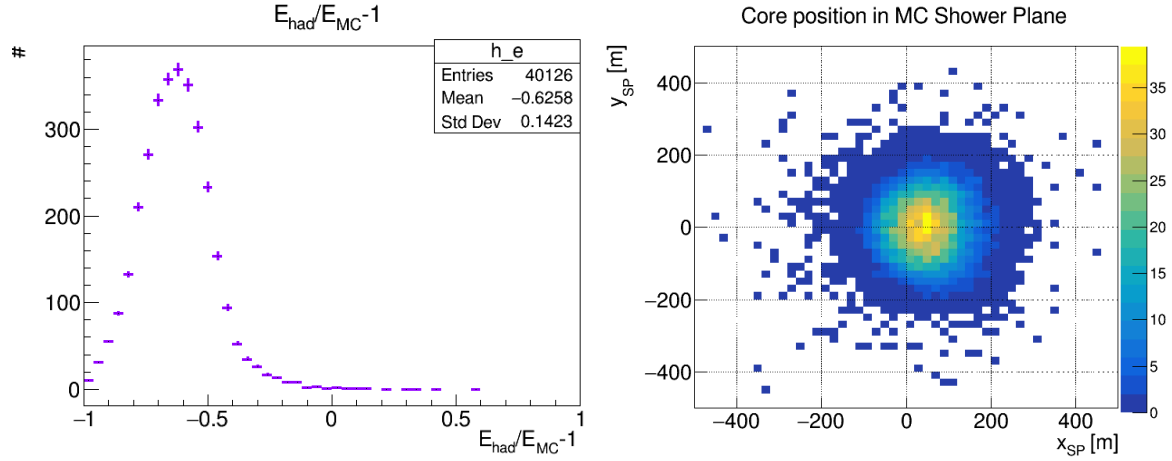

Figure 6.1: Left: Energy bias of the standard reconstructed SD energy for non-preshower photon simulations with $\theta_{MC} = 60°$. Right: standard SD reconstructed core position in the MC shower plane for non-preshower photon simulations under $\theta_{MC} = 60°$. One can see the shift in the earlier part of the shower on the x_{SP} axis.

Currently, the energy reconstruction of extensive air showers detected by the SD is done using the shower size S_{1000}, corresponding to the expected signal at 1000 m from the axis, as explained in Sec. 4.2.2. This energy estimator is determined after the fit of the LDF which parameterisation is optimised for data (hadron induced showers): the LDF does not properly fit the lateral distribution of the signals for photon showers, which is steeper (Sec. 4.2.2). The energy assigned to photon-induced showers, named E_{had} hereafter, is thus underestimated by about -62%. The energy bias $E_{had}/E_{MC} - 1$ distribution is reported in the left panel of Fig. 6.1 for simulated non-preshowering photon showers with zenith angles below 60° and MC energies ranging from $10^{18.5}$ eV to $10^{20.5}$ eV. With the method used to estimate the photon energy in [32] (see Sec. 4.4.1) the obtained energy resolution is $\simeq 30\%$ for non-preshowering photons and the bias is of $\simeq -30\%$ for preshowering photons. An universality-based reconstruction is expected to improve the reconstructed photon energy since it is one of the model parameters which can be derived from the process.

The principle of universality of extensive air showers states that the average properties of a shower can be described by only three parameters: the primary energy, the muon content N_μ and the maximum depth of the shower X_{max} (see Sec. 5.1). The goal of this work is to design a new SD reconstruction for photon-induced showers based on this principle to access the photon energy and X_{max}. To do so, we use an approach inspired from a preliminary study done by M. Ave [138]. In this study, to be able to use the couple of discriminant observables (X_{max}, N_μ) that cannot be measured directly, N_μ is fixed to its mean value obtained from photon simulations. Then, the X_{max} and the energy of photon-induced air showers are reconstructed using a maximum likelihood-method for the fit of the parameters. Encouraging results for the photon search showing the X_{max} distributions of photons and other simulated primaries, were presented. However, the lack of statistics in the set of simulations (discontinuous spectra of MC energy and zenith angle) limited the conclusions of this preliminary analysis. But according to that preliminary study, by fixing N_μ to the mean value of photon simulations, the model of universality will re-

produce the average behaviour of a photon and the reconstruction is designed for photons.

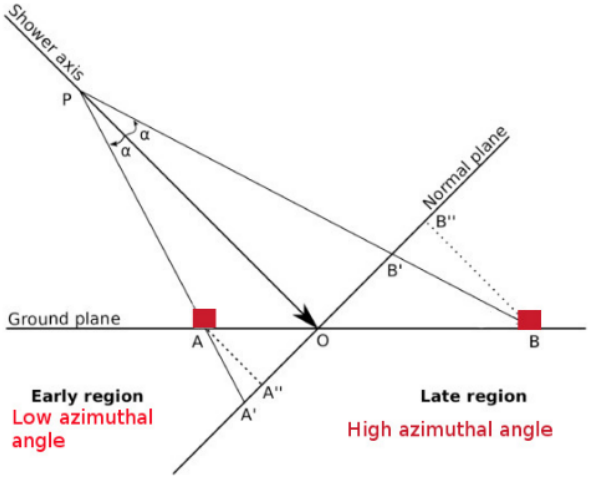

Figure 6.2: Scheme of the azimuthal asymmetry of stations. The stations with lower angles ϕ receive particles from a earlier stage of development while stations with higher angles receive particles from a later stage. The stations are depicted in red and the core position corresponds the O point.

Alongside the energy and X_{max} reconstruction, the core position is to be reconstructed. In the standard SD reconstruction, the asymmetry related to the azimuth angle ϕ[1] of the stations is not taken into account. As illustrated in Fig. 6.2, a WCD with a low azimuth angle will detect particles from a earlier stage than one at higher azimuth. The core position is then shifted towards the earlier part of the shower. The x_{SP} axis corresponds to the projection of the shower axis on the perpendicular shower plane (SP). On the right of Fig. 6.1, one can see the standard SD reconstruction of the core position in the Monte-Carlo shower plane where the shift of 50 m towards the earlier part of the shower development is visible. In the universality model developed for the SD stations [135] [132], ϕ is a parameter of the functions predicting the signals (see Sec. 5.2 and 5.3), and therefore the asymmetry is accounted for. Thus, the core position is also reconstructed using universality.

6.1.3 Validation of the universality-based reconstruction strategy

As shown in Sec. 4.1.1, the number of muons coupled with X_{max} ensures a very distinct discrimination between photons and nuclei primaries. In the universality model, the muon content of a shower, N_μ, is defined as the ratio of the muonic signal at 1000 m from the shower axis with respect to proton-induced showers simulated with the hadronic interaction model QGSJetII-03. However, N_μ is not observable and we are only able to access it through simulations. The computation of N_μ is done using the universality prediction

[1]angle between the projection of the shower axis on the shower plane and the position of the station in the shower plane

of the integrated signals (Sec. 5.2.1) and the muon component of the simulated signals recorded by the 12 "dense stations". These stations correspond to a ring of 12 virtual simulated stations at 1000 m from the shower axis in the shower plane. On Fig 6.3, the ring of 12 dense stations is reported in grey for one of the photon simulations. With these stations, N_μ is computed as the average value of the ratio between the true muonic signal in the station, S^i_μ, and the muonic signal predicted by the universality model for QGSJetII-03 protons $S^i_{\mu,ref}$. The formula for the computation of N_μ is in Eq. 6.1, and takes into account both the nature of the primary and the hadronic interaction model. This last point is important. As the reference signal stays unchanged (QGSJetII-03 protons), all masses and hadronic interaction models can be described by the universality model with the use of N_μ.

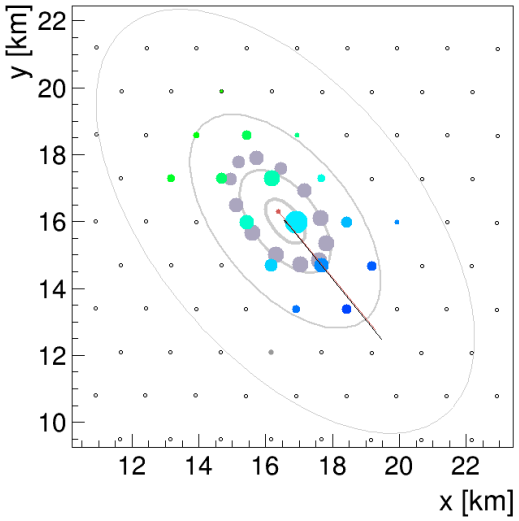

Figure 6.3: Footprint of a photon simulated showers on the SD-1500 network, with the ring of the 12 dense stations reported in grey.

$$N_\mu = \frac{1}{12}\sum_{i=1}^{12}\frac{S^i_\mu}{S^i_{\mu,ref}(N_\mu = 1)} \tag{6.1}$$

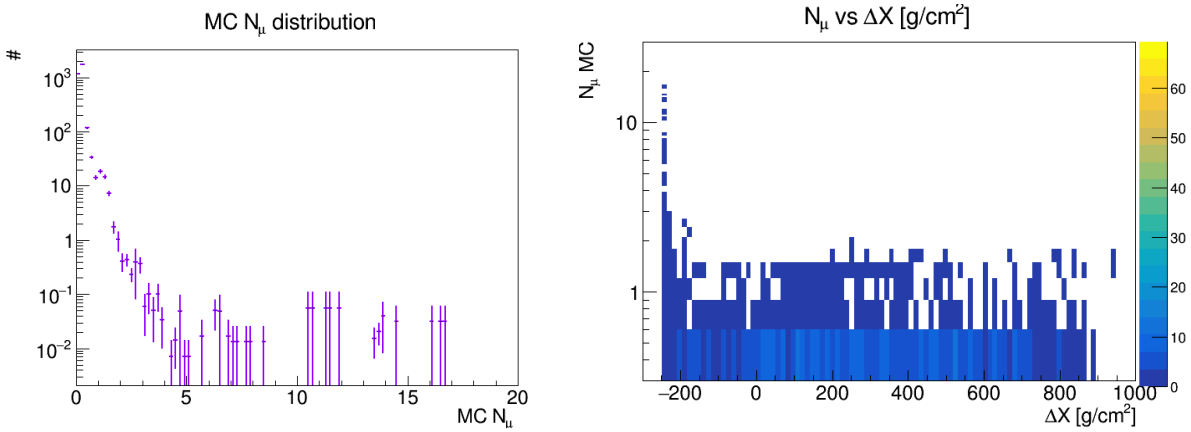

Figure 6.4: Left: N_μ weighted distribution in log-scale computed with the photon simulations with a MC zenith angle below $\theta_{MC} = 60°$. Right: N_μ as function of ΔX [g/cm^2]. Negative values of ΔX means that the Gaisser-Hillas X_{max} is under ground level.

The N_μ distribution for all photon simulations with zenith angle below $\theta_{MC} = 60°$ is reported in log-scale on the left panel of Fig. 6.4. A visible tail in the distribution is reaching values up to almost 20. It is caused by a few events with a Gaisser-Hillas X_{max} well under ground level, below $\sim$ 150 g/cm^2. The Gaisser-Hillas X_{max}, noted $X_{max,GH}$ is obtained from the simulations by fitting the generated shower longitudinal profile with the Gaisser-Hillas function presented in Sec. 4.2.3. For showers which would have reached their maximum below ground, the fitted $X_{max,GH}$ is thus an extrapolation, and results in some cases in a very likely non-physical value. The muon content being calculated from the Signal model with X_{max} as an input parameter is therefore also wrong. This behaviour can be seen in the right panel of Fig. 6.4 in which N_μ is drawn as function of $\Delta X = X_{ground} - X_{max,GH}$, corresponding to the difference in depth between the ground level and $X_{max,GH}$. Showers with a negative value of ΔX have a fitted $X_{max,GH}$ under ground. The tail, starting at $\Delta X \simeq -150$ g/cm^2, does not affect the mean value of N_μ needed for the photon reconstruction by dragging it to higher values. Finally, the N_μ weighted distribution for events with $\Delta X > -150$ g/cm^2 is shown in Fig. 6.5, and the mean value for photon simulations is $< N_\mu >_\gamma = 0.25$, with a standard deviation of 0.15.

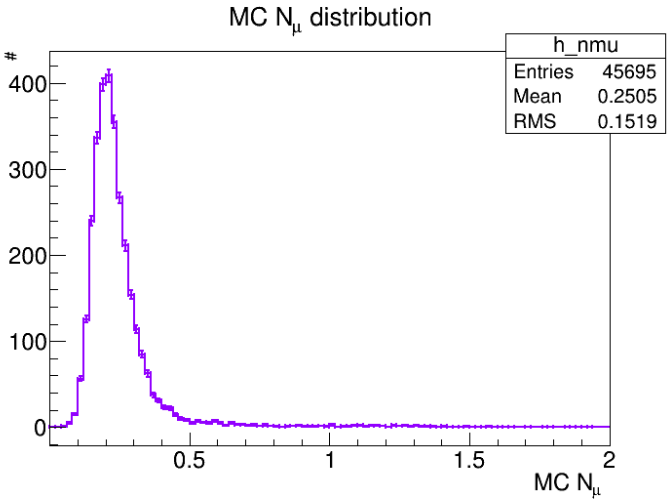

Figure 6.5: N_μ weighted distribution computed with the photon simulations below $\theta_{MC} = 60°$ and $\Delta X > -150$ g/cm^2.

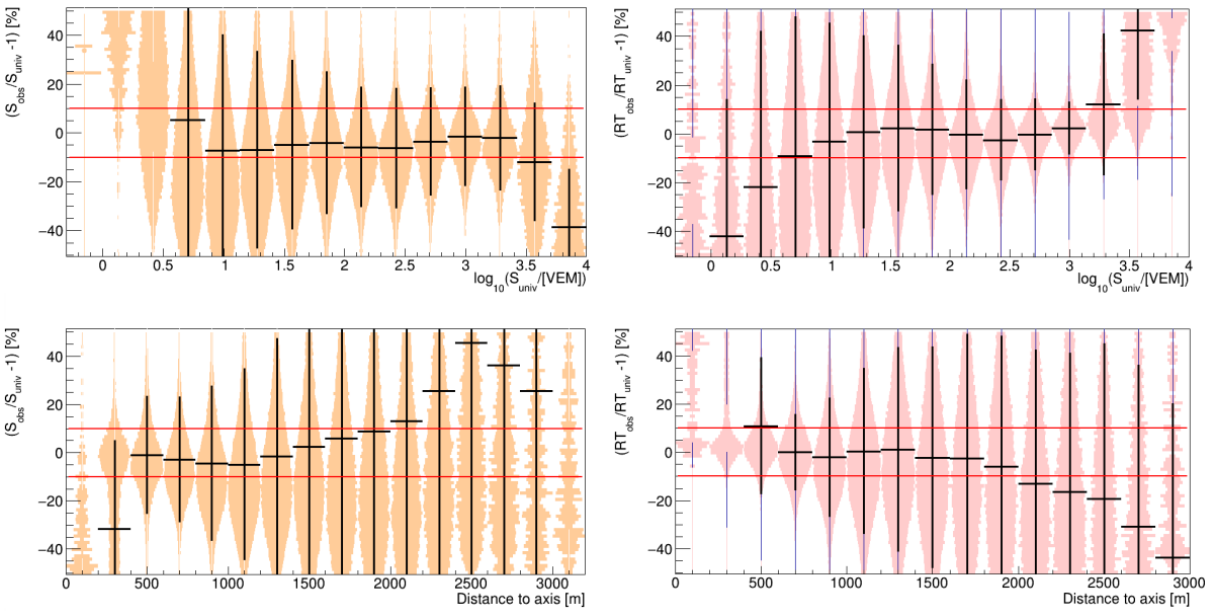

Figure 6.6: Validation tests performed on photon simulations to verify if the use of $< N_\mu >_\gamma$ in the universality model is feasible. Left: Relative difference between the observed integrated signal in a station S_{MC} and the predicted signal from the universality model S_{univ}, as a function of S_{univ} (top) and of the distance of the station to the axis (bottom). Right: Relative difference between the observed $t_{1/2}$ RT$_{obs}$ and the predicted $t_{1/2}$ from the universality model RT$_{univ}$, as a function of S_{univ} (top) and of the distance to the axis (bottom).

The validation of the universality model with the true shower muon content has been done in Sec. 5.3. In the designed reconstruction method, N_μ is fixed to $< N_\mu >_\gamma$ so that the model reproduces the average behaviour of photon-induced showers. Thus, an additional validation is required to verify that the simulations are well described by the universality model when the muon content is fixed to the mean value $< N_\mu >_\gamma$. The calculation of the biases defined in Eq. 5.14 and 5.15 and shown in Fig. 5.11, are reproduced

by substituting the value of N_μ, calculated for each shower as in Eq. 6.1, to $< N_\mu >_\gamma$. The results are reported in Fig. 6.6. The observations drawn in the first validation in Sec. 5.3.2 with the individual N_μ of each shower remain identical. The model describes correctly the average behaviour of simulations within a certain range of predicted signal and distance where the trigger and saturation effects are less probable. The mean relative difference over the candidate stations, as function of the Monte-Carlo energy and zenith angle are shown in Fig. 6.7. Because we chose to fix the muon content of each shower to $< N_\mu >_\gamma$, we observe an increase of the standard deviation in each bin of about +10%. Nevertheless, the photon simulated showers remain well described by the universality model for the whole range of energy and zenith covered by these simulations, and we can use the universality model to build a photon reconstruction strategy.

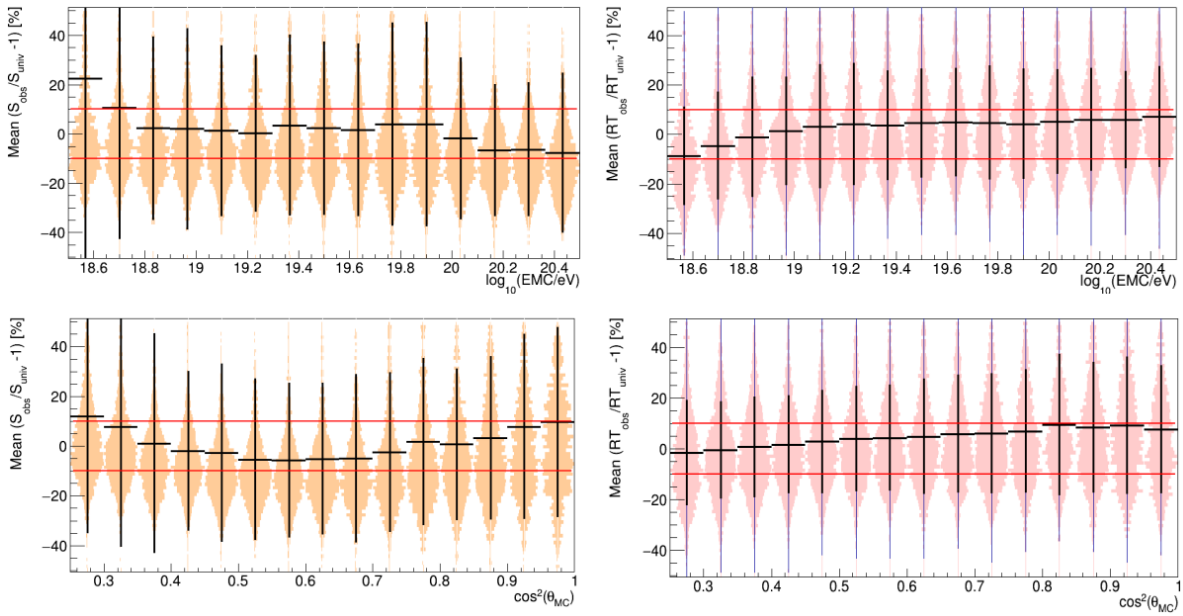

Figure 6.7: Validation tests performed on photon simulations to verify if the use of $< N_\mu >_\gamma$ in the universality model is feasible. Left: Mean relative difference over the candidate stations between the observed integrated signal S_{MC} and the predicted signal from the universality model S_{univ}, as a function of the MC energy (top) and of the MC zenith angle (bottom). Right: Mean relative difference over the candidate stations between the observed $t_{1/2}$, RT_{obs}, and the predicted $t_{1/2}$ from the universality model, RT_{univ}, as a function of S_{univ} (top) and of the MC energy (top) and of the MC zenith angle (bottom).

6.1.4 Selection of stations

To ensure a good reconstruction of photon-induced showers, it is necessary to perform a station selection. As seen in Sec. 5.3 and 6.1.3 in which the validation of the universality model [135] [132] with the simulations was presented, trigger and saturation effects create important biases for the signals and risetimes for predicted signals below $\sim$ 5 VEM and above $\sim$ 1500 VEM.

To avoid using stations with large biases, we will not use low gain saturated stations.

Only stations with measured signals above 5 VEM are used to prevent trigger effects occurring for low signals. This selection is done prior to the reconstruction. As the validation of the model demonstrated that predicted signals below the 5 VEM threshold should not be used, this selection cut is also implemented but cannot be done prior to the reconstruction. Indeed, the prediction of universality given by Eq. 5.4 and 5.10 is dependant on showers parameters that will be reconstructed with a maximisation likelihood method (see following sections). This means that the predicted signal value varies during the reconstruction as function of the reconstructed parameters. Therefore, the selection of stations based on the predicted signal is directly performed in the likelihood functions (Sec. 6.3). The station cannot be properly cut out of the likelihood function. Indeed, the maximised function is the sum of the individual stations likelihoods. Removing stations as function of the reconstructed parameter value will cause problem as the number of degrees of freedom will depend on the parameter value as well. This is solved by assigning a very low likelihood value of -200 in logarithm to the stations falling below the 5 VEM threshold.

6.2 Procedure of the photon reconstruction

In this section, we define the reconstruction procedure of X_{max}, the primary energy E_γ and the core position (x_c, y_c) for photon induced-showers. These parameters are estimated by a maximisation of the likelihood functions presented in Sec. 6.3. The procedure is divided in four steps in which the parameters are reconstructed one after the other. During the whole procedure, the muon content is fixed to $< N_\mu >_\gamma$ for the reasons explained previously. The arrival direction is kept to the value obtained from the standard SD event reconstruction (Sec. 4.2.2) which provides an angular resolution ranging from 1.6° to 0.9° depending on the number of stations used. To ensure a good reconstruction, only events with at least four stations passing the station selection are reconstructed. We initially consider only the reconstruction of non-preshowering photon showers. The case of preshowering photons is discussed later (Sec. 6.2.2).

6.2.1 Reconstruction of non-preshowering photons

The different steps of the designed reconstruction procedure are summarised on Fig. 6.8. The first step of the reconstruction is the estimation of the photon energy. As in the standard SD reconstruction in which the energy is estimated from the fit of the lateral profile of the shower, the LDF is fitted using the universality Signal Model which predicts the integrated signal in each station. Then, the core position is also reconstructed using the signal part of the model, while the energy is fixed to the reconstructed one. The core position is necessary when calculating the distance between a station and the shower axis. Therefore, a change in the core position affects the distances of the WCD and by implication the LDF. The third step consists in a second reconstruction of the energy, identical to the first step but with the new core position. The reconstruction of the energy with the unbiased reconstructed core position is meant to improve the photon energy resolution.

Finally, the reconstruction of $X_{\max}$ is performed by fitting the stations risetimes, using the time part of the model described in Sec. 5.2.2.

Steps :	1	2	3	4
Energy	**Reconstructed** : **Start** = median of Ehad/EMC (θ,S1000) **Range** = 10%-90% quantiles	**Fixed** to reconstructed value from step 1	**Reconstructed** : **Start** = reconstructed value from step 1 **Range** : 2/3 of range in step 1	**Fixed** to reconstructed value from step 3
Core	**Fixed** to standard SD reconstruction + corrected for the asymmetry as function of $\cos^2\theta$	**Reconstructed** : **Start** = standard SD reconstrcution + corrected for the asymmetry **Range** = radius of 200m from start value	**Fixed** to reconstructed value from step 2	**Fixed** to reconstructed value from step 2
Xmax	Using **<Xmax>(E)** for photons	**Fixed** to **<Xmax>(E)** for the reconstructed energy is step 1	Using **<Xmax>(E)** for photons	**Reconstructed** : **Start** = <Xmax>(E) for the reconstructed energy in step 3 **Range** = no bounds

Figure 6.8: Table summarising the four steps of the reconstruction procedure.

Values of fixed parameters

During each step of the procedure, the parameters not used in the likelihood maximisation process must be fixed to given values. In the first step, the core position is fixed to its standard SD reconstruction but should be corrected for the azimuthal asymmetry. Fig. 6.9 shows the SD reconstructed core position in the simulated shower plane in three bins of MC energy, E_{MC}, and five bins of zenith angle, θ_{MC}. The shift towards the earlier part of the shower, visible in each bin, is as expected more important for more inclined showers. The mean shift on the x_{SP} axis as function of $\cos^2(\theta_{MC})$ is drawn on Fig. 6.10, for the same three bins of MC energy than those in Fig. 6.9. The dependence with the zenith angle is clear, the shift ranges from $\sim$ 10 m between 0° and 25°, to $\sim$ 100 m around 55°. On the other hand, the variation with the energy is negligible. The correction applied on the core position thus depends only on the zenith angle. The shift for all energies as function of $\cos^2(\theta_{MC})$ is reported in Fig. 6.11 and the core position is corrected as function of the zenith using these values.

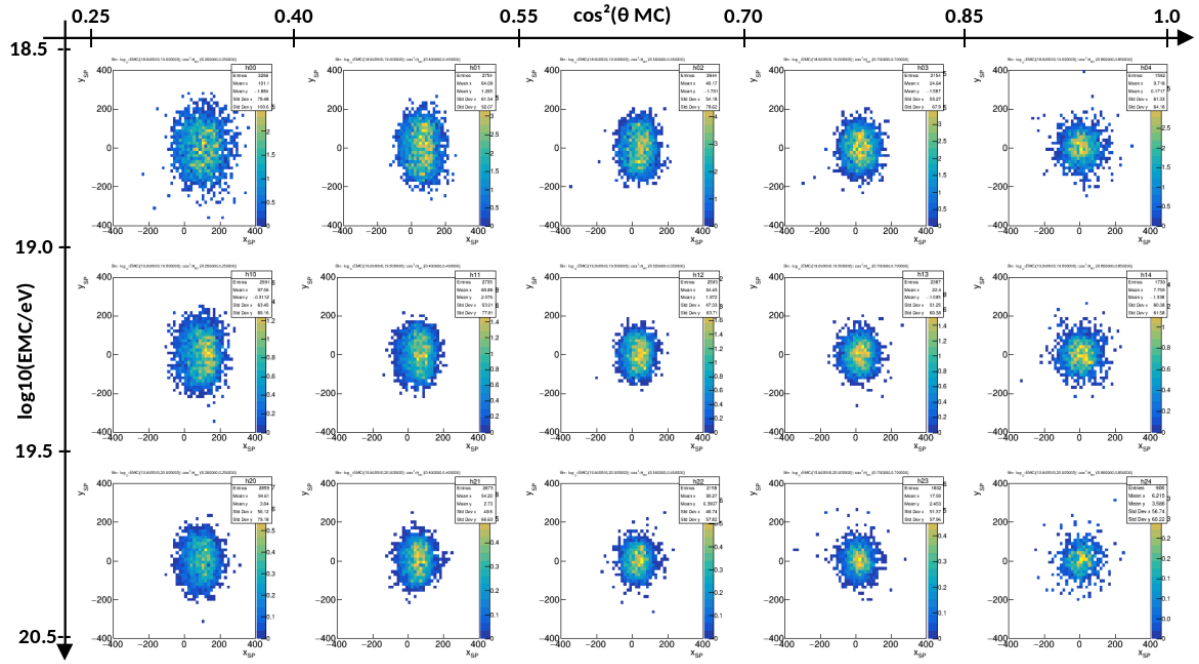

Figure 6.9: The reconstructed SD core position in the Monte-Carlo shower plane in five bins of MC zenith angle θ_{MC} and three bins of MC energy. The shift towards the early part of the shower is visible and growing with increasing zenith angle.

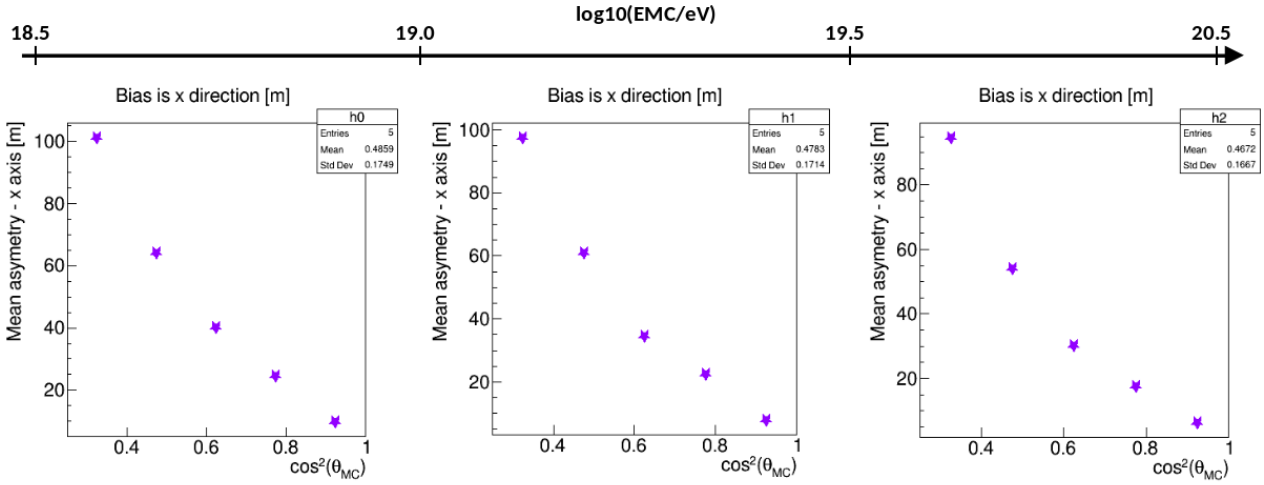

Figure 6.10: The mean shift of the SD reconstructed core position in the MC shower plane towards the earlier part of the shower. Each panel corresponds to a bin of MC energy and the bias is plotted as function of five bins of $\cos^2(\theta_{MC})$.

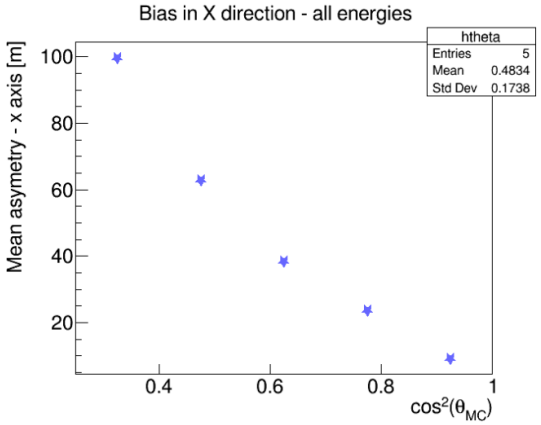

Figure 6.11: The mean shift of the SD reconstructed core position in the MC shower plane towards the earlier part of the shower as function of the MC zenith angle, for all MC energies.

The maximum depth of the shower development is estimated in the last stage of the procedure. Therefore, during the reconstruction of the core position and the photon energy, a value X_{max} has to be determined. As shown in Fig. 4.15, X_{max} increases along with the energy. Thus, during the reconstruction of the photon energy (first and third steps), the given X_{max} value varies as function of the energy and is equal to its mean value for this energy, noted $< X_{max} >_{\gamma} (E)$. The corresponding values of $< X_{max} >_{\gamma} (E)$ are taken from Fig. 4.15 [120]. A distinction between preshowering photons and non-preshowering photons has to be made as preshowering photons develop higher in the atmosphere. Thus, the special case of preshower photons is discussed in Sec. 6.2.2.

Start values of the parameters

The core position corrected for the azimuthal asymmetry is also used as the start value prior to the minimisation for the core reconstruction (see Fig. 6.8). The $< X_{max} >_{\gamma} (E)$ for photon-induced shower as function of the energy is also the start value chosen before the estimation of X_{max}. For the photon energy, the start value is taken from a look-up table built with the simulated photon showers. In this table, divided in bins of $\sec(\theta_{MC})$ and $\log_{10}(S_{1000}/\mathrm{VEM})$, is reported the median of E_{had}/E_{MC} for non-preshowering photons. As the standard SD reconstructed energy E_{had} is an under-estimation of the true primary energy, it is not optimal to use it as a start value for the minimisation. Therefore, the photon energy is set to the value from the table, multiplied by E_{had}, to overcome this issue. This process is only done in the first step of the reconstruction. In the second estimation of the energy, corresponding to the third step of Fig. 6.8, the previous reconstructed energy is used as start value. The table was built with showers having a MC zenith angle below 60°, with at least 4 stations (the minimum number of stations required in the procedure). Only simulations with E_{had}>$10^{18.5}$ eV are selected to match the selection of the SD photon search analysis published in [32].

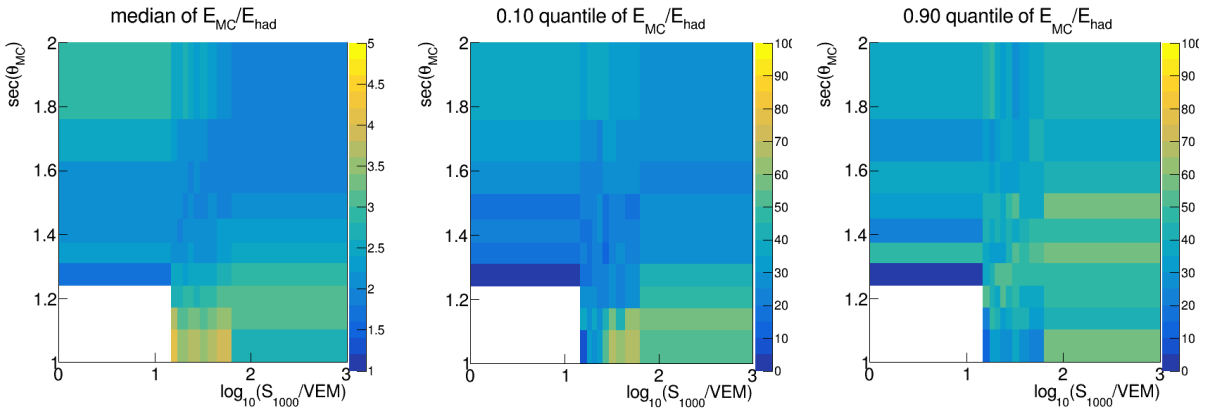

Figure 6.12: Left: median of the distribution of E_{MC}/E_{had} for non-preshowering photon simulations in bins of $\log_{10}(S_{1000}/\text{VEM})$ and $\sec(\theta_{MC})$. Middle: relative difference in percentage of the 10% quantile with respect to the median. Right: relative difference in percentage of the 90% quantile with respect to the median.

Allowed parameter range for the reconstruction

The range of parameters allowed can be restricted during the minimisation to avoid reaching non-physical values or local minima. In the procedure, the core position is restricted to be within a 200 m radius from the start value, which is coherent with the right panel of Fig. 6.1 as it corresponds to about 3 standard deviations of the distribution. Concerning the photon energy, the limits are set with the 10% and 90% quantiles of the E_{MC}/E_{had} distributions in bins of $\log_{10}(S_{1000}/\text{VEM})$ and $\sec(\theta_{MC})$. The relative differences in percentage between the quantiles and the median are shown in the middle and right panels of Fig. 6.12, for the 10% and 90% quantiles respectively. In the second reconstruction of the energy, since this step in mainly an adjustment rather than a new reconstruction, the range is restricted to 2/3 of the initial one, as we don't expect a drastic change of the reconstructed energy value.

6.2.2 The case of preshowering photons

In the case of preshowering photons, X_{max} is on average smaller than non-preshowering ones and their energy scale is also different.

Hence, a separate reconstruction for photons undergoing preshowering was developed. The procedure stays identical but another look-up table is used for the assignment of the start value of the energy, and the 10% and 90% quantiles used to determine the range of reconstruction are built using the simulated showers corresponding to preshowering photons. In Fig. 6.13, the look-up table (median of E_{had}/E_{MC}) and the corresponding quantiles in bins of the shower size S_{1000} and MC zenith angle are shown. As for Fig. 6.12, only events with zenith angles below 60°, with at least 4 stations and $E_{had} > 10^{18.5}$ eV are used. Similarly, the mean X_{max} as function of the photon energy, $< X_{max} > (E_\gamma)$, is still taken from Fig. 4.15 [120] but for the case of preshowering photons (blue stars).

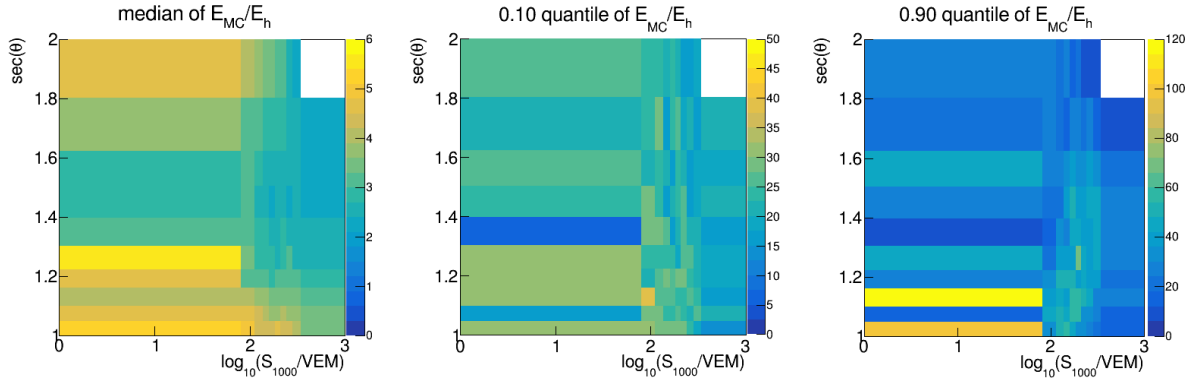

Figure 6.13: Left: median of the distribution of E_{had}/E_{MC} for preshowering photon simulations in bins of $\log_{10}(S_{1000}/\text{VEM})$ and $\sec(\theta_{MC})$. Middle: relative difference in percentage of the 10% quantile with respect to the median. Right: relative difference in percentage of the 90% quantile with respect to the median.

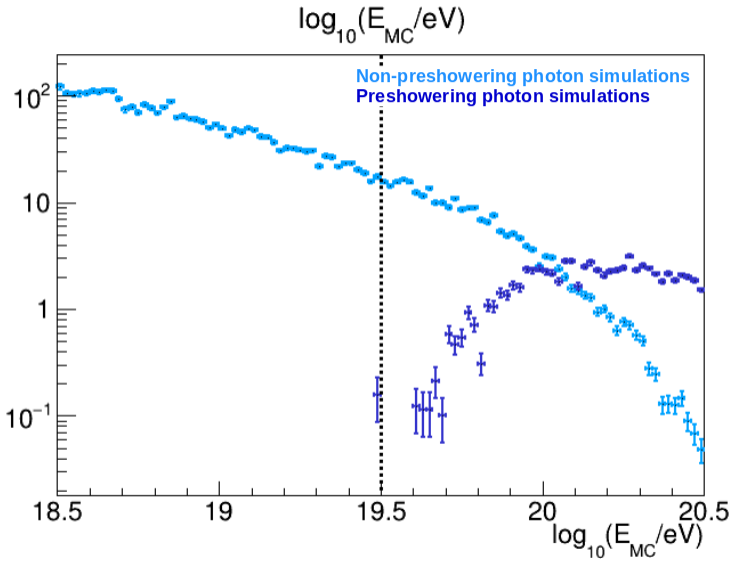

Figure 6.14: Monte Carlo energy distribution of non-preshower simulated photon showers (light blue) and preshower photon shower (dark blue) below $\theta_{MC} = 60°$. The vertical line indicates the energy threshold chosen to identify preshower events in the designed reconstruction.

Two separate photon reconstructions are thus possible. By implementing a second reconstruction designed for preshowering photons, we expect to reduce the energy bias observed in the SD search analysis [32]. To identify if the reconstructed event corresponds to a preshowering photon or not, it is necessary to define a specific and efficient criteria. This is done by comparing the likelihood values (see Sec.6.3) obtained at the end of both reconstructions. Since, the preshowering effect only occurs for photons with energy above $\sim 10^{19.5}$ eV at the Auger site (Fig. 6.14), the reconstruction is first performed in the case of non-preshowering photons: if the reconstructed photon energy is below $10^{19.5}$ eV, the event is flagged as non-preshower. If it is not the case, the second reconstruction in the preshowering hypothesis is performed and the two obtained likelihood values are com-

pared. The percentage of non-preshowering (preshowering) photons wrongly identified is $\sim 16\%$ ($\sim 24\%$).

6.3 Likelihood functions for the maximisation

In each step of the reconstruction procedure, the reconstructed parameter is obtained by a maximisation of the likelihood functions. The energy and core position of photon showers are reconstructed using the part of the universality model describing the integrated signal in the stations [135], while X_{max} is reconstructed with the Time model [132] only. The Universality provides us the mean value of signal and risetime in the stations. However, the variation around these mean values are described by the probability density functions (PDF) used in the maximised likelihood function, and the determination of these PDFs is presented in this section. It is important to note that the functions presented in the following are designed for stations. On the other hand, the logarithm of the likelihood function (log-likelihood or logL) maximised in the reconstruction of the shower parameters is the sum of the log-likelihood functions of the individual selected stations.

The minimisation of -logL is performed using the TMinuit [139] package included in ROOT [140] using MIGRAD.

6.3.1 Designed PDF for each station signal

The PDF of the signal of individual stations must describe the variations of the signal around the mean given by the universality model. As explained in Sec. 4.2.1, a vertical going-through muon deposits a signal of 1 VEM in the station. In a first attempt to determine the most appropriate function for the minimisation procedure, we considered that all the particles creating the integrated signal, S_{tot}, are muons. To convert the signal in a number of particles we assume that each of these muons generates 1 VEM, giving $< S_\mu >= 1$ VEM. Therefore, we chose a Gaussian PDF of mean m equals to the universality prediction of the signal S_{univ}. The related uncertainty σ is $\sqrt{S_{univ} \times < S_\mu >}$. Finally, the PDF function for the station signal is written in Eq. 6.2, in which S_{obs} is the measured signal in the WCD.

$$G(S_{obs}|m = S_{univ}, \sigma = \sqrt{S_{univ} < S_\mu >}) \tag{6.2}$$

To verify if the choice of this PDF leads to a good description of the variations of the signal, several tests are carried. They consist in reconstructing the energy while the core position and the direction of the shower are fixed to their true Monte Carlo values, and X_{max} to $X_{max,GH}$. The tests are carried using only simulated photon showers with a zenith angle below $\theta_{MC} < 60°$. Also, to avoid non-physical values of the Gaisser-Hillas X_{max}, event with $X_{max,GH}$ more than 150 g/cm^2 under ground level are rejected.

Fig. 6.15 shows the energy bias, defined as $E_\gamma/E_{MC} - 1$, where E_γ is the reconstructed photon energy, resulting from the use of Eq. 6.2 in the minimisation process (red). We

observe a bias of 3.3% with a resolution of 32% in the case of non-preshowering photons, and a bias of -3.1% with a 15% resolution for preshowering photons.

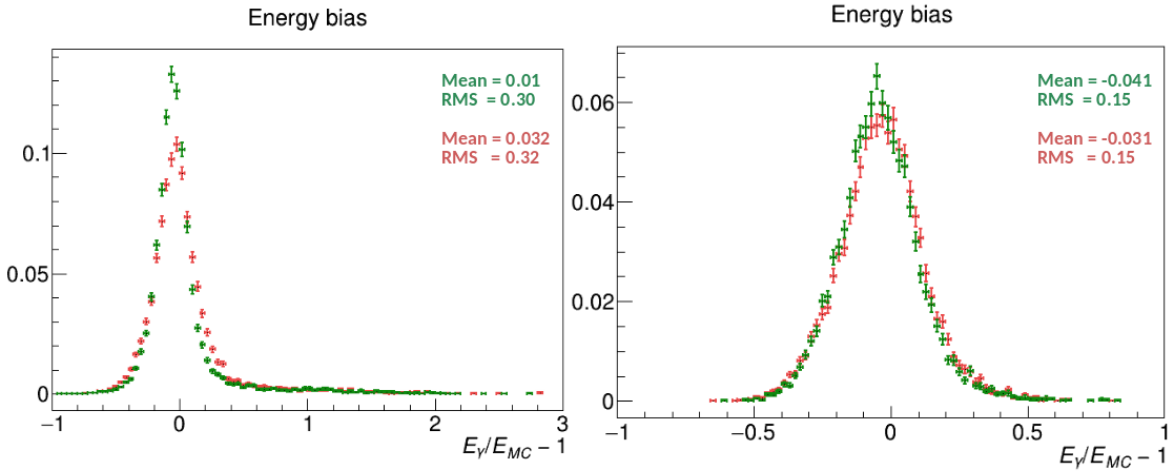

Figure 6.15: Distributions of the reconstructed photon energy bias resulting from Eq. 6.2 in red and from Eq. 6.3 in green. Only events having $\theta_{MC} < 60°$ and with a Gaisser-Hillas X_{max} not more than 150 g/cm^2 under the ground level are used. The distributions are normalised such that their integral is equal to 1. Left: the distributions are reported for simulated non-preshowering photons. Right: the distributions are reported for simulated preshower photons.

Although the assumption on the signal being only generated by muons seems like a rather good description, the implementation of the signal part carried by electromagnetic particles has to be considered for a more realistic one. The signal is divided into two components: muonic and electromagnetic. Each is described by a Gaussian, as previously, but each function is weighted with their respective contribution to the predicted signal, $\alpha_\mu = S^\mu_{univ}/S_{univ}$ and $\alpha_{EM} = S^{EM}_{univ}/S_{univ}$ for the muonic and the electromagnetic component respectively. Here, S^μ_{univ} is the signal predicted by the model for the pure muonic component, and S^{EM}_{univ} is the sum of the predicted signals from the three other components (pure electromagnetic, electromagnetic from muons and electromagnetic from low energy hadrons), i.e. $\alpha_{EM} = 1 - \alpha_\mu$. The PDF function for individual stations is thus expressed by Eq. 6.3.

$$\alpha_\mu G(S_{obs}\alpha_\mu | m = S^\mu_{univ}, \sigma = \sqrt{S^\mu_{univ} < S_\mu >}) + (1-\alpha_\mu) G(S_{obs}(1-\alpha_\mu) | m = S^{EM}_{univ}, \sigma = \sqrt{S^{EM}_{univ} < S_{EM} >}) \quad (6.3)$$

The addition of the electromagnetic part to the station likelihood function requires the estimation of $< S_{EM} >$, the average signal per electromagnetic particle which is necessary to determine the standard deviation of the corresponding Gaussian, as in Eq. 6.2 for the muonic part. $< S_{EM} >$ is obtained from photon simulations. For each event with θ_{MC} below 60° and each candidate station, the measured signal generated by electrons and photons, is divided by the corresponding number of particles entering the WCD. The distribution of the electromagnetic signal per particle is reported in Fig. 6.16. We find

$< S_{EM} >= 0.017$ VEM, which means that on average, 1 VEM represents about 60 photons/electrons.

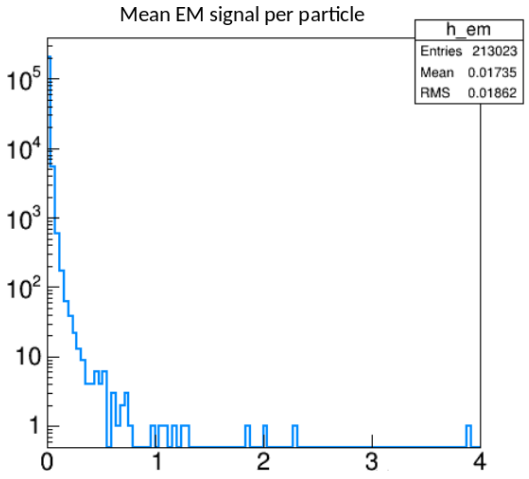

Figure 6.16: The mean electromagnetic signal of stations. The mean of the distribution (0.017) is used in the likelihood function.

The reconstruction test is repeated for this new PDF function given by Eq. 6.3. The results are displayed in Fig. 6.15 by the green distributions. For non-preshowering photons (left), the improvement is rather visible with a more peaked distribution. The bias is reduced by 2% as well as the resolution. On the other hand, in case of preshowering photons, the resolution is not improved.

Regarding the overall improvement, the PDF function describing the fluctuations of the signal will be given by Eq. 6.3 in the reconstruction procedure.

6.3.2 Designed PDF for each station risetime

The reconstruction of the maximum depth X_{max} is performed using the part of the universality model predicting the shape of the signal [132], from which the risetime can be derived. The PDF functions assigned to stations used in the minimisation process describe the variation of the measured risetime around the universality prediction. In a first attempt we use a simple Gaussian form having as mean m the value of the predicted risetime $t_{1/2}^{univ}$. The assignment of the corresponding standard deviation is not straightforward as no parameterisation of the risetime uncertainty for photon-induced shower exists. Therefore, we use the risetime uncertainty parameterised for data in [126] (introduced briefly in Sec. 4.4.2) which describes the average risetime of data as function of the distance to the shower axis r and zenith angle θ. The uncertainty is also determined empirically using pairs of detector placed 11 m apart from each other, and also detectors at similar distances from the shower core. The resulting parameterisation from [126] is

given by:

$$\sigma_{bench}(r,\theta,S) = r\frac{J_a + J_b\cos^2(\theta)}{\sqrt{S}} \tag{6.4}$$
$$J_a = 0.3658 - 0.07197\sec^2(\theta)$$
$$J_b = -6.958\ 10^{-8} + 1.476\ 10^{-7}\cos(\theta)$$

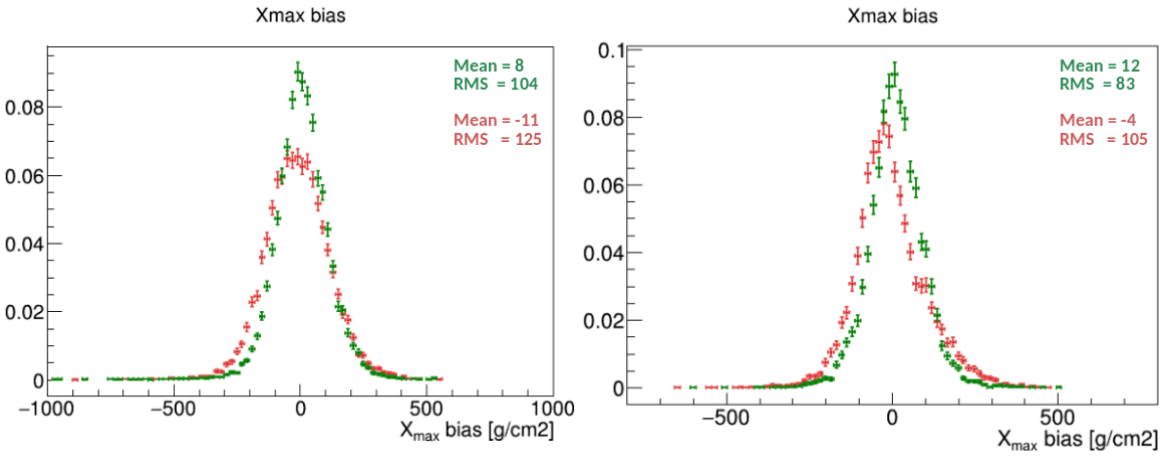

Figure 6.17: Distributions of the reconstructed X_{max} bias resulting from Eq. 6.5 in red and from Eq. 6.7 in green. The distributions are normalised such that their integral is equal to 1. Left: the distributions are reported for simulated non-preshowering photon showers. Right: the distributions are reported for simulated preshower photon shower.

Although the average risetimes observed in photon-induced showers are larger than the ones observed in data, the order of magnitude of the uncertainty, being obtained with the benchmark function, is supposed to be the right one. The resulting PDF form is written as:

$$G(t_{1/2}^{obs} \mid \mu = t_{1/2}^{univ}, \sigma = \sigma_{bench}(r,\theta,S)) \tag{6.5}$$

We tested if the variations of the risetime are correctly described by Eq. 6.5. The last step of the reconstruction procedure, the reconstruction of X_{max}, is performed while other parameters are fixed to their respective true MC values. On Fig. 6.17, the obtained X_{max} bias, defined as the difference between the reconstructed value and the true MC value $X_{max,GH}$, is shown in red for the simulated showers from non-preshowering photons (left) and from preshowering ones (right). We observe a bias of -11 g/cm^2 (-4 g/cm^2) with a standard deviation of 125 g/cm^2 (105 g/cm^2) respectively. While the obtained resolution is not comparable with the FD one, the goal of this work is only to use the reconstructed X_{max} of photons as a discriminating variable between photons and nuclei.

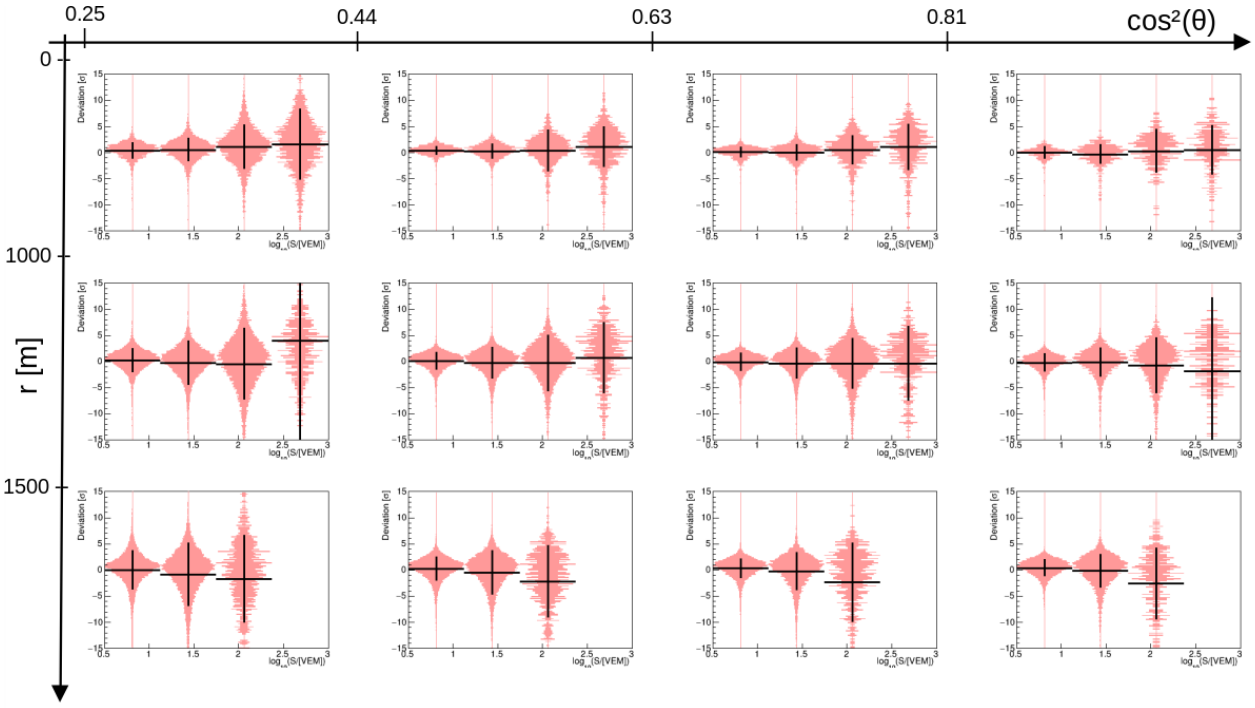

Figure 6.18: Distributions of the deviation of the measured risetime with respect to universality prediction in units of σ_{bench}, as function of 4 bins of signal S. It is reported for 4 bins of $\cos^2(\theta_{MC})$ ([0.25,0.4375,0.625,0.8125,1]) and 3 bins of distance to the axis r ([0,1000,1500,>1500] m). Only events with $\theta_{MC} < 60°$ and having a Gaisser Hillas X_{max} not more than 150 g/cm^2 underground are used. Moreover, only stations passing the selection described in Sec. 6.1.4 are used.

The results are reasonable in view of the simplicity of the designed likelihood function but there is room for improvements, especially in the determination of the risetime uncertainty. To adapt the risetime uncertainty to photon-induced showers, we scale the uncertainty using photon simulations. For each of the 3 parameters used in Eq. 6.4, namely the distance r, the zenith angle θ, and the signal S, we compute the deviation of the measured risetime with respect to the prediction in unit of sigma:

$$\frac{t_{1/2}^{obs} - t_{1/2}^{univ}}{\sigma_{bench}(r, \theta, S)} \tag{6.6}$$

The phase space is divided in 3 bins for r, 4 for θ and S. The results are shown in Fig. 6.18 only for stations passing the selection described in Sec. 6.1.4. The distribution in each bin is represented in pink with the corresponding profile superimposed in black indicating the mean value in the bin and the standard deviation of the distribution. This standard deviation depicts the under or over estimation of the risetime uncertainty for photon showers with respect to data. Indeed, a standard deviation of 3 would mean that the uncertainty in the photon case is underestimated by a factor 3 by the value obtained from data. The corresponding values of the standard deviations observed in each signal bin of Fig. 6.18 are reported in Fig. 6.19 and tend to increase with increasing signal.

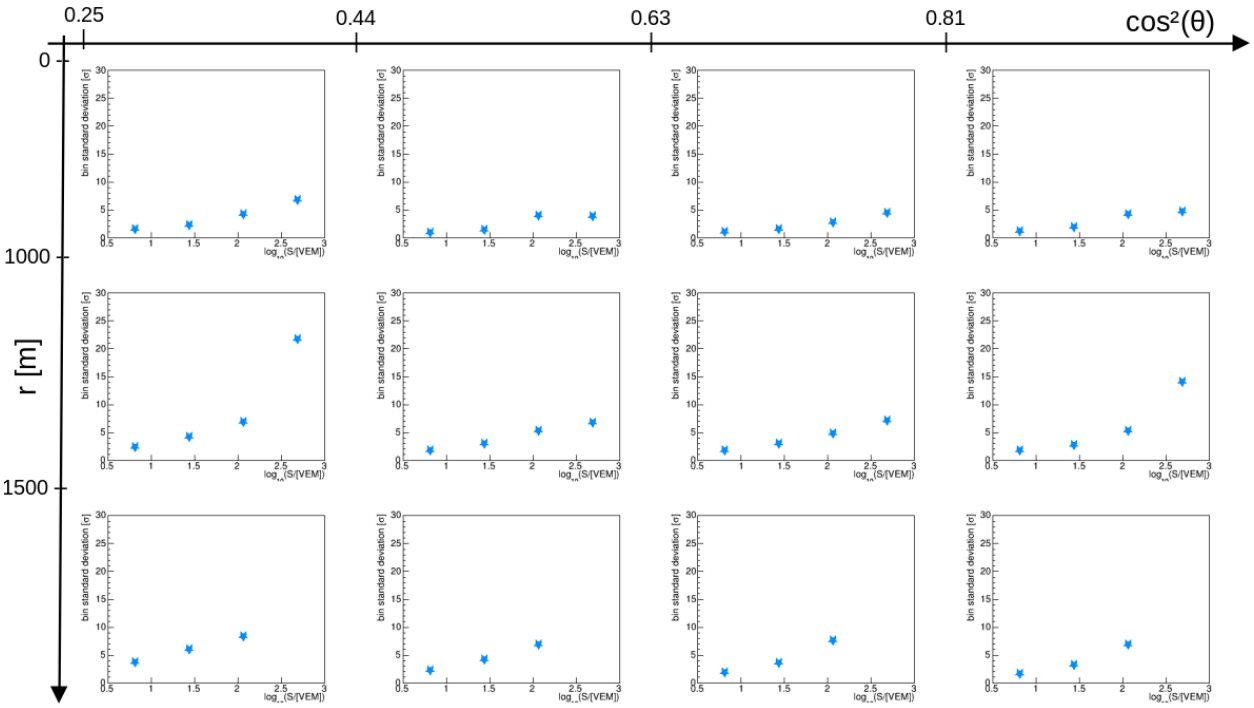

Figure 6.19: The standard deviations of each bin of distance r, signal S and MC zenith angle obtained from Fig. 6.18.

The tests are repeated for the new function

$$G(t_{1/2}^{obs} \mid \mu = t_{1/2}^{univ}, \sigma = \sigma_{bench}(r,\theta,S)\text{scale}(r,\theta,S)) \tag{6.7}$$

in which $\text{scale}(r,\theta,S)$ is the scaling of the risetime uncertainty. The results are reported by the green distributions in Fig. 6.17 for non-preshowering photons in the left panel and preshowering photons on the right panel. Compared to the non-scaled case (Eq. 6.5), the standard deviation decreases from 125 g/cm^2 to 104 g/cm^2 for non-preshowering photons and from 105 g/cm^2 to 83 g/cm^2 for preshowering photons, improving the photon X_{max} reconstruction. The PDFs defined by Eq. 6.3 and Eq. 6.7 will be used in the designed reconstruction procedure.

Summary

In this chapter, the motivations for an universality-based reconstruction of the X_{max}, core position and primary energy of photon-induced shower with the data recorded by the SD were discussed. We presented the different steps of the reconstructions procedures which relies on the method of maximum likelihood fit. Two distinct reconstruction following this procedure were designed: one for preshowering photons and one for non-preshowering photons. The PDFs used in the likelihood functions were determined and tested.

Chapter 7

Search for UHE photons with universality

Contents

In this chapter, we apply the designed reconstruction procedure to photon simulations to present and discuss the obtained performances. The variables built to discriminate photon showers from hadronic ones are presented and processed in a Fisher analysis. The design of the analysis requires the use of proton simulations alongside the photon ones to evaluate and improve its discriminating power. Finally, the analysis is applied on a small data sample representing $\sim 2\%$ of the SD data and the results are compared to the ones recently published.

7.1 Results of the reconstruction procedure

In the following, the results obtained after applying the designed universality reconstruction procedure for photons are presented. To compare to those from the recently published analysis [32], the selection of events is matched: the selected range of zenith angle is $[30°, 60°]$, with $E_{\gamma} > 10^{19}$ eV and $E_{had} > 10^{18.5}$ eV.

7.1.1 Photon energy estimation

The distribution of the energy bias, defined as $E_\gamma/E_{MC}-1$ (Fig. 7.1), for non-preshowering photons has a bias of of 4.7% with a resolution of 37%. The mean value of the bias is actually dragged by the tail observed at the highest values and corresponds to events with a large muon content with respect to the average for photons ($< N_\mu >_\gamma = 0.25$, see Sec. 6.1.3). This is illustrated in Fig. 7.2 in which the energy bias is plotted as function of N_μ, derived from Eq. 6.1. The dependency with the muon content is clear. The energy bias is comparable with the one obtained by the analysis described in [32]. A certain number of preshowering photon showers are misidentified as preshowering photons. These events enlarge the overall bias. This is illustrated in the bottom-left panel of Fig 7.1 which shows the energy bias for correctly identified ("right-flagged") events in green and wrongly identified ("wrong-flagged") events in red. The events not correctly identified represent 16% of all non-preshowering photons. Their energy is overestimated on average by 65% while right-flagged event have an energy resolution of 32% and a bias smaller than 2%.

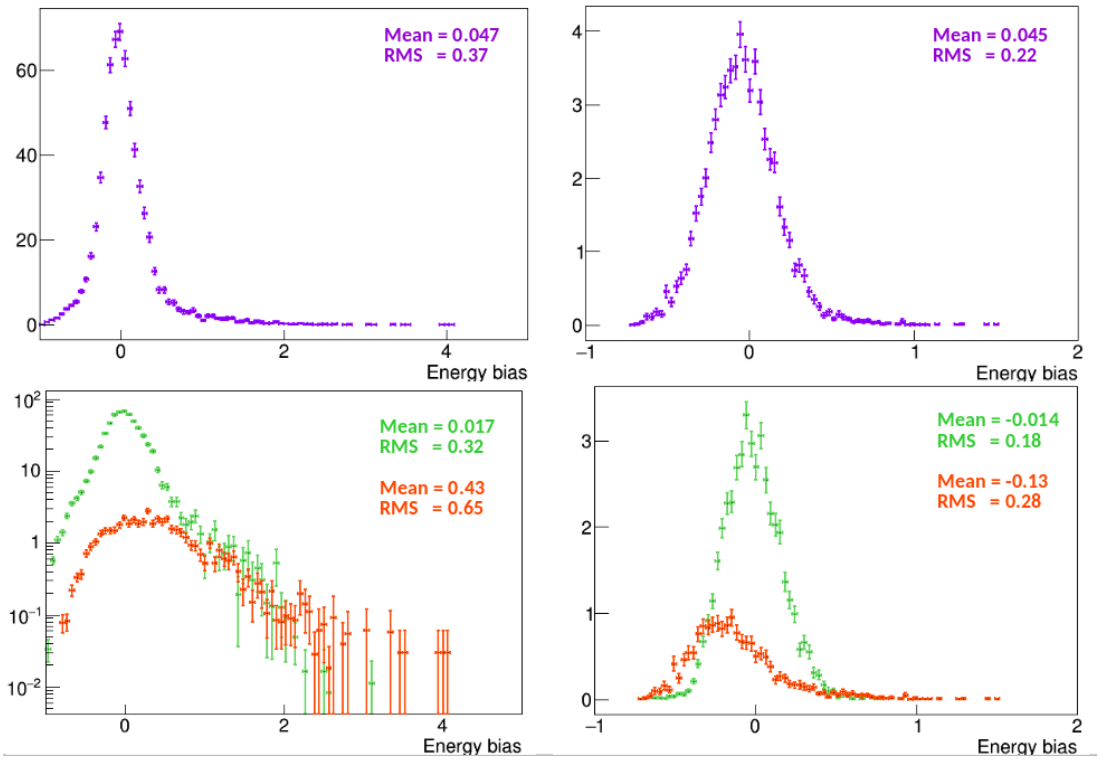

Figure 7.1: Reconstructed photon energy bias distribution for photon simulations the selected events. Top-left: distribution for non-preshowering photons. Top-right: distribution for preshowering photons. Bottom-left: distribution for right-flagged (wrong-flagged) non-preshowering photons in green (red). Bottom-right: distribution for right-flagged (wrong-flagged) preshowering photons in green (red).

For preshowering photons, the energy is reconstructed with a bias of -4.5% and a resolution of 22%. Events correctly identified are reconstructed with a bias of -1% and a resolution of 18%. The percentage of wrong-flagged preshowering photon events is reaching

24%, the bias obtained for these events is -13% with a resolution of 28%. In comparison, the bias for preshowering photons resulting from the analysis described in [32] reaches $\sim -30\%$. The overall reconstruction of the energy presented in this work reduces the energy bias of preshowering photon from -30% to -1%. Moreover, misidentified events have an energy bias more than a factor two less that the one obtained in [32].

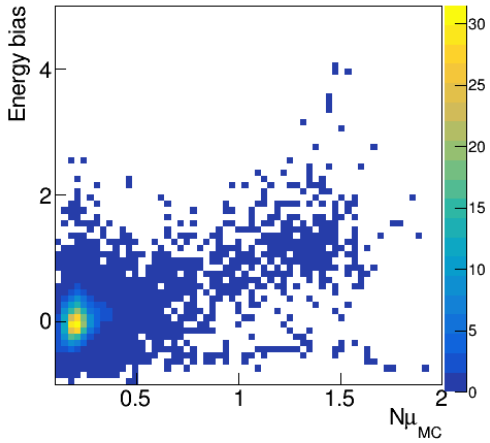

Figure 7.2: Energy bias of non-preshowering photon simulations as function of N_μ (derived from Eq. 6.1). Only events with $\theta_{MC} < 60°$ and $X_{max,GH}$ not more than 150 g/cm^2 below ground level are used. The tail observed at the right end of the distribution in the top-left panel of Fig. 7.1 is created by events with hadron-like muon content.

7.1.2 Core position reconstruction

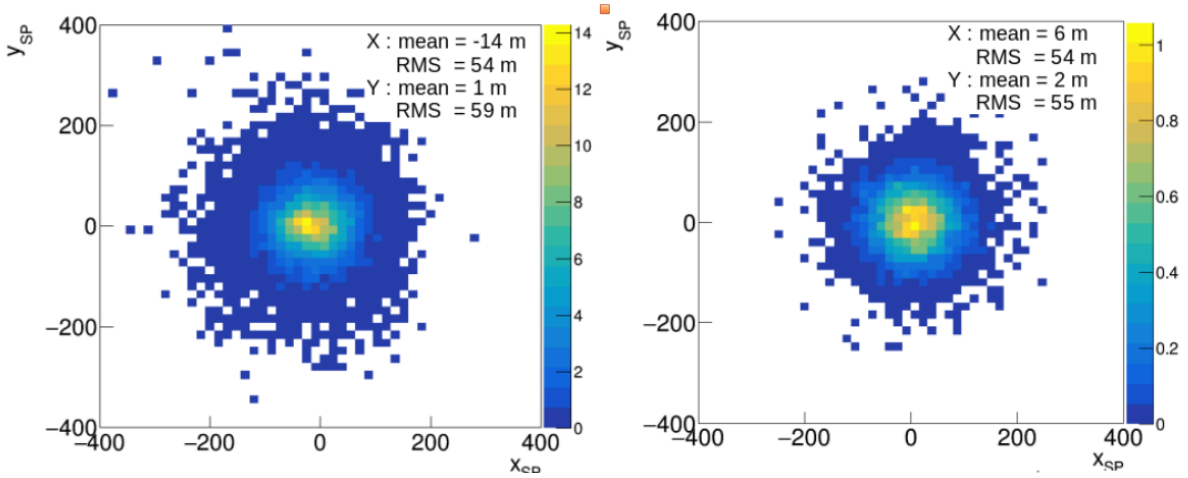

Figure 7.3: Reconstructed core position in the MC shower plane (x_{SP}, y_{SP}). The distribution of non-preshowering (preshowering) photon showers is shown in the left (right) panel.

The reconstructed core position in the MC shower plane (x_{SP}, y_{SP}) is shown in Fig. 7.3 for non-preshowering photons (left) and for preshowering photons (right). No bias is observed in case of preshowering photons, but a small one of -14 m can be seen for non-preshowering photons on the x_{SP} axis which corresponds to a bias towards the late part of

the shower. This bias, as well as the width of the distribution, is more important for events wrongly identified as preshower (top-right panel of Fig. 7.4) with a bias of -27 m. This is also observed in the case of preshowering photons with a bias of 23 m (bottom-right panel).

In comparison with the SD core position reconstruction which does not take into account the azimuthal asymmetry of stations, resulting in a bias of 50 m toward the early part of the shower (see Fig. 6.1), the universality-based reconstruction is an improvement. It is important to note that the width of the distribution is also reduced from $\simeq$ 70 m and $\simeq$ 80 m in the x_{SP} and y_{SP} directions respectively to $\simeq$ 55 m in both cases.

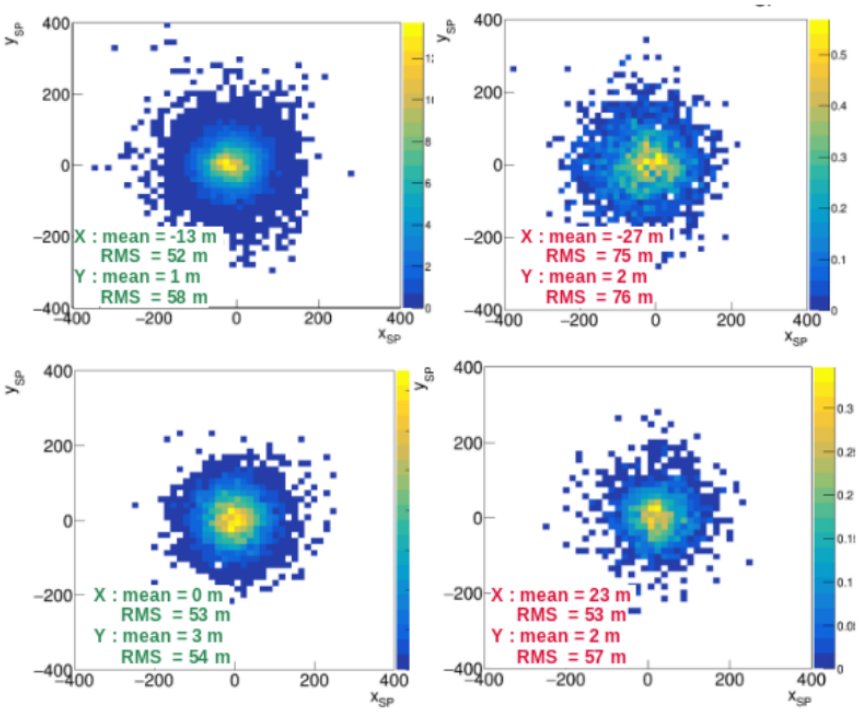

Figure 7.4: Reconstructed core position in the MC shower plane (x_{SP}, y_{SP}). Top: the distribution of rightly (wrongly) identified non-preshowering photons is reported in the left (right) panel. Bottom:distribution of rightly (wrongly) identified preshowering photons is reported in the left (right) panel.

7.1.3 X^{γ}_{max} reconstruction

The distributions of $X^{\gamma}_{max} - X_{max,GH}$ are shown on Fig 7.5 (top panels). A bias of 20 g/cm^2 with a resolution of 139 g/cm^2 are obtained in the case of non-preshowering photons. A tail is at the left end of the distribution, extending below -500 g/cm^2. This originates from photon-induced showers with a Gaisser Hillas X_{max} close to or under the ground level: in this configuration the fit of the longitudinal profile of the simulated shower is not very reliable. This is illustrated in Fig. 7.6 in which the bias is plotted as function of the depth difference between the value from the Gaisser Hillas fit and the ground. This is also why events with a Gaisser Hillas X_{max} more than 150 g/cm^2 below ground are not used to check the X_{max} reconstruction.

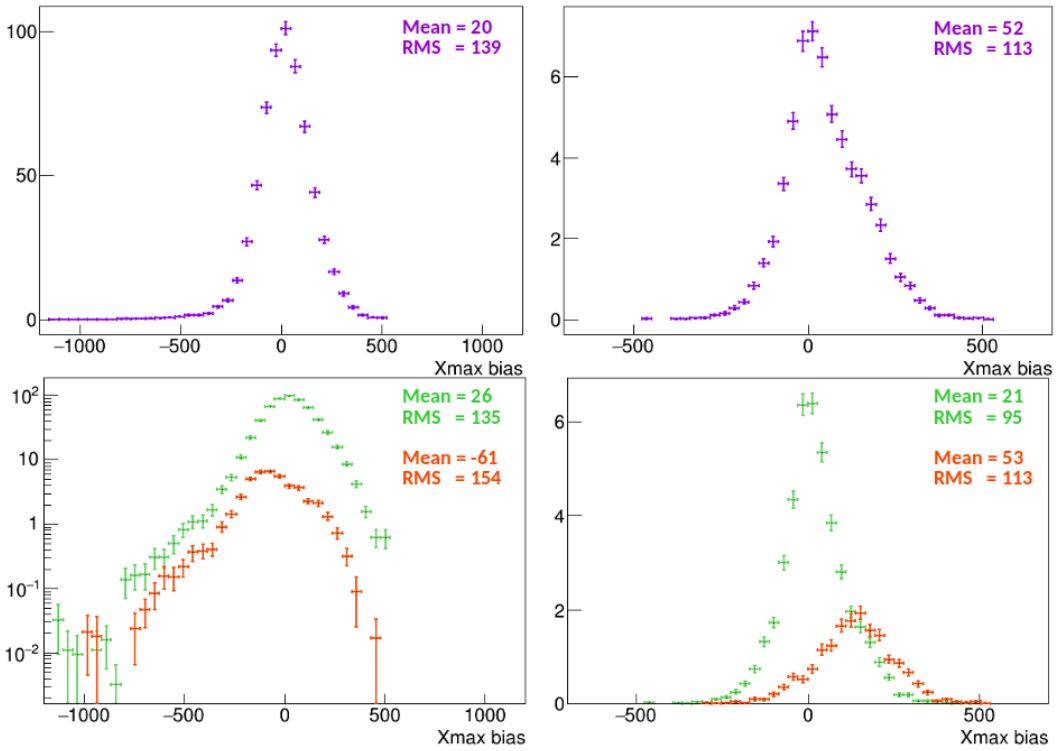

Figure 7.5: Reconstructed X_{max} bias distribution for photon simulations for the selected events. An additional cut rejecting events with a Gaisser Hillas X_{max} more than 150 g/cm^2 under ground level is added to avoid non-physical values of X_{max}. Top-left: distribution for non-preshowering photons. Top-right: distribution for preshowering photons. Bottom-left: distribution for right-flagged (wrong-flagged) non-preshowering photons in green (red). Bottom-right: distribution for right-flagged (wrong-flagged) preshowering photons in green (red).

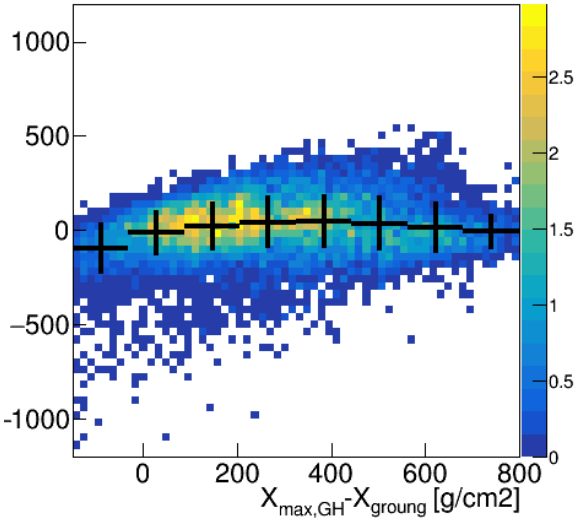

Figure 7.6: The X_{max} bias as function of the depth difference between the Gaisser Hillas fit and the ground. Only events with $\theta_{MC} < 60°$ and $X_{max,GH}$ not more than 150 g/cm^2 below ground level are used.

In the case of preshowering photons the mean of the distribution is of 52 g/cm^2 and the resolution of 113 g/cm^2. Two peaks are visible (bottom-left panel of Fig. 7.5) corresponding to wrong-flagged events (red). The events not correctly identified as preshowering photons have large over-estimated values and are responsible for the second peak as well as for the larger bias.

The resolutions and biases are not comparable with those reached by the FD but the goal for the present photon search is to reach a resolution good enough to use the reconstructed photon X^{γ}_{max} as a separation variable. Thus, the discriminating power of X^{γ}_{max}, combined with other variables, will be evaluated in the next sections.

7.2 Application to protons simulations

In this section, the photon reconstruction is applied to proton simulations. The reconstructed photon X^{γ}_{max} is used in a multivariate analysis (the Fisher Discriminant Analysis [141]) similarly as in the SD search reported in [32], with two other variables described in the next section, R_{sig} and R_{RT}, built with the log-likelihood functions presented in Sec. 6.3. The addition of these new variables aims to exploit more information from the reconstruction. The discriminating power given by different combinations of discriminating variables are tested by looking at the percentage of simulated proton-induced showers passing the selection cut, defined as the median of the non-preshowering photons distribution. This cut is the one used in the photon search of the Pierre Auger Collaboration and is a compromise to obtain a reasonable balance between efficiency and purity.

7.2.1 Discriminating variables based on the likelihoods

At the end of the reconstruction procedure summarised in Fig. 6.8, an additional step is implemented: the reconstruction of X_{max} in the proton hypothesis. This reconstruction is performed in a way similar to the fourth step of the procedure but the values of the parameters are changed to match the proton hypothesis case:

- The mean photon N_{μ} is set to the mean N_{μ} derived from proton simulations generated with the EPOS-LHC model. The value is taken from [125] and is equal to $< N_{\mu} >_p = 1.4$
- The energy is fixed to the standard SD reconstructed energy E_{had} instead of the reconstructed photon energy E_{γ}
- The core position is also fixed to the standard SD reconstructed value but corrected from the azimuthal asymmetry following the parametrisation established in Sec.6.2 (see Fig. 6.11)
- The risetime uncertainty σ_{bench} from the data benchmark is unchanged, since in this case the scaling required for photons is not needed.

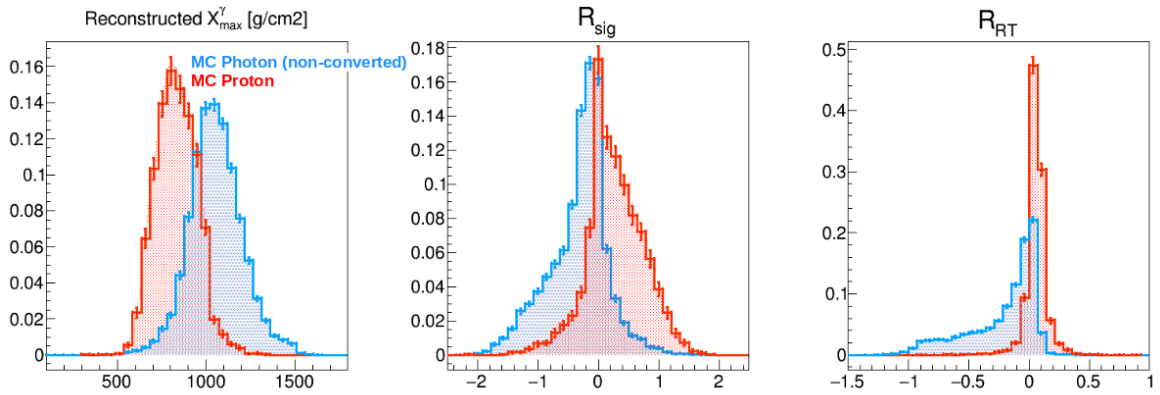

Figure 7.7: From left to right: distributions of X^{γ}_{max}, R_{sig} and R_{RT} for non-preshowering photon simulations in blue and protons simulations in red. The distributions are normalised such that their integral is equal to 1.

Two different sets of shower parameters are then obtained: one for the photon hypothesis and one for the proton hypothesis. By using these sets of reconstructed parameters we can defined likelihood ratios comparing the photon hypothesis and the proton hypothesis. These ratios indicate if the reconstructed shower has a higher probability to correspond to a photon shower or to a proton one. Thus, the following variables in Eq. 7.1 and Eq. 7.2 are defined:

$$R_{sig} = \frac{L^{\gamma}_{sig}}{L^{p}_{sig}} \tag{7.1}$$

$$R_{RT} = \frac{L^{\gamma}_{RT}}{L^{p}_{RT}} \tag{7.2}$$

where R_{sig} is the ratio of the sum of the signal log-likelihoods over the selected stations L^{γ}_{sig}, defined by Eq. 6.3, in the photon hypothesis and L^{p}_{sig} in the proton hypothesis. Similarly, R_{RT} represents the ratio of the risetime log-likelihoods defined by Eq. 6.7.

The normalised distributions of X^{γ}_{max}, $\log_{10}(R_{sig})$ and $\log_{10}(R_{RT})$ are reported in Fig. 7.7 from left to right respectively, for non-preshowering photon simulations in blue and proton simulations in red. A separation between the two X^{γ}_{max} distributions is observed, as well as for R_{sig} and R_{RT}. While the shapes of the X^{γ}_{max} and R_{sig} distributions are similar for protons and photons, a tail is visible at the left-end of the distribution of R_{RT} for photons while that of protons is rather peaked. This tails originates from more inclined showers as illustrated in the bottom-right panel of Fig. 7.8 which shows R_{RT} as function of $\cos^2(\theta_{MC})$ for photons (histogram and black profile) and for protons (red profile). The dependencies of X^{γ}_{max}, R_{sig} and R_{RT} with the Monte-Carlo energy are reported at the top of Fig. 7.8 from left to right. The separation between photons and protons is more important at higher energies for X^{γ}_{max} and R_{RT} while it stays rather constant for R_{sig}. The bottom panels show the dependencies with $\cos^2(\theta_{MC})$ of X^{γ}_{max}, $\log_{10}(R_{sig})$ and $\log_{10}(R_{RT})$ respectively. The separation between photons and protons is only zenith dependent for R_{RT}, no dependency is observed for the other variables.

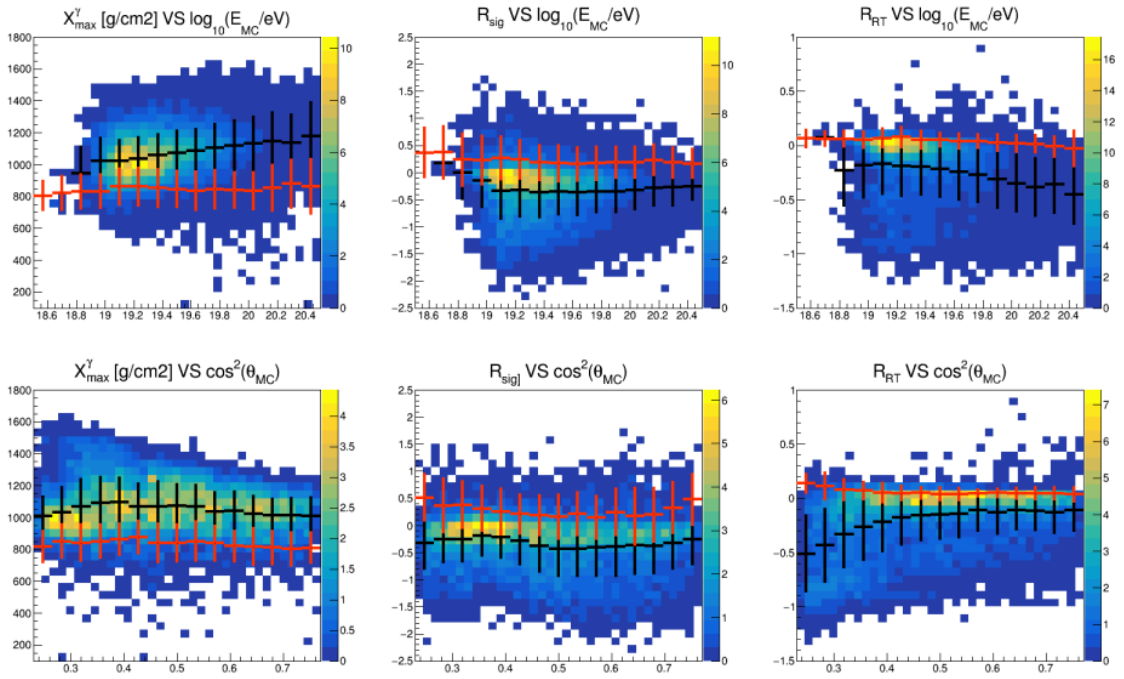

Figure 7.8: From left to right: X^{γ}_{max}, R_{sig} and R_{RT} as function of $\log_{10}(E_{MC}/eV)$ for the top panels and as function of $cos^2(\theta_{MC})$ for bottom ones, for photon simulations (blue histograms and black profiles) and protons simulations (red profile).

7.2.2 Fisher Analysis

The Fisher Linear Discriminant Analysis (FLDA) [141] is used to separate two populations of data in a multidimensional space by applying a linear transformation to the data and therefore reducing the space to one dimension. The FLDA method finds the axis on which the separation between the projection of the two classes is maximised. The distance between the means of each population is maximised while, at the same time, the scatter of individual population is minimised, as illustrated on Fig. 7.9 [141].

Denoting μ_1 and μ_2 the means of the populations to separate and σ_1 and σ_2 their respective variances, the ratio to maximise is given by:

$$J = \frac{(\mu_1 - \mu_2)^2}{\sigma_1^2 + \sigma_2^2} \tag{7.3}$$

This ratio can be expressed in terms of matrices as:

$$J(\mathbf{w}) = \frac{\mathbf{w^T}.S_B.\mathbf{w}}{\mathbf{w^T}.S_W.\mathbf{w}} \tag{7.4}$$

The vector $\mathbf{w}$ is the unitary vector whose direction is the one of the final axis, S_W the covariance matrix which measures the variances of data in each of the populations (the W standing for "within classes"), and S_B covariance matrix measuring the variances for all the data (the B standing for "in between classes").

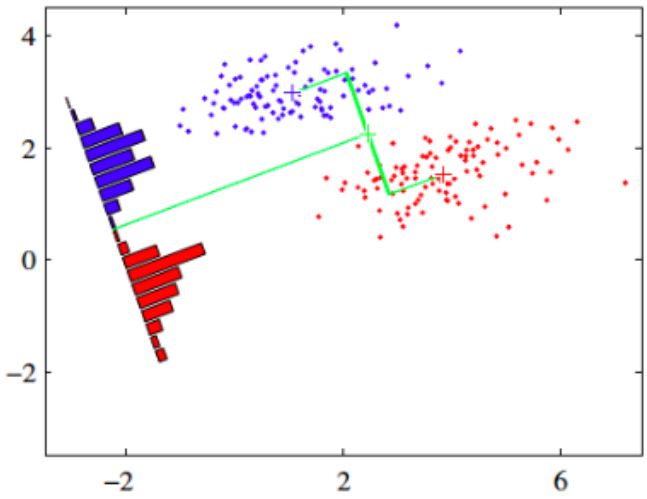

Figure 7.9: Illustration of the Linear Discriminant Analysis. Taken from [141].

In the following, the FLDA is trained with a events sub-sample of the non-preshowering photon simulations (3000 events) and a sub-sample of the proton simulations (3000 events). The first one is defined as signal while the other is considered as background. The remaining simulated photon and proton showers is called the test sample. The training sample is used to find the Fisher axis, on which the test sample is projected. From this, the separation power between protons and photons resulting from the analysis can be deduced.

7.2.3 Proton contamination

X^{γ}_{max}, R_{sig} and R_{RT} are combined in a Fisher analysis. To evaluate the separation between the proton and photon showers, we define the candidate cut as in other photon searches presented in Sec. 4.4 as the median of the distribution of non-preshowering photons on the Fisher axis. All protons showers falling above the median are considered as background contamination. Different combinations of discriminating variables are tested and the percentage of protons above the photon median is reported in each case in the table of Fig. 7.10.

The combinations from A to D evaluate the association of X^{γ}_{max} with the likelihood ratios R_{sig} and R_{RT}. The comparison between B (combination of X^{γ}_{max} and R_{RT}) and C (combination of X^{γ}_{max} and R_{sig}) highlights that the ratio of the likelihood designed for the risetime is more efficient than that of the signal likelihoods ratio, the background decreasing from 1.8% to 0.96%. The results of the combination of X^{γ}_{max} with both likelihood ratios is reported in A and D. In case A, the weight given to both ratios in the Fisher analysis is the same. In case D, no constrain is given and the FLDA can give more weight to one variable than the other. As expected, since R_{RT} is found to be more efficient than R_{sig}, the combination D is largely more effective and the contamination falls from 1.5% to 0.68%.

Combinations of variables	A	B	C	D	E	F	G
X^{γ}_{max}							
R_{RT}	Same relative weights						
R_{sig}	Same relative weights						
θ							
E_{γ}							
Proton contamination [%]	1.5 ± 0.23	0.96 ± 0.17	1.8 ± 0.25	0.68 ± 0.16	0.65 ± 0.16	0.57 ± 0.15	0.51 ± 0.13
Number of events	220	353	330	102	108	211	211

Figure 7.10: Table showing the proton contamination in percentage for different combinations of variables in a Fisher analysis. Green-filled boxes indicate that the variable is used in the FLDA.

To account for the energy and zenith dependencies of the variables, the implementation of the reconstructed photon energy E_{γ} and the zenith angle θ is tested in addition to X^{γ}_{max}, R_{sig} and R_{RT}. In cases E and G, they are added one at a time, and together for F. Although it is not significant, the energy dependencies observed in Fig. 7.8 seems to improve slightly the separation between photons and protons (decrease of about $\sim 0.1\%$), while the addition of θ has no effect. Thus, the best case seems to be the combination of X^{γ}_{max}, R_{sig}, R_{RT} with E_{γ}. However, the results obtained for combinations D, E, F and G stay within the uncertainties.

In the last line of Table 7.10, the number of events corresponding to the contamination is reported, i.e. the weights are not applied (for reference, the proton test sample is composed of 10824 simulated showers). Fig. 7.11 shows the Fisher distributions of photons and protons plotted as function of the reconstructed photon energy. The contours correspond to 10, 30, 50, 70 and 90% of the distributions as indicated by the legend, and the median of photons is indicated by the black line. The left panel corresponds to the Fisher combination D (X^{γ}_{max}, R_{sig}, R_{RT}) while the right panel corresponds to the combination G in which the energy is added. We observe that, although the contamination is smaller when the reconstructed photon energy is used (F and G), the number of events is twice larger ($\simeq$ 100 against $\simeq$ 200). This means that implementing the energy in the FLDA results in more high energy events falling above the selection cut. The Fisher axis rotates clock-wise and more high energy events are selected above the median cut.

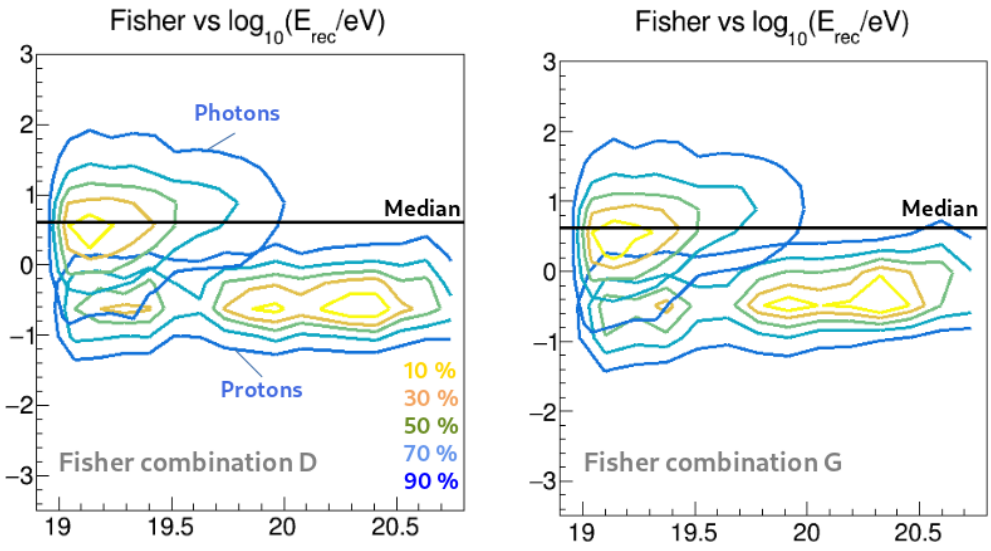

Figure 7.11: Left: The Fisher values resulting from the combination of X^{γ}_{max}, R_{sig}, and R_{RT} as function of the reconstructed photons energy, for simulated non-preshowering photon and proton showers. The contours correspond to 10, 30, 50, 70 and 90% of the distributions as indicated by the legend, and the median of non-preshowering photons is indicated by the black line. Right: Identical plot for the Fisher combination G in which the reconstructed photon energy is added.

In the following section, the Fisher analysis is applied to the "burn" sample of data (see below). As data is not only composed of protons but also heavier nuclei, we expect the separation to be more important: the X_{max} gets smaller with increasing mass while the number of muons gets more important, resulting in the behaviour of heavier hadron-induced showers to be even less photon-like.

7.3 Application to the data burn sample

The burn sample represents 1.8% of the data collected by the surface detector from the 1st January 2004 to 30th June 2020. It is used to test the photon searches with real data and was used in the SD search analysis published in [32]. Following the selection of events discussed earlier in this thesis, the remaining number of events is of 1106. The Fisher method is trained with the non-preshowering photon simulations and the burn sample. To visualise the difference between proton simulations and data, proton simulations are projected on the resulting Fisher axis. This is done from the variables combination D, E, F and G as their proton contamination were very close and within the uncertainties.

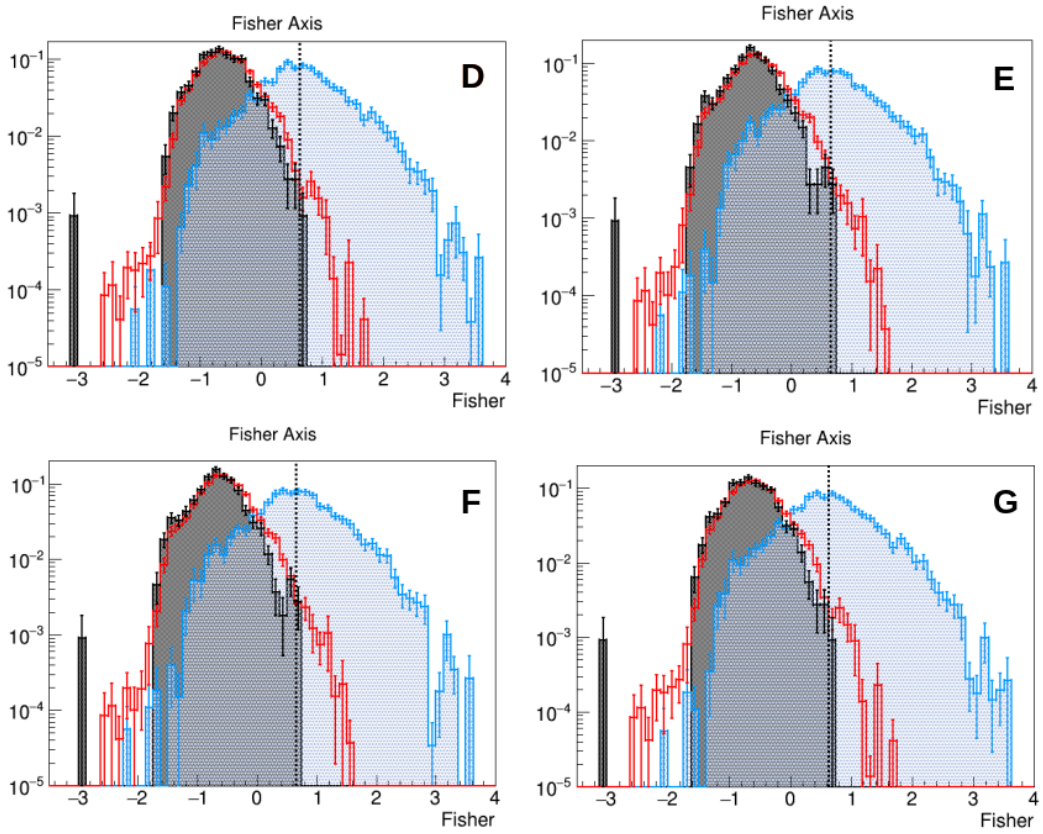

Figure 7.12: Results of the Fisher analysis trained on the burn sample and non-preshowering photons simulations for four combinations of variables (D, E, F and G). The normalised distributions of the burn sample is reported in black while the non-preshowering photon simulations are in blue and the proton simulations in red. The median of photons is indicated by the black dashed line.

Fig. 7.12 shows the distributions of non-preshowering photon simulations (blue), of proton simulations (red) and of the burn sample (black), on the Fisher axis for the four combinations of variables considered. The selection cut corresponding to the median of non-preshowering photons is indicated by the dashed black line. In case of the combinations D and G which respectively associate (X^{γ}_{max}, R_{sig}, R_{RT}) and (X^{γ}_{max}, R_{sig}, R_{RT}, E_{γ}), only one same data event is found above the selection cut. The position of this event in the distributions of the discriminating variables is indicated in red in the top panels of Fig. 7.13, and we observe that it has a value of R_{RT} at the very right-end of the distribution of data, making it looks like a photon. In the two other cases where the zenith angle is used in the Fisher analysis, namely E and F, the same three events are found above the median. Their positions in the distributions of X^{γ}_{max}, R_{sig}, and R_{RT} are indicated by three coloured lines in the bottom panels of Fig. 7.13. Each of these events is found to be at least once in the tail of the burn sample distributions making it look photon-like: the event indicated in orange has a photon-like reconstructed X^{γ}_{max}, the yellow one is in the left-end tail of the R_{sig} distribution and the brown one is found at the left-end tail of the R_{RT} distribution.

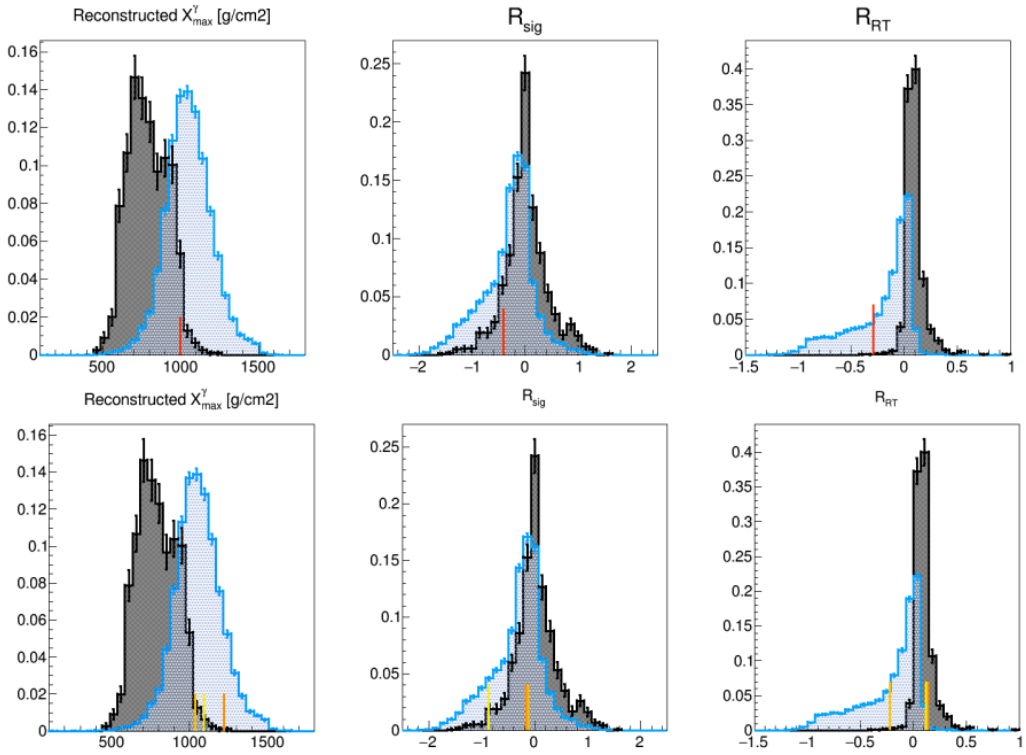

Figure 7.13: Each panel shows the normalised distributions of the burn sample (black) and the non-preshowering photon simulations (blue). Top: the position of the burn sample event passing the selection cut in case D and G in the distribution of X^{γ}_{max}, $\log_{10}(R_{sig})$, and $\log_{10}(R_{RT})$ respectively. Bottom: the position of the three burn sample events passing the selection cut in case E and F in the distribution of X^{γ}_{max}, $\log_{10}(R_{sig})$, and $\log_{10}(R_{RT})$ respectively.

As the number of events in the burn sample of data is rather low, an exponential fit of the 5% right tail of data, corresponding to 55 showers, is performed to have a better estimate of the background. This is done through an unbinned likelihood fit. With respect to a binned fit, this allows to lose less information and the resulting fit does not depend of the bins width. The fits for combinations D to G are shown in Fig. 7.14 by the orange line, with the slope of the exponential and the expected number of events from the burn sample (integral of the function above the median cut). From these values, we can estimate the expected number of candidate events in the full SD data set (except the burn sample). As the burn sample represents 1.8% of data, the expected number of events from the fits are multiplied by $\simeq 55$, which is superior to the 16 photon candidates found in the search sample of data in [32] (it corresponds to 99, 132, 127 and 99 expected events for combination D to G respectively).

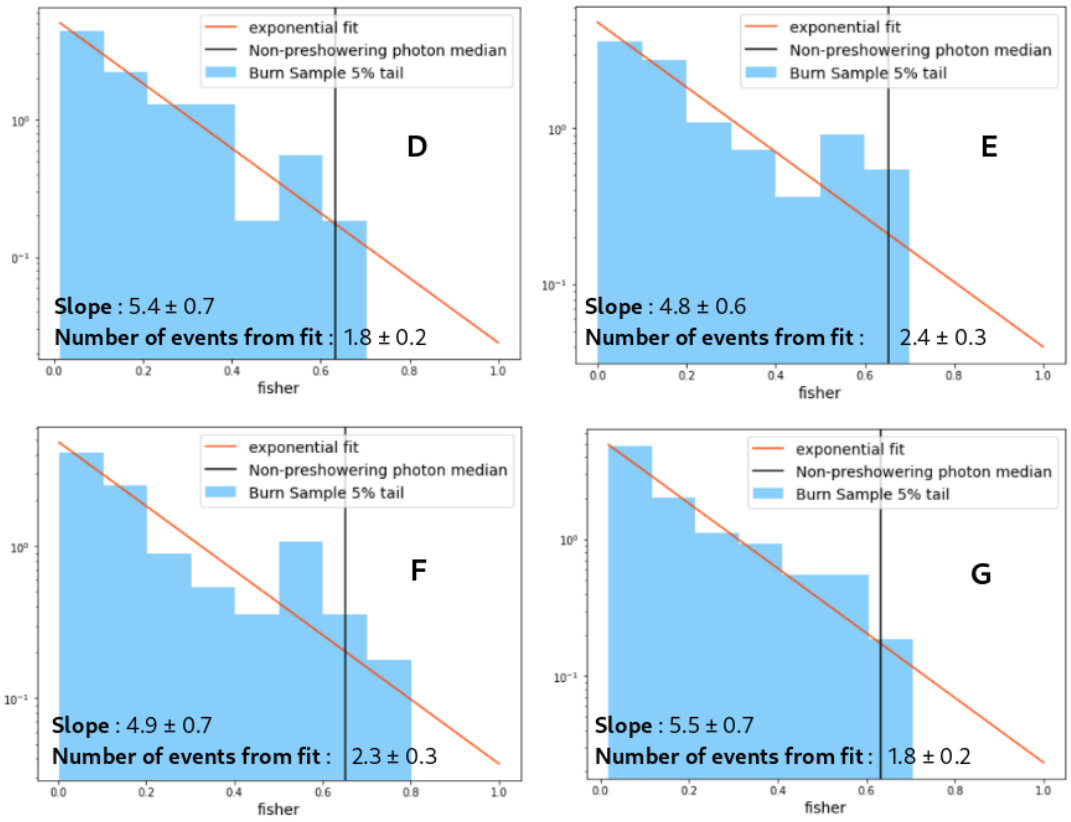

Figure 7.14: For Fisher combinations D to G: the 5% tail of the burn sample on the Fisher axis (blue), with the exponential fit of the tail (orange), and the median of non-preshowering photons (black). The slope of the exponential is indicated with the corresponding number of events estimated from the fit (i.e. integral from the median cut).

The number of events in the burn sample to train the FLDA in [32] was equal to 886. Here, 1106 events are selected out of 1236. This could hints that the quality cuts applied throughout the present analysis might be not sufficient: some events in the tail of the burn sample distribution, which end up above the median candidate cut, could have been rejected before applying the analysis. By looking at the distributions of E_{had} (Fig. 7.15, right) for the 886 (purple) and 1106 (black) burn sample events, we notice that the difference is due to much more lower energy events being selected in this analysis. This can be also illustrated by looking at the selection efficiency of photons (Fig. 7.15, left) in comparison with the one published in [32]. The photon efficiency above a threshold E_0 is calculated as the weighted ratio between the photon simulations with $E_\gamma > E_0$ on which all the selection criteria[1] have been applied, to the total number of photon simulations with $E_{MC} > E_0$ and $30° < \theta_{MC} < 60°$. The efficiencies obtained in our analysis are ~ 30 to $\sim 50\%$ higher than in the SD analysis from [32].

Although cuts are similar in both analyses, the main difference arises from the quality cut required for the Δ variable (Sec. 4.4.1), i.e. non saturated stations above 6 VEM within a 600 m to 2000 m distance range from the shower axis. This could hint that

[1]Cuts: photon reconstruction requirements, zenith range $[30°, 60°]$, $E_{had} > 10^{18.5}$ eV, median selection cut.

the 5 VEM required in our analysis is not sufficient, but to verify this statement the whole procedure and analysis should be repeated. Another interesting path to explore could be the use of a new benchmark describing the average behaviour of the risetime for data. In an internal note of the Pierre Auger Collaboration, a risetime benchmark differentiating high-gain saturated stations from non-saturated was developed [142]. This could potentially improve the X^{γ}_{max} reconstruction and by consequence the performances of this analysis.

Energy Threshold	10 EeV	20 EeV	40 EeV
SD anaylsis [32]	0.26	0.36	0.39
Fisher D	0.40	0.50	0.51
Fisher E	0.40	0.50	0.51
Fisher F	0.40	0.51	0.52
Fisher G	0.40	0.51	0.52

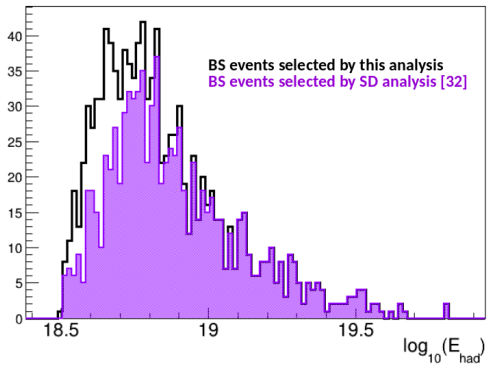

Figure 7.15: Left: photon efficiency for three energy thresholds (10, 20 and 40 EeV) for Fisher combinations D to G, compared to the values obtained in [32]. Right: distribution of $\log_{10}(E_{had}/eV)$ for burn sample (BS) events selected in this work (black) and those selected in [32] (purple).

Summary

The designed reconstruction procedure detailed in the previous chapter was applied to photon simulations. The biases of the reconstructed parameters with respect to their true MC values were presented. In particular, we obtained an energy bias for non-preshowering photons comparable to that published in [32] and no bias was observed for preshowering photons.

The constructed X^{γ}_{max} is combined in an FLDA with two other discriminating variables, R_{sig} and R_{RT}. They are based on the likelihood functions and indicate if the reconstructed event is more photon or proton-like. Different combinations of these variables with E_{γ} and θ_{rec} are tested with a FLDA trained on photon and proton simulations.

Finally, the FLDA is trained with the burn sample of data. Depending on the combination of variables used, 1 or 3 events are found above the candidate cut, resulting in an expected number of events from the search sample of data superior to the 16 candidates found in [32]. We also noticed that the selection efficiency obtained

our analysis is higher than that published in [32] which could hint that the choice of the selection criteria is not optimal.

Chapter 8

Conclusion

In the context of the study of neutral astroparticles with energies above 10^{17} eV, the work presented in this manuscript is devoted to the search for photons at ultra high energies (UHE) using the framework provided by the Pierre Auger Observatory in Argentina. By combining a ground network of water Cherenkov detectors (WCD) with fluorescence telescopes (FD), the Observatory studies the extensive air showers (EAS) generated by UHECRs entering the Earth's atmosphere. The main objective of this thesis work was to design a novel analysis to identify UHE photons among the data provided by the surface detector (SD), by implementing a reconstruction procedure for photon-induced showers based on the concept of the universality of EAS. Using the strategy reminded hereafter, we reconstructed the energy E_γ, the core position (x_c, y_c) and X^γ_{max}, the slant depth corresponding to the maximum of the shower development of photon showers, since this parameter is the most precise mas estimator.

The flux of UHECRs is dominated by charged cosmic rays. The search for UHE photons relies on the differences observed in the development of photon-induced EAS with respect to those induced by nuclei: showers generated by photon primaries develop deeper in the atmosphere (higher X_{max}) and the number of muons they contain is less important. The UHE photon search is also confronted to diffuse fluxes of UHE photons, like the GZK cosmogenic flux and the one originating from UHECR interactions in the Milky Way. The latter was estimated in the third chapter of this manuscript and is found to be about 3 orders of magnitude below the latest limits set on UHE photon fluxes.

Although X_{max} and the muon number are robust observables to distinguish photons from nuclei, they are not directly accessible with the SD. Using an universality-based model predicting the intensity and the shape of the signals in the WCDs, the strategy followed in this thesis work was to fix the muon content N_μ, a parameter of the model, to its mean value obtained from simulated photon showers. In consequence, the universality model of EAS followed the average behaviour of photon showers: the energy, core position and X_{max}, which are also parameters of the universality model, were reconstructed performing maximum likelihood fits.

A four-steps reconstruction procedure has been designed. The energy and core position

of photon-induced showers were reconstructed fitting the integrated signals in the WCDs, while X^{γ}_{max} was obtained fitting the signal risetimes. The model of universality provides only the mean values of the integrated signals and risetimes. Therefore, it was necessary determined the probability density functions (PDF) used in the likelihoods, representing the variations around these mean values. The PDF for the integrated signal is a Gaussian function which takes into account two components, electromagnetic and muonic, as the present work demonstrated that it describes better the variations with respect to the case in which only muons were considered. For the risetime, the PDF is also a Gaussian: the risetime uncertainty is obtained from a benchmark parameterised on data and scaled it to the behaviour of photons using photon simulations. Also, the case of preshowering and non-preshowering photons is distinguished by designing two distinct reconstructions, which is a new approach compared to the previous searches for photons above 10^{19} eV. Finally, when applying the reconstruction procedure to photon simulations, the energy resolution is comparable to that of the SD photon search analysis published in 2023, but with an unbiased reconstructed energy for the preshowering photons.

Two new variables, R_{sig} and R_{RT}, were elaborated using the likelihood functions designed in this work and illustrate the probability of a shower to be more photon or proton-like. The obtained X^{γ}_{max} is combined with R_{sig} and R_{RT} in a Fisher Linear Discriminant Analysis (FLDA) to discriminate photon from hadron primaries. Different combinations of X_{max}, R_{sig} and R_{RT} with E_{γ} and the zenith angle θ were tested in the FLDA using proton and photon simulations. The proton contamination above the candidate selection cut is found to be within the uncertainties for the best configurations, although hinting that using E_{γ} should give a better separation. The FLDA was trained on a small ($\sim 2\%$) sample of Auger SD data, the burn sample, for the four best combinations of discriminating variables: 1 or 3 events were found above the candidate cut. The estimated number of expected selected events from the rest of the whole SD data is in the best case of ~ 100, which is higher than the results obtained with the analysis published in 2023 (16 candidates). By computing the photon efficiency, we observed that it is 30% to 50% larger than that in the published analysis. This could hint that the selection criteria applied throughout the analysis are not optimal, in particular the signal threshold of 5 VEM in the selection of WCDs.

Thanks to the reconstruction of photon showers presented in this manuscript, which provides X_{max} and unbiased energy value for both preshowering and non preshowering photon showers, the analysis developed in this work gives encouraging results for the search of UHE photons using the SD with universality. Nevertheless, there is room for improvement to increase its separation power between photon and hadron primaries. Among the possibilities, the likelihood functions could be refined to upgrade the reconstruction performances. For instance, with a better parameterisation of the risetime uncertainty for photon showers, one could expect a better X^{γ}_{max} resolution and discriminating power. Another possibility relies on the method of identification which should be adapted with a selection depending on the photon energy.

The Pierre Auger Observatory is currently being upgraded in the context of the Auger Prime project. The objective is to obtain information on the primary mass of the most

energetic cosmic rays on a shower-by-shower basis to address in particular the question of the origin of UHECRs. Among the ongoing modifications, new scintillator detectors are deployed on top of the WCDs. To accommodate new detectors, the electronics is also upgraded. Combining the different responses to shower particles of the different types of detectors will lead to a better distinction between the electronic and muonic components of the showers, resulting in particular in enhanced performances for the UHE photon searches. The universality principle is not detector-related and if a model predicting the signal in the scintillators was developed, a procedure similar to that presented here could be envisaged in the future.

Traduction française

Introduction

Les astroparticules de haute énergie sont de précieux messagers en provenance du cosmos. Celui a été observé grâce photons depuis les commencements de l'astronomie moderne, d'abord dans le domaine optique visible, puis en élargissant la gamme vers les infrarouges et les ultraviolets. La détection des photons d'ultra haute énergie (UHE) joue un rôle crucial dans la compréhension des phénomènes astrophysiques extrêmes. À ce jour, les photons les plus énergétiques détectés atteignent des énergies dans la gamme du PeV, et la recherche d'émission de photons à plus haute énergie, dans un domaine où leur absorbtion est moins probable, continue.

La recherche de particules neutres à UHE (dans la gamme EeV) est très importante dans le cadre de l'astronomie multi-messagers: comme ces particules ne sont pas déviées sur leur parcours jusqu'à la Terre par les champs magnétiques galactiques et extra-galactiques, elles peuvent fournir des informations précieuses sur la nature des sources de rayons cosmiques d'ultra haute énergie (RCUHE). En effet, bien que les connaissances sur les RCUHE se soint grandement améliorées dans les dernières décennies grâce à la contribution des observatoires de RCUHE tel celui exploité par la Collaboration Pierre Auger, la question de leur origine et de la façon dont les RCs sont accélérés à de telles énergies reste une des questions principales les concernant. On pense que ces particules neutres sont produites avec les RCUHE dans l'environnement des sources ou durant leur propagation. Elles ouvrent une fenêtre sur une nouvelle physique au delà du Modèle Standard, car plusieurs scénarios prédisent leur production suite à la désintégration de particules lourdes toujours inconnues, ou lors de processus sans accélération.

Dans ce contexte, les observatoires de RCUHE, et en particulier l'Observatoire Pierre Auger situé en Argentine, cherchent ces messagers neutres dans leurs données largement dominées par les rayons cosmiques chargés. Ils détectent les gerbes atmosphériques produites par l'interaction des RCUHE dans l'atmosphère. L'Observatoire Pierre Auger est le plus grand observatoire de RCUHE. Il utilise un mode de détection hybride constitué d'un réseau de détecteurs au sol et de plusieurs télescopes de fluorescence, ce qui permet de reconstuire les propriétés du rayon cosmique primaire. Les photons UHE peuvent être identifiés car les gerbes atmosphériques qu'ils génèrent possèdent des caractéristiques différentes de celles produites par des rayons cosmiques chargés, permettant ainsi de développer des analyses discriminant les photons des hadrons. Dans la recherche de photons UHE produits par des sources astrophysiques ou par de nouveaux processus physiques encore méconnus, les flux diffus de photons de haute énergie pourraient constituer un "bruit de fond" cachant l'émission localisée de photons. Ils doivent donc être pris en compte au même titre que l'absorption des photons qui résulte de leur interaction avec différents champs de photons présents dans l'univers et limitant l'horizon de détection. Au vu de l'absence de détection au delà de la gamme des PeV, des limites supérieures sur les flux de photons UHE ont été déterminées par les observatoires de rayons cosmiques, et ont permis d'écarter plusieurs modèles de production de RCUHE dans des processus sans accélération.

Le travail présenté dans ce manuscrit de thèse entre dans le contexte de la recherche de photons UHE, et est principalement consacré à leur identification avec les données fournies par le détecteur de surface de l'Observatoire Pierre Auger. L'analyse repose sur le concept de l'universalité des gerbes atmosphériques à ultra haute énergie. Le nombre très important de particules secondaires dans ces gerbes résulte en une homogénisation des propriétés de la gerbe, qui peut alors être décrite par quelques paramètres macroscopiques. En élaborant une reconstruction des gerbes générées par des photons basée sur ce principe, on estime la profondeur atmosphérique correspondant au maximum de développment de la gerbe, une observable robuste pour discriminer les photons des hadrons. Cette observable est accessible directement avec les données hybrides, mais ces données ne donnent accès qu'à peu de statistiques, ce qui rend impossible une exploration efficace aux plus hautes énergies. La profondeur reconstruite de la gerbe est ensuite combinée, dans une analyse multivariée, à deux autres variables discriminantes élaborées dans ce travail. L'objectif est d'améliorer les perfomances de la recherche actuelle de photons UHE avec le détecteur de surface.

Ce manuscrit est divisé en six chapitres. Le premier introduit l'astronomie multi-messagers à ultra haute énergie, au delà de 10^{17} eV, en mettant l'accent sur les rayons cosmiques. L'importance de la recherche de messagers neutres pour identifier les sources de RCUHE est soulignée, et l'état de l'art de la recherche de particules neutres UHE est présenté. Le second chapitre présente l'estimation du flux diffus de photons et neutrinos UHE provenant des interactions des RCUHE avec les gaz interstellaires de la Voie Lactée. Le troisième chapitre est consacré aux recherches de photons UHE effectuées à l'Observatoire Pierre Auger, en particulier avec le détecteur de surface. Les spécificités des gerbes induites par des photons par rapport à celles générées par des hadrons qui sont exploitées dans la recherche de photons UHE sont décrites, et les différentes analyses effectuées par la Collaboration Pierre Auger sont présentées. Le quatrième chapitre présente le concept d'universalité des gerbes atmosphériques utilisé dans ce travail pour élaborer une nouvelle reconstruction des gerbes induites par des photons, ainsi que les modèles prédisant les signaux dans les détecteurs de surface de l'Observatoire. Le cinquième chapitre explique la procédure élaborée pour implémenter la reconstruction basée sur l'universalité qui fournit des variables appropriées pour identifier les photons collectés par le détecteur de surface. Enfin, la reconstruction est appliquée sur des simulations de photons et de protons, et, grâce aux informations extraites de la reconstruction, trois variables discriminantes photon-hadron sont combinées dans une analyse multivariée décrite dans le dernier chapitre. Les résultats obtenus après l'application de l'analyse sur un petit échantillon de données Auger sont commentés.

Conclusion

Dans le cadre de l'étude des astroparticules neutres possédant des énergies au delà de 10^{17} eV, le travail présenté dans ce manuscript est consacré à la recherche de photons à ultra haute énergie (UHE), en utilisant les outils fournis par l'Observatoire Pierre Auger situé Argentine. En combinant un réseau de détecteurs Cherenkov à eau ("WCD") au sol avec des télescopes de fluorescence ("FD"), l'Observatoire permet d'étudier les gerbes atmosphériques générées par l'interaction des rayons cosmiques UHE (RCUHE) dans l'atmosphère terrestre. L'objectif de cette thèse fut de développer une nouvelle méthode d'analyse d'identification des photons UHE dans les données fournies par le détecteur de surface ("SD"), en implémentant une procédure de reconstruction des gerbes générées par des photons s'appuyant sur le principe d'universalité. En utilisant une stratégie rappelée dans la suite, nous avons reconstruit l'énergie E_γ, la position du cœur de gerbe (x_c, y_c), ainsi que X^γ_{max}, la pronfondeur atmosphérique correspondant au maximum de développement de la gerbe, qui est le paramètre le plus discriminant pour la nature du rayon cosmique.

Le flux des RCUHE est dominé par les rayons cosmiques chargés. La recherche de photons UHE repose sur les différences observées dans le développement des gerbes induites par des photons, en comparaison à celles générées par des noyaux: les gerbes produites par des photons se développent plus pronfondément dans l'atmosphère (grands X_{max}), et le nombre de muons qu'elles contiennent est moins important. La recherche de photons UHE est également confrontée à des flux diffus de photons UHE, comme le flux cosmogénique GZK et celui provenant de l'interaction des RCUHE dans la Voie Lactée. Ce dernier a été estimé dans le troisième chapitre, et se trouve être trois ordres de grandeur en dessous des dernières limites supérieures posées sur les flux des photons UHE.

Bien que X_{max} et le nombre de muons soient des observables robustes pour distinguer les photons des noyaux, elles ne sont pas directement accessibles avec le SD. En utilisant un modèle basé sur l'universalité des gerbes qui prédit l'intensité et la forme des signaux dans les WCDs, la stratégie fut de fixer le contenu en muon N_μ, un paramètre du modèle, à sa valeur moyenne pour des gerbes de photon que l'on a obtenue à l'aide de simulations Monte-Carlo. En conséquence, le modèle d'universalité a suivi le comportement moyen d'une gerbe de photon: l'énergie, la position du cœur et X_{max} ont été reconstruits en effectuant des fits de maximum de vraisemblance.

Une procédure de reconstruction en quatre étapes a été élaborée. L'énergie et la position du cœur ont été reconstruites en fittant les valeurs des signaux dans les WCDs, alors que X_{max} a été obtenu en fittant les "risetimes" (temps de montée) de ces signaux. Le modèle d'universalité fournissant seulement les valeurs moyennes des signaux et risetimes, il a été nécessaire de déterminer les fonctions de densité de probabilité ("PDF") utilisées dans les fonctions de vraisemblance, représentant les variations autour des valeurs moyennes. La PDF pour les signaux est une Gausienne prenant en compte deux composantes, électromagnetique et muonique, car ce travail a pu montrer que cela décrit mieux les fluctuations que la seule considération des muons. Pour le risetime, la PDF est également une Gausienne: nous avons utilisé l'incertitude fournie par une référence

paramétrisée sur des données, et l'avons adaptée au comportement des photons en se servant de simulations. De plus, les cas des "preshowering" photons a été distingué des "non-preshowering" en développant deux reconstructions distinctes, ce qui constitut une nouvelle approche par rapport aux autres recherches de photons au delà de 10^{19} eV. Enfin, en appliquant la procédure de reconstruction à des simulations de gerbes de photons, la résolution en énergie est comparable à celle de l'analyse publiée en 2023, avec une reconstruction non biasiée de l'énergie des "preshowering" photons.

Deux nouvelles variables, R_{sig} et R_{RT}, furent élaborées en utilisant les fonctions de vraisemblance développées dans ce travail. Elles illustrent la probabilité d'une gerbe à se rapprocher plus d'un comportement de photon que de proton. Le X^{γ}_{max} obtenu a été combiné à R_{sig} et R_{RT} dans une Analyse Linéraire Discriminante de Fisher ("FLDA") pour discriminer les photons des hadrons. Différentes combinaisons de X^{γ}_{max}, R_{sig}, et R_{RT} avec E_{γ} et l'angle zénithal θ ont été testées dans la FLDA avec des simulations de photons et de protons. La contamination en protons au delà du critère de sélection des candidats était contenue dans les intervalles d'incertitude dans le cas des meilleures configurations, suggérant néanmoins que l'utilisation de E_{γ} donnerait une meilleure séparation. La FLDA a été entraînée ensuite sur un échantillon réduit de données Auger SD ($\sim 2\%$), le "burn sample", pour les quatres meilleures combinaisons de variables discriminantes: 1 à 3 évènements furent sélectionnés. Le nombre estimé de gerbes selectionnées attendu dans le reste des données est dans le meilleur des cas de ~ 100, ce qui est supérieur aux résultats obtenus dans l'analyse publiée en 2023 (16 candidats). En calculant l'efficacité pour les photons, nous avons constaté qu'elle était de 30 à 50% plus importante que celle rapportée dans l'analyse publiée. Cela pourrait siginifier que les critères de selection appliqués tout au long de la procédure ne sont pas optimaux, en particulier le seuil de 5 VEM sur les signaux des WCDs.

Grâce à la reconstruction des gerbes de photon présentée dans ce manuscrit, qui donne accès à X_{max} et a énergie non biaisée pour les photons "preshowering" et "non-preshowering", l'analyse fournit des résulats encourageants pour la recherche de photons UHE avec le SD et l'univesalité. Néanmoins, il reste de la place pour des améliorations dans le cadre du pouvoir de séparation entre les photons et les noyaux. Parmi les possibilités, la détermination des fonctions de vraisemblance pourrait être affinée dans le but d'améliorer les perfomances de reconstruction. Par exemple, une meilleure paramétrisation de l'incertitude sur le risetime pour les gerbes de photons permettrait une meilleure résolution de X^{γ}_{max} et un donc une augmentation du pouvoir discriminant. Une autre possibilité serait d'adapter la méthode d'indentification avec une dépendance sur l'énergie des photons.

L'Observatoire Pierre Auger en cours d'amélioration dans le cadre du projet Auger Prime. L'objectif est d'obtenir des informations sur la nature des rayons cosmiques aux plus hautes énergies pour avancer sur la question de l'origine des RCUHE. Parmi les modifications en cours, de nouveaux détecteurs à scintillation sont déployés sur le dessus des WCDs, accompagnés d'une nouvelle électronique. Grâce aux réponses différentes engendrées par les deux types de détecteurs, l'accès à une meilleure distinction entre la composante electromagnétique et muonique de la gerbe est permis, ce qui entraîne en

particulier de meilleures performances pour la recherche de photons UHE. Le principe d'universalité ne dépendant pas du détecteur, si une paramétrisation prédisant les signaux dans les scintillateurs été développée, une procédure similaire à celle présentée dans cette thèse pourrait être envisagée dans le futur.

Remerciements

Pour conclure ce manuscrit, je tiens à exprimer ma reconnaissance envers Corinne Bérat, pour sa direction éclairée tout au long de ces trois années de thèse. Son expertise, son soutien continu et son engagement envers mon travail ont été plus qu'essentiels. Merci beaucoup à toi Corinne pour cet accompagnement, j'ai eu beaucoup de chance de t'avoir comme directrice.

Un grand merci à Carla Bleve, ma co-directrice, pour son expertise et son aide précieuse. Merci aussi à François Montanet pour ses bon conseils lors des réunions hebdomadaires de l'équipe.

Je tiens à remercier également mon jury de thèse: Yvonne Becherini, Anne Stutz, Olivier Deligny, Damien Dornic, et Laurent Derome, pour leurs retours, leur intérêt et leur expertise sur mon travail.

Mes remerciements vont aussi à l'ensemble de la Collaboration Pierre Auger au sein de laquelle j'ai pu m'épanouir pendant ces trois années et dont les échanges ont été une expérience enrichissante.

Bien sûr, merci à toute ma famille (Papa, Maman, Alice et les tous les autres), pour leur soutient inconditionnel et pour avoir bien souvent aidé gérer le stresse à ma place. Enfin, merci à tous mes amis, Vickie, Marine, Alexandre, Lucas et tous les autres, qui même s'ils ne comprenaient pas ce que je faisais, ont été là pour moi.

Bibliography

[1] V. F. Hess. "Über Beobachtungen der durchdringenden Strahlung bei sieben Freiballonfahrten". In: *Phys. Z.* 13 (1912), p. 1084.

[2] D. Pacini. "La radiazione penetrante alla superficie ed in seno alle acque". In: *Il Nuovo Cimento* 3.1 (1912), p. 93.

[3] R. A. Milikan. "High frequency rays of cosmic origin". In: *Proceedings of the National Academy of Sciences* 12.1 (1926), p. 48. DOI: https://doi.org/10.1073/pnas.12.1.48.

[4] J. Clay et ak. "Results of the Dutch Cosmic Ray Expedition 1933: II. The magnetic latitude effect of cosmic rays a magnetic longitude effect". In: *Physica* 1.(7-12) (1934), p. 829. DOI: https://doi.org/10.1016/S0031-8914(34)80277-7.

[5] P. Auger et al. "Extensive Cosmic-Ray Showers". In: *Rev. Mod. Phys.* 11 (1939), p. 288. DOI: https://doi.org/10.1103/RevModPhys.11.288.

[6] W. Heitler. "The quantum theory of radiation". In: *Courier Corporation* 3rd ed. (1954), p. 386.

[7] J. Linsley. "Evidence for a Primary Cosmic-Ray Particle with Energy 10^{20} eV". In: *Phys. Rev. Lett.* 10 (1963), p. 146. DOI: https://doi.org/10.1103/PhysRevLett.10.146.

[8] A. A. Penzias and R. W. Wilson. "A Measurement of Excess Antenna Temperature at 4080 Mc/s." In: *The Astrophysical Journal* 142 (1965), p. 419. DOI: https://doi.org/10.1086/148307.

[9] G. T. Zatsepin and V. A. Kuz'min. "Upper limit of the spectrum of cosmic rays". In: *Journal of Experimental and Theoretical Physics Letters* 4.3 (1966), p. 78.

[10] K. Greisen. "End to the Cosmic-Ray Spectrum?" In: *Phys. Rev. Lett.* 16 (1966), p. 748. DOI: https://doi.org/10.1103/PhysRevLett.16.748.

[11] D. M. Edge et al. "The cosmic ray spectrum at energies above 10^{17} eV". In: *J. Phys. A: Math. Nucl. Gen.* 6 (1973), p. 1612. DOI: https://doi.org/10.1088/0305-4470/6/10/019.

[12] The High Resolution Fly's Eye Collab. "Observation of the Ankle and Evidence for a High-Energy Break in the Cosmic Ray Spectrum". In: *Phys. Lett. B* 619 (2005), p. 271. DOI: https://doi.org/10.1016/j.physletb.2005.05.064.

[13] M. Takeda et al. "Energy determination in the Akeno Giant Air Shower Array experiment". In: *Astroparticle Physics* 19.4 (2003), p. 447. DOI: https://doi.org/10.1016/S0927-6505(02)00243-8.

[14] M. Aliguar et al. "The Alpha Magnetic Spectrometer (AMS) on the international space station: Part II — Results from the first seven years". In: *Phys. Rept.* 894 (2021), p. 1. DOI: https://doi.org/10.1016/j.physrep.2020.09.003.

[15] R.L. Workman et al. (Particle Data Group). "The Review of Particle Physics". In: *Prog. Theor. Exp. Phys.* (2022), p. 083C01.

[16] G. V. Kulikov and G. B. Khristiansen. "On the Size Spectrum of Extensive Air Showers". In: *Zh. Exp. Teor. Fiz.* 35 (1958), p. 635.

[17] J. R. Hörandel. "The Composition of cosmic rays at the knee". In: *Nuovo Cim. B* 6-8 (2005), p. 825. DOI: https://doi.org/10.1393/ncb/i2005-10124-2.

[18] W. D. Apel et al. (KASCADE-Grande Collaboration). "Kneelike Structure in the Spectrum of the Heavy Component of Cosmic Rays Observed with KASCADE-Grande". In: *Phys. Rev. Lett.* 107 (2011), p. 171104. DOI: https://doi.org/10.1103/PhysRevLett.107.171104.

[19] A. Aab et al. (The Pierre Auger Collaboration). "Measurement of the cosmic-ray energy spectrum above 2.5 10^{18} eV using the Pierre Auger Observatory". In: *Phys. Rev. D* 102 (2020), p. 062005. DOI: https://doi.org/10.1103/PhysRevD.102.062005.

[20] A. Aab et al. (The Pierre Auger Collaboration). "Probing the origin of ultra-high-energy cosmic rays with neutrinos in the EeV energy range using the Pierre Auger Observatory". In: *Journal of Cosmology and Astroparticle Physics* 10 (2019), p. 022. DOI: https://doi.org/10.1088/1475-7516/2019/10/022.

[21] M. Niechciol for The Pierre Auger Collaboration. "Searches for Ultra-High-Energy Photons at the Pierre Auger Observatory". In: *38th International Cosmic Ray Conference* (2023).

[22] M. G. Aartsen et al. (The IceCube Collaboration). "Differential limit on the EHE cosmic neutrino flux in the presence of astrophysical background from nine years of IceCube data". In: *Phys. Rev. D* 98 (2018), p. 062003. DOI: https://doi.org/10.1103/PhysRevD.98.062003.

[23] P. W. Gorham et al. (ANITA Collaboration). "Constraints on the diffuse high-energy neutrino flux from the third flight of ANITA". In: *Phys. Rev. D* 98 (2018), p. 022001. DOI: https://doi.org/10.1103/PhysRevD.98.022001.

[24] A. Aab et al. "A search for point sources of EeV photons". In: *The Astrophysical Journal* 789 (2014), p. 160. DOI: https://doi.org/10.1088/0004-637X/789/2/160.

[25] R. U. Abbasi et al. "Search for point sources of ultra-high energy photons with the Telescope Array surface detector". In: *Monthly Notices of the Royal Astronomical Society* 492.3 (2020), p. 3984. DOI: https://doi.org/10.1093/mnras/stz3618.

[26] A. Aab et al. (The Pierre Auger Collaboration). "Limits on point-like sources of ultra-high-energy neutrinos with the Pierre Auger Observatory". In: *Journal of Cosmology and Astroparticle Physics* 11 (2019), p. 004. DOI: https://doi.org/10.1088/1475-7516/2019/11/004.

[27] M. G. Aartsen et al. (The IceCube Collaboration). "All-sky Search for Time-integrated Neutrino Emission from Astrophysical Sources with 7 yr of IceCube Data". In: *The Astrophysical Journal* 835 (2017), p. 151. DOI: https://doi.org/10.3847/1538-4357/835/2/151.

[28] A. Albert et al. (ANTARES Collaboration). "First all-flavour neutrino pointlike source search with the ANTARES neutrino telescope". In: *Phys. Rev. D* 96 (2017), p. 082001. DOI: https://doi.org/10.1103/PhysRevD.96.082001.

[29] A. Aab et al. (The Pierre Auger Collaboration). "A targeted search for point sources of EeV photons with the Pierre Auger Observatory". In: *The Astrophysical Journal Letters* 837 (2017), p. L25. DOI: https://doi.org/10.3847/2041-8213/aa61a5.

[30] B. P. Abbott et al. (LIGO Scientific Collaboration and Virgo Collaboration). "Observation of Gravitational Waves from a Binary Black Hole Merger". In: *Phys. Rev. Lett.* 116 (2016), p. 061102. DOI: https://doi.org/10.1103/PhysRevLett.116.061102.

[31] A. Abdul Halim et al. (The Pierre Auger Collaboration). "Search for UHE Photons from Gravitational Wave Sources with the Pierre Auger Observatory". In: *The Astrophysical Journal* 952 (2023), p. 91. DOI: https://doi.org/10.3847/1538-4357/acc862.

[32] P. Abreu et al. (The Pierre Auger Collaboration). "Search for photons above 10^{19} eV with the surface detector of the Pierre Auger Observatory". In: *Journal of Cosmology and Astroparticle Physics* 05 (2023), p. 021. DOI: https://doi.org/10.1088/1475-7516/2023/05/021.

[33] A. Albert et al. "Search for High-energy Neutrinos from Binary Neutron Star Merger GW170817 with ANTARES, IceCube, and the Pierre Auger Observatory". In: *Astrophysical Journal Letters* 850 (2017), p. L35. DOI: https://doi.org/10.3847/2041-8213/aa9aed.

[34] A. Aab et al. (The Pierre Auger Collaboration). "A Search for Ultra-high-energy Neutrinos from TXS0506+056 Using the Pierre Auger Observatory". In: *The Astrophysical Journal* 902 (2020), p. 105. DOI: https://doi.org/10.3847/1538-4357/abb476.

[35] A. Aab et al. (The Pierre Auger Collaboration). "A Targeted Search for Point Sources of EeV Neutrons". In: *The Astrophysical Journal Letters* 789 (2014), p. L34. DOI: https://doi.org/10.1088/2041-8205/789/2/L34.

[36] E. Fermi. "On the origin of the cosmic radiation". In: *Phys. Rev.* 75 (1949), p. 1169. DOI: https://doi.org/10.1103/PhysRev.75.1169.

[37] M. Bustamante et al. "High-energy cosmic-ray acceleration". In: *2009 CERN - Latin-American School of High-Energy Physics* 1 (2010), p. 533. DOI: https://doi.org/10.5170/CERN-2010-001.533.

[38] A. M. Hillas. "The Origin of Ultra-High-Energy Cosmic Rays". In: *Annual Review of Astronomy and Astrophysics* 22 (1984), p. 425. DOI: https://doi.org/10.1146/annurev.aa.22.090184.002233.

[39] R. Alves Batista et al. "Open Questions in Cosmic-Ray Research at Ultrahigh Energies". In: *7th High Energy Phenomena in Relativistic Outflows* 6 (2019). DOI: https://doi.org/10.3389/fspas.2019.00023.

[40] F. M. Rieger. "UHE Cosmic Rays and AGN Jets". In: *Frontiers in Astronomy and Space Sciences* 6 (2019). DOI: https://doi.org/10.48550/arXiv.1911.04171.

[41] L. A. Anchordoqui. "Acceleration of ultrahigh-energy cosmic rays in starburst superwinds". In: *Phys. Rev. D* 97 (2018), p. 063010. DOI: https://doi.org/10.1103/PhysRevD.97.063010.

[42] P. Abreu et al. (The Pierre Auger Collaboration). "Arrival Directions of Cosmic Rays above 32 EeV from Phase One of the Pierre Auger Observatory". In: *The Astrophysical Journal* 935 (2022), p. 170. DOI: https://doi.org/10.3847/1538-4357/ac7d4e.

[43] E. Waxman. "Cosmological Gamma-Ray Bursts and the Highest Energy Cosmic Rays". In: *Phys. Rev. Lett.* 75 (1995), p. 386. DOI: https://doi.org/10.1103/PhysRevLett.75.386.

[44] M. Vietri. "The Acceleration of Ultra–High-Energy Cosmic Rays in Gamma-Ray Bursts ". In: *the Astrophysical Journal* 453 (1995), p. 883. DOI: https://doi.org/10.1086/176448.

[45] K. Koreta. "Pulsars: a promising source for high and ultrahigh energy cosmic rays". In: *Nuclear Physics B - Proceedings Supplements* 256 (2014), p. 131. DOI: https://doi.org/10.1016/j.nuclphysbps.2014.10.016.

[46] B. T. Zhang et al. "High-energy cosmic ray nuclei from tidal disruption events: Origin, survival, and implications". In: *Phys. Rev. D* 96 (2017), p. 063007. DOI: https://doi.org/10.1103/PhysRevD.96.063007.

[47] P. S. Coppi and F. A. Aharonian. "Constraints on the Very High Energy Emissivity of the Universe from the Diffuse GeV Gamma-Ray Background". In: *The Astrophysical Journal* 487 (1997), p. L9. DOI: https://doi.org/10.1086/310883.

[48] V. Berezinsky et al. "Ultrahigh Energy Cosmic Rays without Greisen-Zatsepin-Kuzmin Cutoff ". In: *Phys. Rev. Lett.* 79 (1997), p. 4302. DOI: https://doi.org/10.1103/PhysRevLett.79.4302.

[49] R. P. L. Azevedo and C. J. A. P. Martins. "Cosmic strings and other topological defects in nonscaling regimes". In: *Phys. Rev. D.* 95 (2017), p. 043537. DOI: https://doi.org/10.1103/PhysRevD.95.043537.

[50] Z. Fodor et al. "Z-Burst Scenario for the Highest Energy Cosmic Rays". In: *Conference on Physics Beyond the Standard Model: Beyond the Desert 02* (2002). DOI: https://doi.org/10.48550/arXiv.hep-ph/0210123.

[51] O. E. Kalashev and M. Yu. Kuznetsov. "Constraining heavy decaying dark matter with the high energy gamma-ray limits". In: *Phys. Rev. D* 94 (2016), p. 063535. DOI: https://doi.org/10.1103/PhysRevD.94.063535.

[52] M. Kachelrieß et al. "Heavy decaying dark matter and IceCube high energy neutrinos". In: *Phys. Rev. D* 98 (2018), p. 083016. DOI: https://doi.org/10.1103/PhysRevD.98.083016.

[53] P. Abreu et al. (The Pierre Auger Collaboration). "Cosmological implications of photon-flux upper limits at ultrahigh energies in scenarios of Planckian-interacting massive particles for dark matter". In: *Phys. Rev. D* 107 (2023), p. 042002. DOI: https://doi.org/10.1103/PhysRevD.107.042002.

[54] A. Bobrikova et al. "Predicting the UHE photon flux from GZK-interactions of hadronic cosmic rays using CRPropa 3". In: *37th International Cosmic Ray Conference* 395 (2021), p. 449. DOI: 10.22323/1.395.0449.

[55] C. Bérat et al. "Diffuse Flux of Ultra-high-energy Photons from Cosmic-Ray Interactions in the Disk of the Galaxy and Implications for the Search for Decaying Super-heavy Dark Matter". In: *The Astrophysical Journal* 929 (2022), p. 55. DOI: https://doi.org/10.3847/1538-4357/ac5cbe.

[56] Sangjin Lee. "Propagation of extragalactic high energy cosmic and γ rays". In: *Phys. Rev. D* 58 (1998), p. 043004. DOI: https://doi.org/10.1103/PhysRevD.58.043004.

[57] E. W. Mayotte for the Pierre Auger Collaboration. "Measurement of the mass composition of ultra-high-energy cosmic rays at the Pierre Auger Observatory". In: *38th International Cosmic Ray Conference* 444 (2023), p. 365. DOI: https://doi.org/10.22323/1.444.0365.

[58] A. Aab et al. (The Pierre Auger Collaboration). "Cosmic-ray anisotropies in right ascension measured by the Pierre Auger Observatory". In: *The Astrophysical Journal* 891 (2020), p. 142. DOI: https://doi.org/10.3847/1538-4357/ab7236.

[59] A. Aab et al. (the Pierre Auger Collaboration). "The energy spectrum of cosmic rays beyond the turn-down around 10^{17} eV as measured with the surface detector of the Pierre Auger Observatory". In: *Eur. Phys. J. C* 81 (2021), p. 966. DOI: https://doi.org/10.1140/epjc/s10052-021-09700-w.

[60] J. Bellido for The Pierre Auger Collaboration. "Depth of maximum of air-shower profiles at the Pierre Auger Observatory: Measurements above $10^{17.2}$ eV and Composition Implications". In: *35th International Cosmic Ray Conference* 301 (2018), p. 506. DOI: https://doi.org/10.22323/1.301.0506.

[61] T. Pierog et al. "EPOS LHC: Test of collective hadronization with data measured at the CERN Large Hadron Collider". In: *Phys. Rev. C* 92 (2015), p. 034906. DOI: https://doi.org/10.1103/PhysRevC.92.034906.

[62] F. Riehn et al. "The hadronic interaction model Sibyll 2.3 and Feynman scaling". In: *35th International Cosmic Ray Conference* 301 (2017), p. 301. DOI: https://doi.org/10.22323/1.301.0301.

[63] S. Ostapchenko. "QGSJET-II: physics, recent improvements, and results for air showers". In: *International Symposium on Very High Energy Cosmic Ray Interactions* 52 (2013), p. 02001. DOI: https://doi.org/10.1051/epjconf/20135202001.

[64] T. M. Dame et al. "The Milky Way in molecular clouds: A New complete CO survey". In: *The Astrophysical Journal* 547 (2001), p. 792. DOI: https://doi.org/10.1086/318388.

[65] P. Lipari et S. Vernetto. "Diffuse Galactic gamma ray flux at very high energy". In: *Phys. Rev. D* 98 (2018), p. 043003. DOI: https://doi.org/10.1103/PhysRevD.98.043003.

[66] G. Jóhannesson et al. "The Three-Dimensional Spatial Distribution of Interstellar Gas in the Milky Way: Implications for Cosmic Rays and High-Energy Gamma-Ray Emissions". In: *The Astrophysical Journal* 856 (2018), p. 45. DOI: https://doi.org/10.3847/1538-4357/aab26e.

[67] R. Ulrich et al. "Cosmic Ray Monte Carlo Package, CRMC". In: (2021). DOI: https://doi.org/10.5281/zenodo.4558706.

[68] YU A. Fomin et al. "Constraints on the flux of $\sim (10^{16} - 10^{17.5})$ eV cosmic photons from the EAS-MSU muon data". In: *Phys. Rev. D* 95 (2017), p. 123011. DOI: https://doi.org/10.1103/PhysRevD.95.123011.

[69] W. D. Apel et al. "KASCADE-Grande Limits on the Isotropic Diffuse Gamma-Ray Flux between 100 TeV and 1 EeV". In: *The Astrophysical Journal* 848 (2017), p. 1. DOI: https://doi.org/10.3847/1538-4357/aa8bb7.

[70] O. Kalashev et al. for the Telescope Array Collaboration. "Telescope Array search for EeV photons". In: *37th International Cosmic Ray Conference* 395 (2021), p. 864. DOI: https://doi.org/10.22323/1.395.0864.

[71] P. Savina for the Pierre Auger Collaboration. "A search for ultra-high-energy photons at the Pierre Auger Observatory exploiting air-shower universality". In: *37th International Cosmic Ray Conference* 395 (2021), p. 373. DOI: 10.22323/1.395.0373.

[72] V. A. Kuzmin and V. A. Rubakov. "Ultrahigh-energy cosmic rays: A Window to postinflationary reheating epoch of the universe?" In: *Phys. Atom. Nucl.* 61.6 (1998), p. 1028. DOI: https://doi.org/10.48550/arXiv.astro-ph/9709187.

[73] R. Aloisio et al. "Status of superheavy dark matter". In: *Phys. Rev. D* 74 (2006), p. 023516. DOI: https://doi.org/10.1103/PhysRevD.74.023516.

[74] J. F. Navarro et al. "The Structure of Cold Dark Matter Halos". In: *The Astrophysical Journal* 462 (1996), p. 563. DOI: https://doi.org/10.1086/177173.

[75] R. Aloisio et al. "Ultra high energy cosmic rays spectra in top-down models". In: *Nucl. Phys. B* 136 (2004), p. 319. DOI: https://doi.org/10.1016/j.nuclphysbps.2004.10.023.

[76] Z. Cao et al. "Ultrahigh-energy photons up to 1.4 petaelectronvolts from 12 -ray Galactic sources". In: *Nature* 594 (2021), p. 33. DOI: https://doi.org/10.1038/s41586-021-03498-z.

[77] B. Rossi. "Über die Eigenschaften der durchdringenden Korpuskularstrahlung im Meeresniveau". In: *Zeitschrift für Physik* 82 (1933), p. 151. DOI: https://doi.org/10.1007/BF01341486.

[78] W. Bothe. "Zur Vereinfachung von Koinzidenzz ahlungen". In: *Z. Phys.* 59 (1929), p. 1.

[79] H. Geiger and W. Müller. " Elektronenzählrohr zur Messung schwächster Aktivitäten ". In: *Die Naturwissenschaften* 16 (1928), p. 617. DOI: https://doi.org/10.1007/BF01494093.

[80] H. Bethe and W. Heitler. "On the Stopping of Fast Particles and on the Creation of Positive Electrons". In: *Proc. Roy. Soc. A* 146 (1934), p. 83. DOI: https://doi.org/10.1098/rspa.1934.0140.

[81] H. Bhabha and W. Heitler. "The passage of last electrons and the theory of cosmic showers". In: *Proc. Roy. Soc. A* 159 (1937), p. 432. DOI: https://doi.org/10.1098/rspa.1937.0082.

[82] J. F. Carlson and J. R. Oppenheimer. "On Multiplicative Showers". In: *Phys. Rev.* 51 (1937), p. 220. DOI: https://doi.org/10.1103/PhysRev.51.220.

[83] E. Regener and G. Pfotzer. "Vertical intensity of cosmic rays by treefold coincidences in the stratosphere". In: *Nature* 136 (1935), p. 718. DOI: https://doi.org/10.1038/136718a0.

[84] J. Matthews. "A Heitler model of extensive air showers". In: *Astroparticle Physics* 22 (2005), p. 387. DOI: https://doi.org/10.1016/j.astropartphys.2004.09.003.

[85] D. Heck et al. "CORSIKA: A Monte Carlo Code to Simulate Extensive Air Showers". In: (1998), p. 1. URL: https://hal.in2p3.fr/in2p3-00005094.

[86] P. Billoir. "A sampling procedure to regenerate particles in a ground detector from a "thinned" air shower simulation output." In: *Astroparticle Physics* 30 (2008), p. 270. DOI: https://doi.org/10.1016/j.astropartphys.2008.10.002.

[87] S. Argirò et al. "The offline software framework of the Pierre Auger Observatory". In: *Nuclear Instruments and Methods in Physics Research Section A* 580.3 (2007), p. 1485. DOI: https://doi.org/10.1016/j.nima.2007.07.010.

[88] T. Pierog. "Hadronic Interactions and Air Showers: Where Do We Stand?" In: *International Symposium on Very High Energy Cosmic Ray Interactions* 208 (2019), p. 02002. DOI: https://doi.org/10.1051/epjconf/201920802002.

[89] W. R. Nelson et al. "EGS4 code system". In: (1985). URL: https://www.osti.gov/biblio/6137659.

[90] G. Battistoni et al. "Overview of the FLUKA code". In: *Annals of Nuclear Energy* 82 (2015), p. 10. DOI: https://doi.org/10.1016/j.anucene.2014.11.007.

[91] M. Bleicher et al. "Relativistic hadron-hadron collisions in the ultra-relativistic quantum molecular dynamics model". In: *Journal of Physics G: Nuclear and Particle Physics* 25 (1999), p. 1859. DOI: https://doi.org/10.1088/0954-3899/25/9/308.

[92] R. S. Fletcher et al. "Sibyll: An event generator for simulation of high energy cosmic ray cascades". In: *Phys. Rev. D* 50 (1994), p. 5710. DOI: https://doi.org/10.1103/PhysRevD.50.5710.

[93] K-H. Kampert and M. Unger. "Measurements of the Cosmic Ray Composition with Air Shower Experiments". In: *Astroparticle Physics* 35.10 (2012), p. 660. DOI: https://doi.org/10.1016/j.astropartphys.2012.02.004.

[94] T. Abu-Zayyad et al. "Evidence for Changing of Cosmic Ray Composition between 10^{17} and 10^{18} eV from Multicomponent Measurements". In: *Phys. Rev. Lett.* 84 (2000), p. 4276. DOI: https://doi.org/10.1103/PhysRevLett.84.4276.

[95] A. G. Bogdanov et al. "Investigation of the properties of the flux and interaction of ultrahigh-energy cosmic rays by the method of local-muon-density spectra". In: *Physics of Atomic Nuclei* 73 (2010), p. 1852. DOI: https://doi.org/10.1134/S1063778810110074.

[96] A. G. Bogdanov et al. "Investigation of very high energy cosmic rays by means of inclined muon bundles". In: *Astroparticle Physics* 98 (2018), p. 13. DOI: https://doi.org/10.1016/j.astropartphys.2018.01.003.

[97] J.A. Bellido et al. "Muon content of extensive air showers: comparison of the energy spectra obtained by the Sydney University Giant Air-shower Recorder and by the Pierre Auger Observatory". In: *Phys. Rev. D* 98 (2018), p. 023014. DOI: https://doi.org/10.1103/PhysRevD.98.023014.

[98] A. Aab et al. (The Pierre Auger Collaboration). "Muons in air showers at the Pierre Auger Observatory: Mean number in highly inclined events". In: *Phys. Rev. D.* 91 (2015), p. 032003. DOI: https://doi.org/10.1103/PhysRevD.91.032003.

[99] R. U. Abbasi et al. (Telescope Array Collaboration). "Study of muons from ultrahigh energy cosmic ray air showers measured with the Telescope Array experiment". In: *Phys. Rev. D* 98 (2018), p. 022002. DOI: https://doi.org/10.1103/PhysRevD.98.022002.

[100] W. D. Apel et al. (KASCADE-Grande Collaboration). "Probing the evolution of the EAS muon content in the atmosphere with KASCADE-Grande". In: *Astroparticle Physics* 95 (2017), p. 25. DOI: https://doi.org/10.1016/j.astropartphys.2017.07.001.

[101] Yu. A. Fomin et al. "No muon excess in extensive air showers at 100-500 PeV primary energy: EAS-MSU results". In: *Astroparticle Physics* 92 (2017), p. 1. DOI: https://doi.org/10.1016/j.astropartphys.2017.04.001.

[102] A. Aab et al. (The Pierre Auger Collaboration). "The Pierre Auger Observatory Upgrade - Preliminary Design Report". In: (2016). DOI: https://doi.org/10.48550/arXiv.1604.03637.

[103] X. Bertou et al. "Calibration of the surface array of the Pierre Auger Observatory". In: *Nucl. Instrum. Meth. A* 568 (2006), p. 839. DOI: https://doi.org/10.1016/j.nima.2006.07.066.

[104] The Pierre Auger Collaboration. "Trigger and Aperture of the Surface Detector Array of the Pierre Auger Observatory". In: *Nucl. Instrum. Meth. A* 613 (2010), p. 29. DOI: https://doi.org/10.1016/j.nima.2009.11.018.

[105] The Pierre Auger Collaboration. "Reconstruction of inclined air showers detected with the Pierre Auger Observatory". In: *Journal of Cosmology and Astroparticle Physics* 8 (2014), p. 19. DOI: https://doi.org/10.1088/1475-7516/2014/08/019.

[106] A. Aab et al. (The Pierre Auger Collaboration). "Reconstruction of Events Recorded with the Surface Detector of the Pierre Auger Observatory". In: *JINST* 15 (2020), p. 10021. DOI: https://doi.org/10.1088/1748-0221/15/10/P10021.

[107] K. Kamata and J. Nishimura. "The Lateral and the Angular Structure Functions of Electron Showers". In: *Progress of Theoretical Physics Supplement* 6 (1958), p. 93. DOI: https://doi.org/10.1143/PTPS.6.93.

[108] K. Greisen. "The extensive air showers". In: *Progress in cosmic ray physics 3.1* (1956).

[109] D. Newton et al. "The Optimum Distance at which to Determine the Size of a Giant Air Shower". In: *Astropart. Phys.* 26.6 (2007), p. 414. DOI: https://doi.org/10.1016/j.astropartphys.2006.08.003.

[110] D. Veberic for the Pierre Auger Collaboration. "Estimation of the Total Signals in Saturated Stations of the Pierre Auger Observatory". In: *33rd International Cosmic Ray Conference* (2013), p. 23. DOI: https://doi.org/10.48550/arXiv.1307.5059.

[111] J. Hersil et al. "Observations of Extensive Air Showers near the Maximum of Their Longitudinal Development". In: *Phys. Rev. Lett.* 6 (1961), p. 22. DOI: https://doi.org/10.1103/PhysRevLett.6.22.

[112] V. Verzi for the Pierre Auger Collaboration. "Measurement of the energy spectrum of ultra-high energy cosmic rays using the Pierre Auger Observatory". In: *36th International Cosmic Ray Conference* 358 (2019), p. 450. DOI: https://doi.org/10.22323/1.358.0450.

[113] The Pierre Auger Collaboration. "The Pierre Auger Cosmic Ray Observatory". In: *Nuclear Instruments and Methods in Physics Research A* 798 (2015), p. 172. DOI: https://doi.org/10.1016/j.nima.2015.06.058.

[114] A. Aab et al. (The Pierre Auger Collaboration). "Data-driven estimation of the invisible energy of cosmic ray showers with the Pierre Auger Observatory". In: *Phys. Rev. D.* 100 (2019), p. 082003. DOI: https://doi.org/10.1103/PhysRevD.100.082003.

[115] The Pierre Auger Collaboration. "Searches for Ultra-High-Energy Photons at the Pierre Auger Observatory". In: *Universe* 8 (2022), p. 579. DOI: https://doi.org/10.3390/universe8110579.

[116] P. Savina for The Pierre Auger Collaboration. "Searching for UHE photons in the EeV range: a two-variable approach exploiting air-shower universality". In: *36th International Cosmic Ray Conference* 358 (2019), p. 414. DOI: https://doi.org/10.22323/1.358.0414.

[117] J. K. Daugherty and A. K. Harding. "Pair production in superstrong magnetic fields. " In: *Astrophysical Journal* 273 (1983), p. 761. URL: https://www.osti.gov/biblio/6050430.

[118] P. Homola et al. " Characteristics of geomagnetic cascading of ultra-high energy photons at the southern and northern sites of the Pierre Auger Observatory ". In: *Astroparticle Physics* 27 (2007), p. 174. DOI: https://doi.org/10.1016/j.astropartphys.2006.10.005.

[119] L.D. Landau et al. "Limits of the Applicability of the Theory of Electron Bremsstrahlung and Pair Production at High Energies ". In: *Akad. Nauk* 32 (1953), p. 535.

[120] N. Krohm. "Search for Ultra-High Energy Photons with the Surface Detector of the Pierre Auger Observatory". In: *PhD Thesis at Wuppertal University* (2017).

[121] The Pierre Auger Collaboration. "Upper limit on the cosmic-ray photon flux above 10^{19} eV using the surface detector of the Pierre Auger Observatory ". In: *Astroparticle Physics* 29.4 (2008), p. 243. DOI: https://doi.org/10.1016/j.astropartphys.2008.01.003.

[122] P. Abreu et al. (The Pierre Auger Collaboration). "A Search for Photons with Energies Above 2×10^{17} eV Using Hybrid Data from the Low-Energy Extensions of the Pierre Auger Observatory". In: *The Astrophysical Journal* 933 (2022), p. 125. DOI: https://doi.org/10.3847/1538-4357/ac7393.

[123] A. Aab et al. (The Pierre Auger Collaboration). "Search for photons with energies above 10^{18} eV using the hybrid detector of the Pierre Auger Observatory". In: *Journal of Cosmology and Astroparticle Physics* 09 (2020), p. 02. DOI: https://doi.org/10.1088/1475-7516/2017/04/009. , and Erratum "Erratum: Search for photons with energies above 10^{18} eV using the hybrid detector of the Pierre Auger Observatory". In: *Journal of Cosmology and Astroparticle Physics* 04 (2017), p. 009. DOI: https://doi.org/10.1088/1475-7516/2020/09/E02.

[124] R. U. Abbasi et al. "Constraints on the diffuse photon flux with energies above 10^{18} eV using the surface detector of the Telescope Array experiment". In: *Phys. Rev. D* 110 (2019), p. 8. DOI: https://doi.org/10.1016/j.astropartphys.2019.03.003.

[125] P. Savina. "Search for gamma-rays in the EeV sky at the Pierre Auger Observatory using universality". In: *PhD Thesis at IJCLab, Orsay, INFN, Italy, Université Paris-Saclay* (2021). URL: https://inspirehep.net/literature/1905939.

[126] A. Aab et al. (Pierre Auger Collaboration). "Inferences on Mass Composition and Tests of Hadronic Interactions from 0.3 to 100 EeV using the water-Cherenkov Detectors of the Pierre Auger Observatory". In: *Phys. Rev. D* 96 (2017), p. 122003. DOI: https://doi.org/10.1103/PhysRevD.96.122003.

[127] S. Lafebre et al. "Universality of electron-positron distributions in extensive air showers". In: *Astroparticle Physics* 31 (2009), p. 243. DOI: https://doi.org/10.48550/arXiv.0902.0548.

[128] B. Rossi and K. Greisen. "Cosmic-Ray Theory". In: *Rev. Mod. Phys.* 13 (1941), p. 240. DOI: https://doi.org/10.1103/RevModPhys.13.240.

[129] M. Giller et al. "Energy spectra of electrons in the extensive air showers of ultra-high energy". In: *Journal of Physics G: Nuclear and Particle Physics* 30 (2004), p. 97. DOI: https://doi.org/10.1088/0954-3899/30/2/009.

[130] F. Nerling et al. "Universality of electron distributions in high-energy air showers—Description of Cherenkov light production". In: *Astroparticle Physics* 24.6 (2006), p. 421. DOI: https://doi.org/10.1016/j.astropartphys.2005.09.002.

[131] P. Lipari. "The Concepts of "Age" and "Universality" in Cosmic Ray Showers". In: *Phys. Rev. D* 79 (2009), p. 063001. DOI: https://doi.org/10.1103/PhysRevD.79.063001.

[132] M. Ave et al. "A generalized description of the time dependent signals in extensive air shower detectors and its applications". In: *Astroparticle Physics* 88 (2017), p. 46. DOI: https://doi.org/10.1016/j.astropartphys.2017.01.003.

[133] S. Andringa et al. "The muonic longitudinal shower profiles at production". In: *Astroparticle Physics* 35 (2012), p. 821. DOI: https://doi.org/10.1016/j.astropartphys.2012.03.010.

[134] L. Cazon et al. "A model for the transport of muons in extensive air showers". In: *Astroparticle Physics* 36 (2012), p. 211. DOI: https://doi.org/10.1016/j.astropartphys.2012.05.017.

[135] M. Ave et al. "A generalized description of the signal size in extensive air shower detectors and its applications". In: *Astroparticle Physics* 87 (2017), p. 23. DOI: https://doi.org/10.1016/j.astropartphys.2016.11.008.

[136] F. Schmidt et al. "A model-independent method of determining energy scale and muon number in cosmic ray surface detectors". In: *Astroparticle Physics* 29.6 (2008), p. 355. DOI: https://doi.org/10.1016/j.astropartphys.2008.03.004.

[137] A. Aab et al. (The Pierre Auger Collaboration). "Combined fit of spectrum and composition data as measured by the Pierre Auger Observatory". In: *Journal of Cosmology and Astroparticle Physics* 141 (2017), p. 038. DOI: https://doi.org/10.1088/1475-7516/2017/04/038.

[138] M. Ave. "On the feasibility of photon searches using X_{max}^{SD}". In: *Auger Internal Note* GAP 2013-086 (2013).

[139] F. James et M. Roos. "Minuit - a system for function minimization and analysis of the parameter errors and correlations". In: *Computer Physics Communications* 10 (1975), p. 343. DOI: https://doi.org/10.1016/0010-4655(75)90039-9.

[140] Rene Brun and Fons Rademakers. "ROOT - An Object Oriented Data Analysis Framework". In: *Nuclear Instruments and Methods in Physics Research Section A* 389 (1997), p. 81. DOI: https://doi.org/10.1016/S0168-9002(97)00048-X.

[141] C. Li. "Fisher Linear Discriminant Analysis". In: (2014). URL: https://api.semanticscholar.org/CorpusID:8370473.

[142] P. Sanchez-Lucas. "The $< \Delta >$ method: an estimator for the mass composition of ultra-high-energy cosmic rays ". In: *Auger Inernal Note* GAP 2017-005 (2017).